Soil – Anchor Interaction of a Floating Offshore Wind Turbine under Cyclic Load

Master Thesis

Georgios Christopoulos

TU Delft

Witteveen + Bos

TNO

Delft University of Technology

Faculty of Civil Engineering and Geosciences

MSc Geo-Engineering

Master Thesis Report

Soil – Anchor Interaction of a Floating Offshore Wind Turbine under Cyclic Load

By

Georgios Christopoulos

Student number: 5611903

To obtain the degree of Master of Science

At the Delft University of Technology

Thesis Committee:	Dr. Luca Flessati	TU Delft - Chair
	Dr. Ir. Evangelos Kementzetzidis	TU Delft
	Dr. George Lavidas	TU Delft
	Ir. Apostolos Bougioukos	Witteveen + Bos
	Ir. Feike Savenije	TNO

Cover: Semi-Submersible Illustration by Josh Bauer, NREL

Abstract

The rapid growth of Floating Offshore Wind (FOW) has spurred intensive research across various aspects of the floating system. A standard practice in mooring system design within the industry is that anchors remain fixed on the seabed. In contrast, plate-type anchors exhibit mobility under loading, a crucial factor considering the thousands of loading cycles experienced by FOW turbines during operation. Understanding the strain accumulation mechanism during cyclic loading has substantial implications for design.

This thesis delves into the behavior of Drag Embedded Anchors (DEAs) subjected to static monotonic and cyclic loading, utilizing 3-dimensional Finite Element simulations. The installation trajectory of DEAs is initially defined through established analytical methodologies. Subsequently, the movement of the anchor and soil response under monotonic and cyclic loads is elucidated.

Analytical expressions for monotonic force-displacement curves are examined, identifying optimal models and offering relevant parameter values for different anchor trajectory points. Under cyclic loading, the influence of average load and cyclic load amplitude is studied, along with exploring the feasibility of applying an existing 1-dimensional model for predicting anchor response.

Acknowledgements

As my Master of Science studies are near completion, I am grateful to all those who have supported me throughout this journey.

First of all, I would like to thank my Thesis committee members, Luca Flessati, Evangelos Kementzetzidis and George Lavidas from TU Delft, Apostolos Bougioukos from Witteveen+Bos and Feike Savenije from TNO.

Specifically, I would like to express my deepest appreciation to my thesis supervisor Luca Flessati for his guidance and support. I always felt I had a new insight after our meetings. Moreover, I would like to express my gratitude to Evangelos Kementzetzidis for his valuable guidance and feedback. I'm extremely grateful to Apostolos Bougioukos for his continuous guidance, support and eagerness to help when setbacks occurred. I would like to extend my gratitude to Feike Savenije whose knowledge and experience contributed to the realization of this Thesis.

Finally, I am thankful to my family and friends for their constant encouragement and understanding. I could not have undertaken this journey without their support.

Giorgos Christopoulos,

Delft, September 2023

Table of Contents

Chapter 1

Introduction

1.1 Background Information

In the last few decades, there has been systematic and thorough research in the field of offshore structure foundations, mainly due to the installation of offshore platforms for the oil and gas industry. More recently, there has been a global shift towards renewable energy with a plethora of offshore wind farms deployed internationally. Det Norske Veritas (DNV) predicts that, in 2050, fossil fuels will be responsible for just 12% of the total electricity production compared to the present 59% (**Figure 1.1**). Wind is predicted to account for approximately 30% of the total production showing an almost 10-fold growth (DNV AS 2021). Since the wind offshore is steadier and stronger than on land, the development of offshore wind is expected in order to take advantage of the steadier and greater supply of energy. The global offshore wind capacity in operation by the end of 2022 was 57.6 GW with an additional 12.4 GW under construction (Herzig 2022). The operational capacity is estimated to reach approximately 180 GW through 2027 based on developer-announced Commercial Operation Dates (Musial et al. 2022).

While the majority of operational wind farms is mainly installed in depths between 20m-60m (Europe 2019), an estimated 80% of Europe's offshore wind resource is located in depths greater than 60m (James and Ros 2015). The emergence of Floating Offshore Wind (FOW) offers the possibility of harnessing the high wind potential found in ocean areas characterized by water depths surpassing 60 meters, where traditional fixed-bottom foundations are not feasible. In the FOW concept, the wind turbines are placed on floating structures that are anchored to the seabed using anchors, chains, steel cables, or hybrid mooring systems. The FOW energy market in Europe, Asia and North America is currently at the pilot scale (10MW to 100MW). Initiating operation of three floating offshore wind projects added 57.1 MW to the operational capacity in 2021, the most prominent of which was the 50 MW Kincardine Offshore Wind Farm in Scotland (Musial et al. 2022).

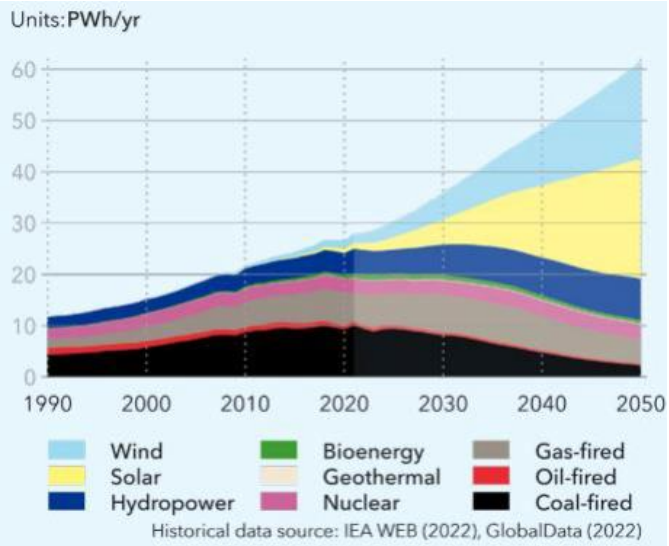

Figure 1.1: World grid-connected electricity generation by power station type

The main challenge for FOW technologies at the moment is cost reduction which is often associated with the Levelized Cost Of Energy (LCOE). The current cost is estimated at $200/MWh based on a small set of data, mainly demonstration projects. It is projected to be reduced to $60-$120/MWh by 2030 as early stage technology advances usually translate to considerable cost reductions. This will make FOW more competitive as the projected LCOE for fixed offshore wind is $60/MWh on average by 2030 (Musial et al. 2022). In this context, research on every aspect of a floating offshore wind concept should be funded, including but not limited to anchoring systems.

1.2 Problem Statement and Thesis Objective

The design of mooring systems for a Floating Offshore Wind Turbine (FOWT) is particularly challenging as it includes the interaction with the loads applied on the wind turbine by wind and waves, hydrodynamic effects on the mooring line etc. One aspect of the mooring system that is not implemented in the design is the interaction of the mooring line with the anchor. It is common for the industry to model the anchor as a fixed point located at the seabed at the bottom end of the mooring line. In reality, this is not the case as certain type of anchors may move significantly upon loading (e.g. plate anchors). Since the anchoring system of a FOWT experiences thousands of loading cycles while in operation, understanding the mechanism that governs the strain accumulation under cyclic loading could have significant design impact.

The scope of the Thesis is to investigate the behaviour of a selected anchor type under static monotonic and cyclic loading through 3 dimensional finite element analyses and find appropriate analytical expressions that accurately describe the soil-anchor interaction. The

anchor type to be studied, should be selected for a specific floating concept. In more detail, the focus is on:

a) The anchor response when subjected to static monotonic load.
b) The anchor response when subjected to static cyclic load.

1.3 Thesis Structure

Following this introductory chapter, Chapter 2 presents an overview of a floating system including different types of floaters, mooring configurations and the main types of anchors available in the industry.

Chapter 3 outlines the process of choosing various components of the floating system including the floater, mooring system, and anchor type for the case study. The forces exerted by wind and waves on the floater are calculated the appropriate anchor size based on these calculations is determined.

Chapter 4 describes the numerical model that is used for the finite element analyses in terms of geometry, mesh, constitutive law, boundary conditions and load stages. Additionally, the chapter elaborates on the analytical methodologies employed to predict the trajectory of anchor installation.

Chapter 5 presents the anchor's response mechanism under static monotonic loading. Analytical expressions are utilized to describe the force displacement curve. A parametric study on the effect of the initial anchor position is also included.

Chapter 6 presents the anchor's response mechanism under static cyclic loading for various load combinations and initial anchor positions. The parameters of an 1D model are calibrated to match the anchor's response and the predictions are compared to the Finite Element results.

Finally, Chapter 7 summarizes the main conclusions from the previous chapters and offers suggestions for future research.

Chapter 2

Literature Review

This Chapter is designed to make the reader familiar with the different parts that constitute a floating system. Initially, the different types of floating platforms and mooring systems are introduced as described by Du 2019, Ma et al. 2019, Uzunoglu et al. 2021, VRYHOF 2018, Yang et al. 2022. Secondly, an overview of the types of anchors available in the industry is presented as described by Cerfontaine et al. 2023, Da Silva 2021, VRYHOF 2018).

2.1 Floating Platforms

Fixed platforms were initially used to allow for offshore oil and gas production. However, their range of operation was limited to depths of 365m (1200 ft) and so the concept of the compliant tower was introduced which increased the range of operation to depths of 550m (1800 ft). The need to access resources located at areas with deeper water lead to the introduction of floating systems. A plethora of floating structures are available, the most common being Tension Leg Platform (TLP), Semi-submersible and Spar (**Figure 2.1**).

Figure 2.1: Floating wind turbine structures. From Left to Right: Spar, Semi-submersible, and TLP (Barter et al. 2020).

2.1.1 Tension-Leg Platform (TLP)

The TLP is characterized by the fact that it has higher buoyancy than weight which results in an upwards resultant force acting on the platform. To connect the platform to the foundation, vertical tubular steel tendons are used. These tendons are connected to the platform's hull at each corner and extend downward to the seafloor where they are anchored, typically using piles. Vertical motion of the platform is minimized due to the high axial stiffness of the tendons and to pre-tension. The tendons also provide the necessary tension to restrain the platform's lateral movement caused by wind, waves, and currents. They are suitable for water depths ranging from 300m to 1500m (1000-5000 ft).

The TLP is the most stable floating concept compared to the other two types. It offers the advantage of a smaller structure size, resulting in reduced material costs, similar to the semi-submersible. Additionally, TLPs can be deployed in various water depths starting from 40 meters. Moreover, the wind turbine can be installed on the TLP while it is still in the dockyard and subsequently transported to the designated site.

However, the Technology Readiness Level (TRL) of TLPs for floating wind applications is currently lower than that of the other two concepts. This is because TLPs, due to their high structural stiffness, are more susceptible to high-frequency dynamic loads, potentially causing resonant pitch and heave motions that can lead to fatigue damage in the tendons. Furthermore, TLPs have the most expensive anchoring system among the three concepts in terms of fabrication and installation.

2.1.2 Semi-submersible (Semi)

Semi-submersibles are floating structures partially submerged in water. The hull consists of multiple columns or trusses that provide stability and pontoons that provide buoyancy. The center of gravity is above the center of buoyancy, thus stability is achieved by the restoring moment. The platforms vertical position can be controlled by pumping water in or out of the hull.

Despite having a more complex structure and lower inherent stability in comparison to Spars and TLPs, semi-submersibles continue to dominate the industry due to the following reasons:

- Semi-submersibles can be utilized in a broad spectrum of water depths, usually starting from 40 meters.
- The cost associated with the anchoring system for semi-submersibles is lower than that of TLPs.

- The transportation and installation procedures for semi-submersibles are more straightforward compared to the other two concepts.
- By installing the turbine on the semi-submersible at the dockside and towing it to the site, costly offshore installations can be avoided.

2.1.3 Spar

A Spar consists of a large-diameter, single vertical buoyant cylinder with a deep draft. The lower portion of the platform is filled with ballast material, such as water or concrete, which lowers the center of gravity and provides stability. The upper portion of the platform contains air or other buoyant materials to generate the necessary upward force. Additionally, helical strakes are placed around the Spar to mitigate the effects of vortex-induced motions.

The Spar concept offers several advantages, including:

- Due to its deep draft design, the Spar concept provides greater stability compared to semi-submersibles.
- The structure configuration of Spars is generally simpler when compared to both semi-submersibles and TLPs.
- The cost associated with the anchoring system for Spars is lower than that of TLPs.

Nevertheless, the Spar concept does have certain disadvantages:

- The requirement for water depths exceeding 100 meters restricts the applicability of Spars due to their tall hull structure.
- Transportation in shallow water zones can be challenging.
- Turbine installation for Spars typically takes place offshore, similar to bottom-fixed foundations.

2.2 Mooring Systems

The mooring systems can be classified to a variety of types according to their operation lifetime, layout characteristics and mooring line configuration.

2.2.1 Temporary and permanent moorings

Depending on the duration of operation, moorings can be categorized as temporary or permanent. For a temporary mooring the station-keeping duration is between a few days to several months. Typical applications include pipe laying vessels, drill ships and crane vessels. A permanent mooring maintains station-keeping for years or even decades. This type of mooring

is suitable for a plethora of floating structures that are to operate in a fixed location for an extended period of time.

2.2.2 Spread and Single Point Moorings

Based on the requirements for restricting the heading of the floater, moorings can be distinguished as spread or Single Point Moorings (SPM) (See **Figure 2.2**). In a spread mooring setup, multiple mooring lines are distributed around the floating structure, effectively confining its offset and heading to facilitate its unimpeded operations. The floater heading is selected according to location specific environmental conditions. Compared to other alternatives, the spread mooring system offers a cost-effective and straightforward solution.

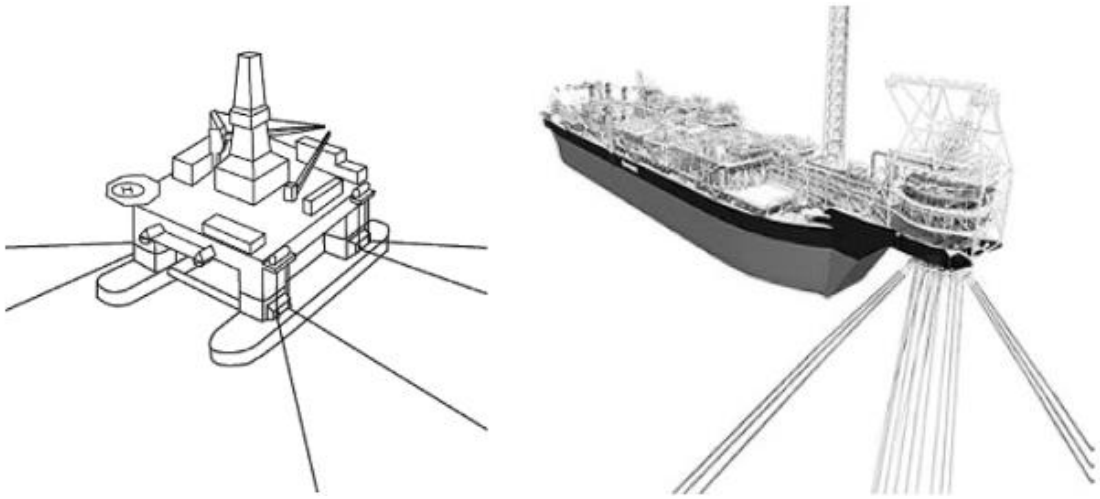

Figure 2.2: Typical spread (left) and single point (right) mooring systems (Ma et al. 2019).

The equal spread design, characterized by symmetrically distributed mooring lines with a consistent spread angle, is primarily employed for its simplified design process and potentially easier installation. Mooring lines may also be grouped into three or four clusters, enhancing mooring performance and creating a larger angular space for subsea facilities. These are often referred to as clustered-spread mooring systems.

The single-point mooring is the preferred solution for ship-shaped floating structures under severe sea conditions when the direction of wind, waves and currents is continuously shifting. The floater is allowed to rotate around the floater-mooring lines attachment point. It is most commonly used for floating production storage and offloading (FPSO) and has not been applied to an actual FWT project.

2.2.3 Catenary and Taut moorings

Depending on the mooring line configuration, the mooring systems of FWTs mainly include three types: catenary moorings, taut moorings and tether moorings. The catenary mooring is a mooring line, usually a steel chain, which at one end is suspended on the floater at the fairlead and on the other end it is attached to the foundation. Due to self-weight, the line creates a catenary shape with part of the mooring line resting on the seabed (**Figure 2.3a**). This leads to only horizontal loads transferred to the anchor point. When the floater is offset from its equilibrium position, part of the mooring line is lifted from the sea floor and due to the line's self-weight a restoring force is generated thus ensuring stability. Water depths shallower than 1000m is where it is most commonly applied.

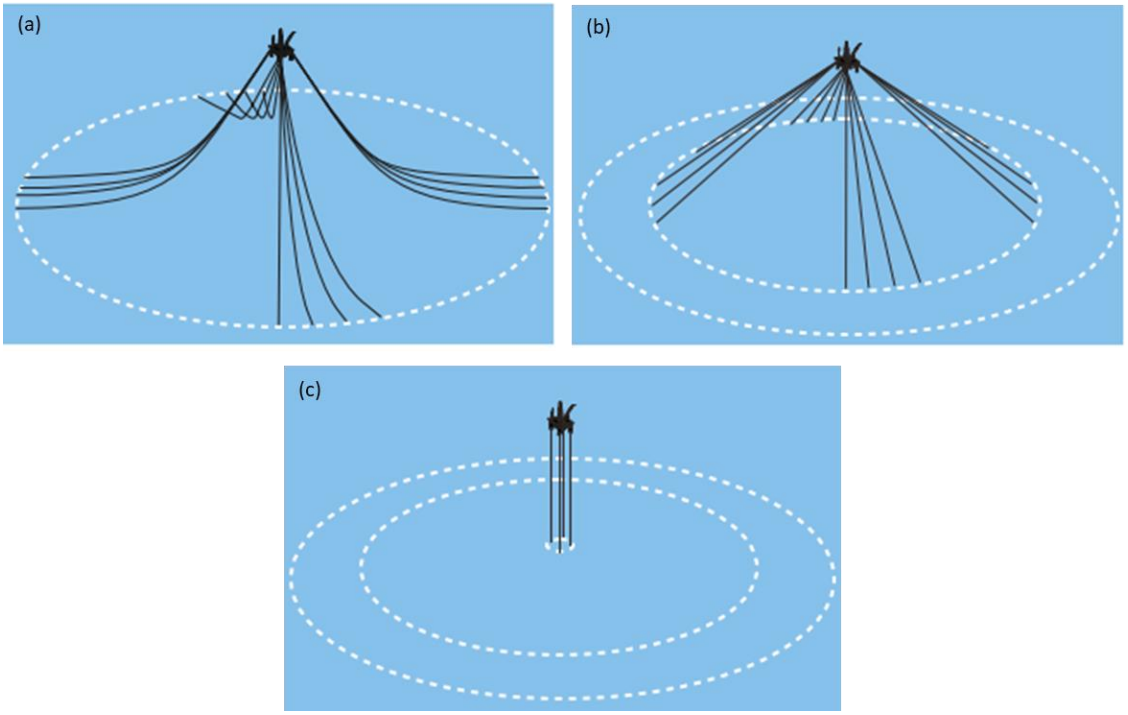

Figure 2.3: (a) Catenary, (b) Taut and (c) Tension mooring systems (VRYHOF 2018).

As the water depth increases, the mooring lines used in the system will need to be longer and heavier. This is because longer lines are required to reach the seabed and provide sufficient stability for the floating structure. However, this significantly raises the cost of the mooring system, as longer and heavier lines are more expensive to manufacture and install. Moreover, the added weight of the mooring lines reduces the overall deck payload capacity of the floating structure. Simultaneously, the mooring radius will also increase, affecting the laying of submarine pipelines, ship navigation and environmental footprint.

The catenary mooring has been the most frequent choice for floating oil and gas platform, as well as FWTs, mainly due to the following reasons:

- It is simple and stable.
- It is economical in the water depth shallower than 500 m.
- The mooring chain has relatively easier fabrication and simpler installation as compared to other types of mooring.

The taut mooring system has mooring lines that are pretensioned from the anchor point to the fairlead on the floater such that there is no line lying on the seabed in its equilibrium position (**Figure 2.3b**). The angle between the line and the seabed is typically between 30 and 45 degrees which means that both horizontal and vertical loads are acting on the anchor point. The footprint and the use of line material is smaller compared to the catenary mooring system. The taut mooring system usually uses wire ropes, high-strength nylon ropes, polyester cables or other synthetic materials. The compliance to floater offset and dynamic response comes mainly from axial tensile deformation of the line itself. The use of the taut system in shallow waters is limited as the mooring line stiffness may be very large and thus severely increase the line tension. Therefore, it is more suitable for deep and ultra-deep water applications.

As described in **Section 2.1.1**, Tension Leg Platforms (TLPs) utilize vertical mooring systems called tendons or tethers. These tendons are composed of steel tubes with high axial stiffness. Due to their vertical orientation relative to the seabed, the mooring radius is rather small. However, the fabrication process for tendons is complex. Furthermore, installing the tendons necessitates specialized vessels capable of maintaining the stability of the floater and connect the tendons. Consequently, the use of tether moorings results in significant costs associated with both fabrication and installation. A typical tension mooring system is depicted in **Figure 2.3c**.

2.3 Types of Anchors

Several anchor types have been developed in the industry with different shapes and installation methods.

2.3.1 Suction caisson anchors

They consist of a large-diameter stiffened cylindrical shell which is open at the bottom and closed on the top. When they are installed, they are lowered to the seabed and reach an initial embedment due to self-weight. Consequently, water is pumped out of an opening at the top

which creates a pressure difference inside and outside the caisson. This results in a downwards force that forces the caisson to embed until the cylinder is drained and the bottom is closed.

A schematic representation of the installation of such anchors is depicted in **Figure 2.4**. The pumps are installed and removed either by divers or remote operated vehicles (ROV).

Compared to other anchor types, their after installation position is known and they don't require to be proof loaded. Moreover, they are able to bear both horizontal and vertical loads which makes them suitable for both catenary and taut mooring. Their advantage over piles is that their installation doesn't necessitate heavy hammers or auxiliary platforms. However, their installation may be difficult in heterogeneous soils with hard layers. Furthermore, the high pressure required for installation in some sandy soils may result in failure of the soil plug within the caisson.

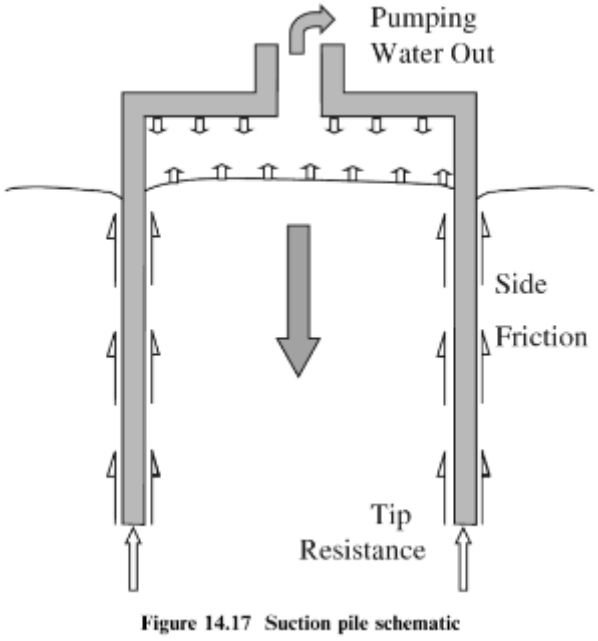

Figure 14.17 Suction pile schematic

Figure 2.4: Installation of a suction caisson (de Koning 1984).

2.3.2 Anchor Pile

Anchor piles are hollow steel tubes with a mooring line attached at some point below the mudline (**Figure 2.5**). They generate capacity by the friction between the soil and the pile and are able to bear both vertical and horizontal loads. Despite being able to be installed in a variety of soil conditions, they are associated with high installation costs due to the need of additional equipment. These cost increase with water depth and thus are not preferred for depths greater than 1500m. There also environmental concerns regarding their installation procedure.

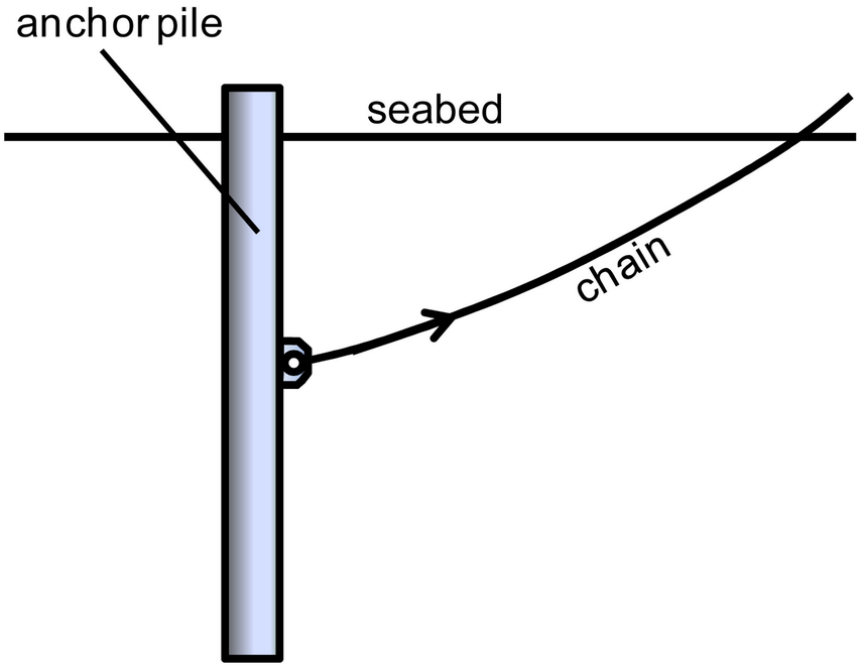

Figure 2.5: Chain attached to an anchor pile at the padeye (Loukidis et al. 2014).

2.3.3 Screw anchors

They arose as an alternative to conventional anchor piles which reduces the noise during installation. They possess significant tensile strength and are more efficient than piles when subjected to tensile loads. The main difficulty with screw anchors lies in the substantial torque and force needed for their installation. However, their decommission process could potentially be less expensive than the alternatives by reversing the installation procedure.

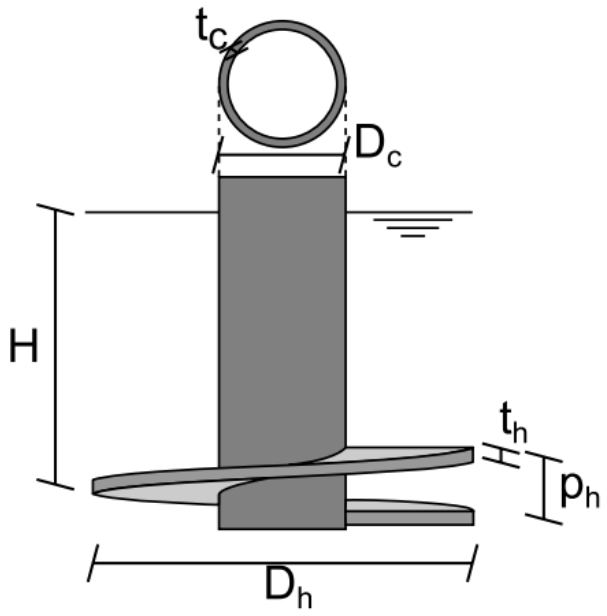

Figure 2.6: Schematic of a single helix screw anchor (Cerfontaine et al. 2020).

2.3.4 Drag-Embedded anchor (DEA)

Drag-embedded anchors consist of a fluke rigidly connected to a shank, as depicted in **Figure 2.7**. At the free end of the shank, there is an anchor shackle where the mooring line is attached. Their geometry allows them to penetrate into the soil when dragged. The majority of the capacity comes from the bearing resistance of the plate with some additional capacity coming from friction between the soil and the shank. The low installation cost makes them the most popular anchor choice presently. However, they are not able to withstand large vertical loads and thus are typically used for catenary moorings but not for taut and semi taut lines in very deep waters. Another limitation is the high degree of uncertainty regarding the trajectory and final position of the anchor during installation. Moreover, large drag distances may be necessary for the ultimate capacity to be achieved.

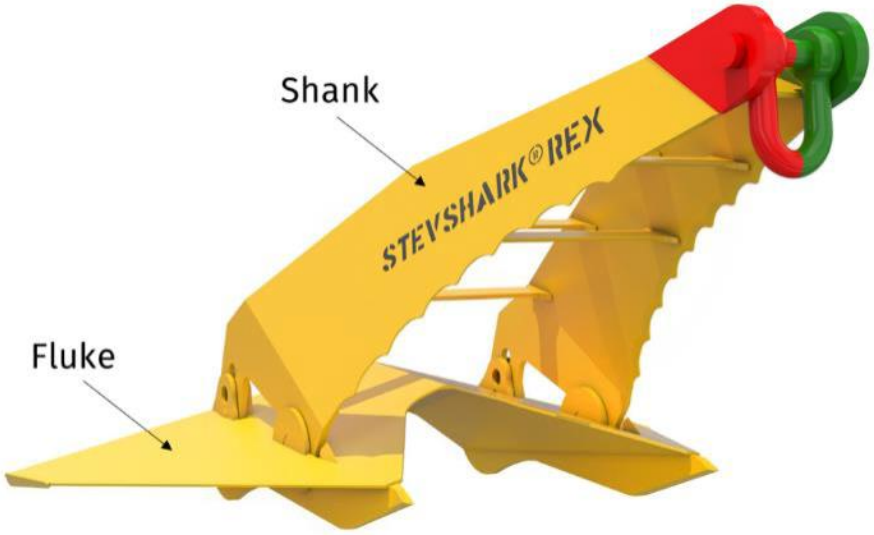

Figure 2.7: Components of a Drag Embedded Anchor (VRYHOF 2018).

2.3.5 Vertically loaded anchor (VLA)

VLAs are installed in a similar way as DEAs. The main difference is that after the anchor has reached the desired depth, the shank can be reconfigured such that the load acts perpendicular to the plate, thus maximizing its capacity (**Figure 2.8**). Consequently, VLAs can bear both horizontal and vertical loads making them suitable for both catenary and taut moorings. Additionally, they are among the most light-weight anchors available in the industry and have low installation costs. Similar to drag anchors, their limitations are mainly the uncertainty of the installation trajectory and final position.

Figure 2.8: Vertically Loaded Anchor Stevmanta (VRYHOF 2018).

2.3.6 Dynamically installed anchors

They were developed to overcome the high costs of anchor installation in deep waters. They are released from a predefined height above the sea bed and are able to embed into the soil due to the accumulation of kinetic energy before impact. Their initial shape was similar to a torpedo, so they are also refers to as torpedo anchors, but alternative designs have also been proposed, as presented in **Figure 2.9**. In clays, the usual penetration depth is between two and three times the anchor length and their holding capacity is between three and six times the anchor weight. Although they have lower capacity compared to other anchors, their low cost and their ability to bear both vertical and horizontal loads makes them a competitive choice.

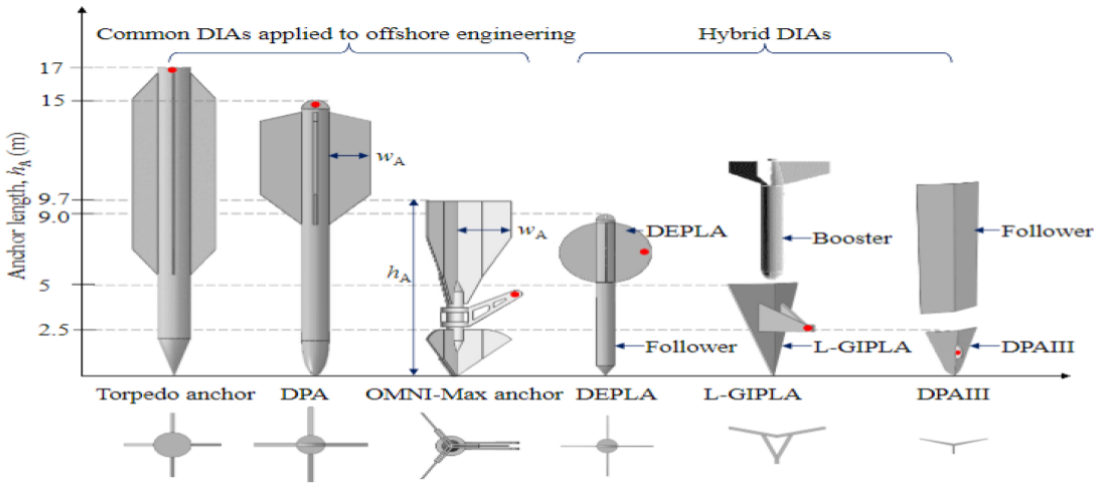

Figure 2.9: Types of dynamically installed anchors (Han and Liu 2020).

2.3.7 Plate anchors

A type of plate anchor is the suction embedded plate anchor (SEPLA) which comprises of a rectangular thin fluke, a shank connecting the fluke the padeye and an optional keying flap. They are embedded with the assistance of a suction caisson, which is called the follower. The plate is initially placed at the tip of the caisson perpendicular to its cross-section, as presented in **Figure 2.10**. The pressure differential inside and outside the caisson forces it to embed to a predefined depth within the soil. Consequently, the follower is retrieved and can be reused. Then, the mooring line attached to the padeye is pulled from an anchor handling vessel (AHV) which forces the plate to rotate and become perpendicular to the load direction. This rotation process while the anchor is being pulled is called keying and results in an upwards motion and hence, a loss of embedment depth.

SEPLAs can reach high vertical and horizontal capacities and are therefore suitable for both catenary and taut moorings. Moreover, there is little uncertainty over their final position. The keying flap, when present, aims to reduce the loss of embedment during the keying process. The main disadvantage associated with SEPLAs is the loss of embedment during keying and thus loss of capacity. Their high cost of installation, mainly due to the use of a large diameter suction caisson, is another disadvantage.

Figure 2.10: A plate anchor positioned at the tip of the follower (Chao and Eng 2016).

A more recent type of plate anchor is the dynamically embedded plate anchor (DEPLA) which takes advantage of the easy installation of dynamically installed anchors and the high holding capacity of plate anchors. It consists of a piece with four flukes and a follower of torpedo shape. After embedment is achieved with free-fall, the follower is retrieved and can be reused. The anchor is then subjected to keying by tensioning the mooring line attached to the flukes,

which reorientates the anchor so that it is almost perpendicular to the load direction (**Figure 2.11**). Their fabrication costs can be 70-80% less than SEPLAs. Similar to SEPLAs, their main disadvantage is the need for keying which results in loss of embedment and thus loss of capacity.

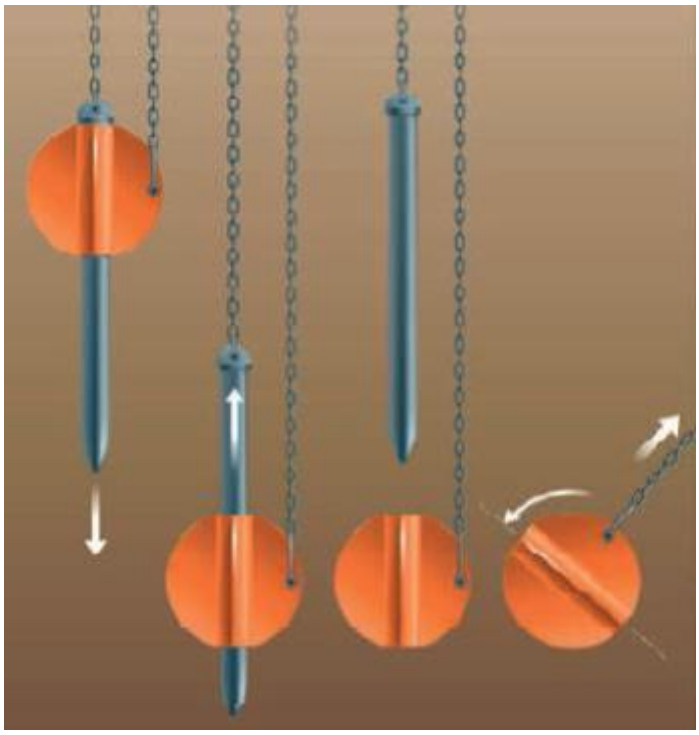

Figure 2.11: Installation and keying of a DEPLA (Da Silva 2021).

Chapter 3

Anchor Size Selection Based on Local Environmental Conditions

3.1 The Floating Platform

Initially, the location where the platform is to be analyzed is selected based on local environmental conditions. Different sites were considered, including the US west coast where deep water is prevalent and in the Mediterranean. Ultimately, a location 15km of the coast of Aberdeen in Scotland was selected. The area (depicted in blue in **Figure 3.1**) covers approximately 3400 km^2 and includes the Kincardine floating offshore wind farm which consists of 6 operational wind turbines with total capacity of 50MW on semisubmersible floaters connected to Drag Embedded Anchors (DEAs). The location is appropriate for floating offshore wind as it has a mean wind speed above 9 m/s and the water depth ranges from 50m-220m (James and Ros 2015).

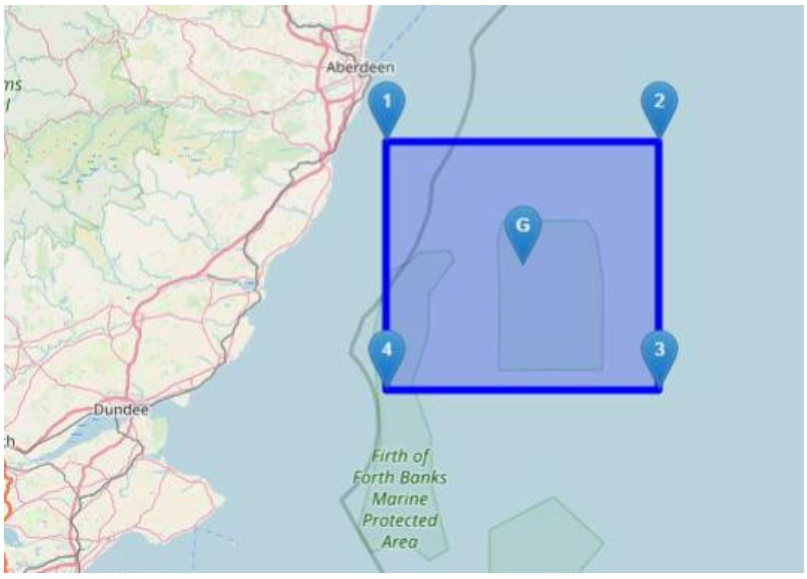

Figure 3.1: Location considered near Aberdeen, Scotland (Geo.jawaga.nl).

Since this research focuses on anchor behaviour, an existing floating platform is selected based on its future potential and available information. In 1985, typical turbines had a rated capacity

of 0.05 MW and a rotor diameter of 15m. Today's new wind power projects have reached a turbine capacity range of 8-12 MW offshore which tends to increase (IRENA 2022). As for the foundation type, semisubmersibles seem to be the preferred choice of the industry with over 14GW in total capacity projects globally announced in 2021 (**Figure 3.2**). Considering the above, plus the need for available information, the floater selected to be examined in this Thesis is the VolturnUS-S developed by the University of Maine (Allen et al. 2020).

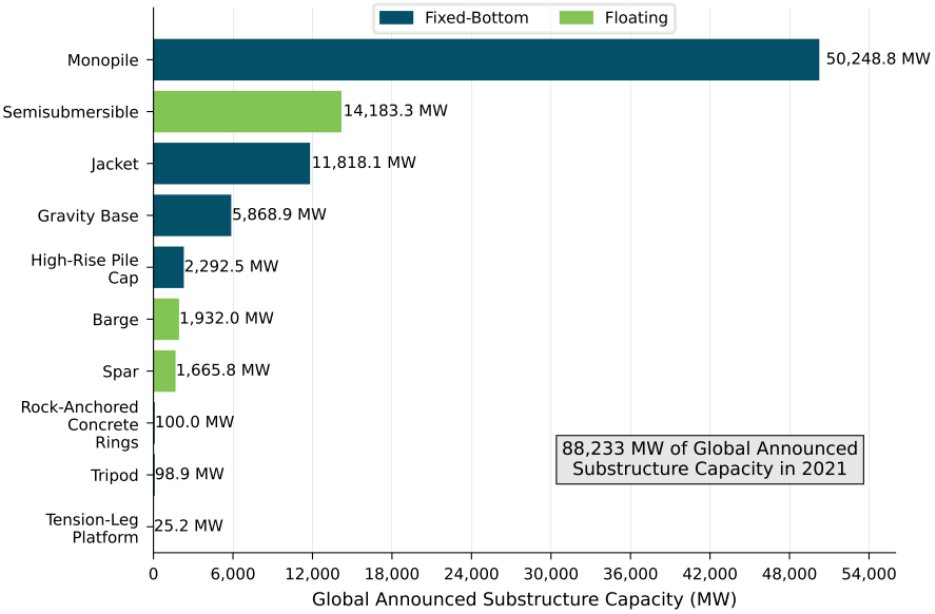

Figure 3.2: Announced offshore wind substructure technology for future projects (Musial et al. 2022).

Figure 3.3: The UMaine VolturnUS-S reference floating offshore wind turbine (Allen et al. 2020).

In 2013, the University of Maine (UMaine) and its collaborative partners successfully deployed VolturnUS, a prototype of a floating structure. This prototype was scaled down to 1:8 of the intended design, which was a 6 MW offshore wind turbine with a rotor diameter of 140 meters. The hull of the structure was constructed using concrete while the tower was crafted by composite materials. The moorings consisted of steel chains linked to drag anchors. The subsequent version, known as the UMaine VolturnUS-S reference floating offshore wind turbine semisubmersible, is an adaptation of the original UMaine VolturnUS floater. This advanced version is constructed from steel and engineered to support a 15 MW reference wind turbine, as depicted in **Figure 3.3**.

The floater comprises of three radial steel columns and one central that supports the 150m tall and 1263t heavy tower and the 990t RNA. The cut-in, rated and cut-off wind speeds at hub height for the turbine are 3, 11 and 25 m/s, similar to the respective values of 3.5, 14, 25 m/s of the Kincardine turbine. After installation, the semisubmersible has a 20m draft and a 15m freeboard. The water depth at the deployment site is assumed to be 200m and the floater is held into place by chain catenary mooring lines spanning approximately 850m from each radial column. The technical report released by UMaine and the US National Renewable Energy Laboratory (NREL) is a rich source of information ranging from a system overview to technical specifications of the floating platform, mooring system, turbine tower and turbine controller. Simulations such as static offset are also included ii the report.

NREL's description of the mooring system does not include any indication on the type or dimensions of the anchor to be used. This is understandable because determining the appropriate anchor requires complex calculations of loads on the floater and catenary system specific to the chosen location, which goes beyond the scope of their study. To address this gap, it was decided to undertake this step in this Thesis in order to later conduct finite element analyses for an anchor suitable for the UMaine floater. Drag Embedded Anchors (DEA) were chosen as they are the most commonly utilized anchor type in both soft and hard soils, aligning with the prevalent use of catenary mooring configurations (James and Ros 2015).

3.2 Environmental Loads

In order to calculate the loads that act upon the floater, data regarding the wind velocity and wave significant height and peak period are required. A reliable source of such data is the Copernicus Climate Change Service, a website that offers free and open access to climate data (Copernicus 2023). From their database, the following hourly data from the last 10 years (2013-2022) were extracted:

• wind speed at 10m height (m/s).

• Significant height of combined wind waves and swell (m).

• Peak wave period (s).

3.2.1 Forces from the wind

Figure 3.4 depicts the histogram of the wind speeds averaged over a time span of 1 hour measured at 10 meters height for the chosen location. The 10 year average wind speed is close to 8 m/s and the peak value is over 26 m/s. DNV claims that the annual maximum of the 10-minute mean wind speed $U_{10,max}$ can often be assumed to follow a Gumbel distribution as in Equation 3-1 (DNV-RP-C205). The parameters a and b are estimated with Equations 3-2 and 3-3 as per Kang et al. 2015. It must be noted that while DNV proposes Equation 3-1 for the annual maximum of the 10-minute mean wind speed, the available data from Copernicus are hourly averages.

$$F_{U_{10,\max},1year}(u) = \exp\left\{-\exp\left[-a(u-b)\right]\right\} \quad 3\text{-}1$$

Where:

u is the 10-minute mean wind speed (m/s)

$$a = \frac{\pi}{\sigma\sqrt{6}} \quad 3\text{-}2$$

$$b = \bar{u} - 0.45\sigma \quad 3\text{-}3$$

Where $\bar{u}$ and σ represent the mean and standard deviation of the annual extreme mean wind speeds of the measured data and are equal to 22.51 m/s and 1.49 m/s.

The 10-minute mean wind speed with return period T_R in units of years is defined as the $(1-1/T_R)$ quantile in the distribution of the annual maximum 10-minute mean wind speed, i.e. it is the 10-minute mean wind speed whose probability of exceedance in one year period is $1/T_R$. For instance, the 50-year wind speed is the 98^{th} quantile of the distribution. Using Equations 3-2 and 3-3, the values for a and b are 0.862 and 21.835 respectively. Although the methodology is originally intended for 10-minute average wind speeds, it is applied to 1-hour average wind speeds due to the limitation of available data. Hence, the calculated 50-year 1-hour mean wind speed at a height of 10 meters amounts to 26.36 m/s.

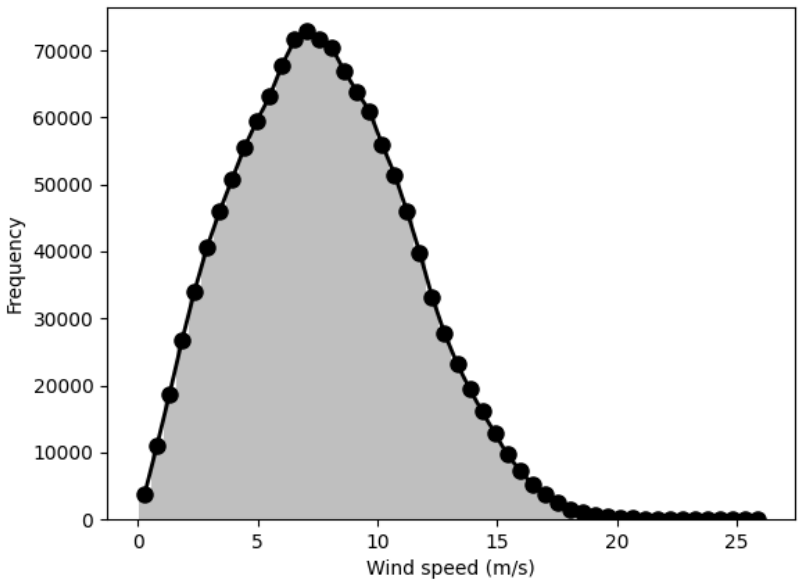

Figure 3.4: Histogram of 1-hour averaged wind speeds at 10m height from the last 10 years.

The total wind load can be distinguished into two parts. The load on the tower and the load on the blades. The load on the tower can be estimated by integrating the wind force distribution along the tower height. Hence, an appropriate wind profile is needed. For offshore locations the Frøya wind profile is recommended by DNV. It provides Equation 3-4, that can convert the one hour mean wind speed U_o at height H above sea level to mean wind speed U with averaging period T at height z above sea level. The hourly averages are converted to ten minute averages which is a typical averaging period for offshore wind.

$$U(T,z) = U_o \cdot \left\{1 + C \cdot \ln\frac{z}{H}\right\} \cdot \left\{1 - 0.41 \cdot I_u(z) \cdot \ln\frac{T}{T_o}\right\} \quad \text{3-4}$$

Where H=10m, T_o=1 hour and T=10 minutes, where

$$C = 5.73 \cdot 10^{-2}\sqrt{1 + 0.148U_o} \quad \text{3-5}$$

$$I_u = 0.06 \cdot (1 + 0.043U_o) \cdot \left(\frac{z}{H}\right)^{-0.22} \quad \text{3-6}$$

The basic wind pressure is defined by Equation 3-7.

$$q = 0.5 \cdot \rho_\alpha \cdot U^2(T,z) \quad \text{3-7}$$

With

ρ_α = 1.226 kg/m3 for dry air at 15 °C, the mass density of the air.

The wind force F_w on a structural member acting normal to the member axis may be calculated according to Equation 3-8.

$$F_w = C_D \cdot q \cdot S \cdot \sin\alpha \qquad 3\text{-}8$$

Where α is the angle between the direction of the wind and the axis of the exposed member taken equal to 90˚, C_D is a shape coefficient taken equal to 0.85 for the tower and S is the projected area of the member normal to the direction of the force. Since both q and S vary with height, the wind force distribution on the tower is initially calculated and the total wind load can be calculated by integration of the force distribution over the whole tower length.

The wind load on the blades calculation must distinguish between when the turbine is in operation and when it is idle. When generating electricity, the force is equal to the thrust force and, when idle, the drag force on the blades must be calculated. The drag force on a single blade is calculated based Equation 3-9. However, if one of the blades is vertical, the other two are at 60˚, so assuming a reduction on the force proportional to the reduction of the projected area we get a total factor for three blades: 1 + cos(60˚) + cos(60˚) = 2 times the single blade. The case for one blade horizontal is less conservative as cos(30˚) + cos(30˚) ≈ 1.7.

$$F_{blade} = C_D \cdot q \cdot A_{blade} \qquad 3\text{-}9$$

The drag coefficient C_D was taken equal to 1.5, in accordance with the IEA 15MW RWT that uses about 1.5 for 90 degrees angle of attack (AoA). The area of one blade A_{blade}, was calculated as approximately 480m^2. The NREL has made available the thrust force values with varying operational wind speeds as results from their analyses.

Figure 3.5 shows the wind force on the tower, blades and the summation. The force on the tower (blue line) keeps increasing with increasing wind speed as it is a function of the square of the wind speed. Looking at the force on the blades (green line), we can observe as soon as the turbine begins operation at 3 m/s, the thrust force increases and reaches its peak of 2500 kN at the rated wind speed. For higher wind speeds and up to the cut off speed, the force decreases as a result of the turbines control system to maintain the rated capacity. After the wind speed of 25 m/s, the turbine is no longer in operation and the drag force increases with increasing wind speed as it is also a function of the square of the wind speed. The graph ends at u = 36.4 m/s which is the 10-minute wind speed at hub height with a 50 year return period, converted from the 1-hour mean wind speed at 10m height with a 50 year return period. It is

evident from the graph that there are two local maximums, 2570 kN at rated wind speed and 1900 kN at 50 year wind speed.

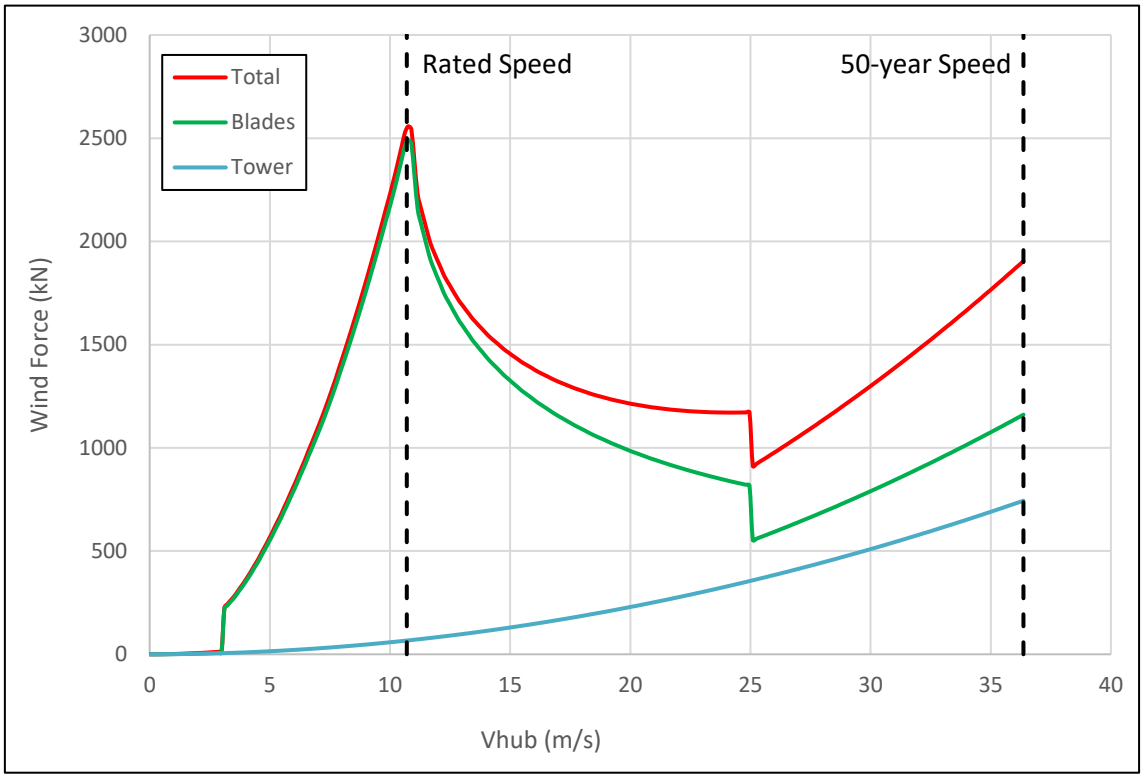

Figure 3.5: Wind force against the wind speed at hub height.

3.2.2 Forces from the waves

Figure 3.6 depicts the scatter plot of H_s - T_p for the chosen location, created by plotting individual data points, where each point represents a specific measurement of wave height (H_s) and peak wave period (T_p). It is evident from the plot that the most frequent waves have a height below four meters and come at peak periods of 2.5 to 12.5 seconds. According to DNV-RP-C205, a Weibull distribution can be used for the significant wave height. The probability and cumulative density functions of such a distribution are described by Equations 3-10 and 3-11. The scale (λ) and shape (κ) parameters were calibrated against the measured values using the maximum likelihood estimation method and are 1.6 and 1.74 respectively.

$$f(x) = \frac{\kappa}{\lambda}\left(\frac{x}{\lambda}\right)^{\kappa-1} e^{-(x/\lambda)^{\kappa}} \qquad 3\text{-}10$$

$$F(x) = 1 - e^{-(x/\lambda)^{\kappa}} \qquad 3\text{-}11$$

The cumulative density function derived from the measured data is compared to the Weibull prediction in **Figure 3.7** and shows a good match. The significant wave height with return period T_R in units of years can be defined as the (1-1/(n*T_R)) quantile of the distribution of significant wave heights, where n is the number of sea states per year. Since the values are 1-hour averages, there are 8760 sea states per year. Therefore, the significant wave height with return period 50 years can be calculated and is 6.98m.

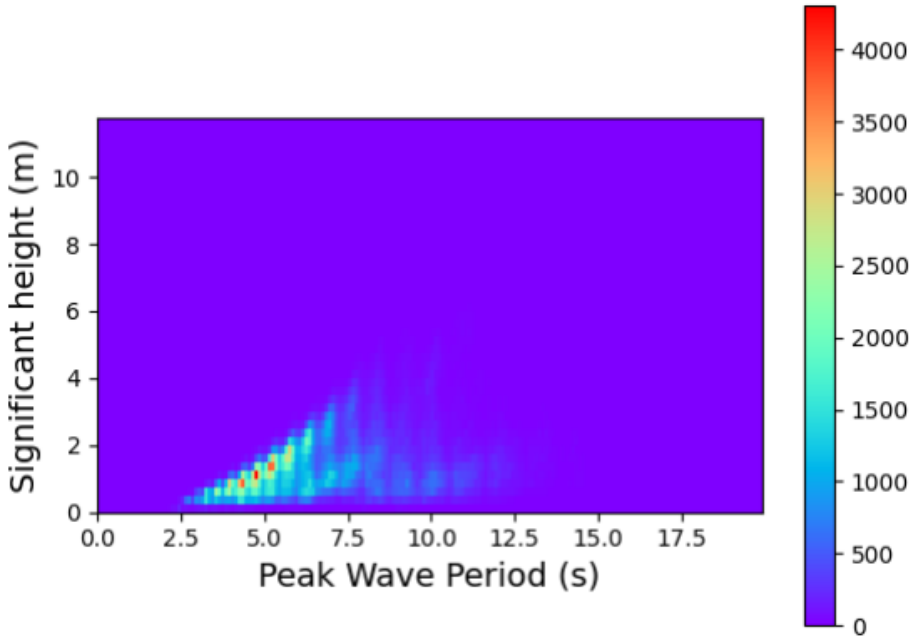

Figure 3.6: Wave significant height H_s and peak period T_p scater plot.

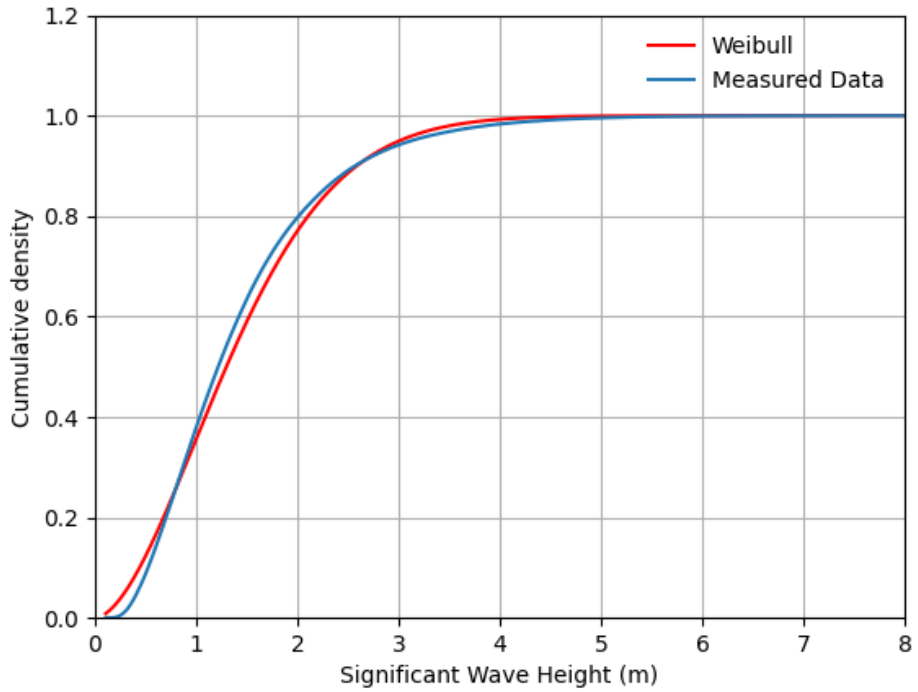

Figure 3.7: Cumulative Density Function from the measured data and the Weibull function.

NREL has conducted hydrodynamic analyses on the UMaine Semi using WAMIT (WAMIT 2011) and has made the results available. WAMIT is a computer program based on the linear and second-order potential theory for analyzing floating or submerged bodies, in the presence of ocean waves. The boundary integral equation method (BIEM), also known as the panel method, is used to solve the velocity potential and fluid pressure on the submerged surfaces of the bodies. Separate solutions are carried out simultaneously for the diffraction problem, giving the effects of incident waves on the body, and the radiation problems for each of the prescribed modes of motion of the bodies.

Relevant for this Thesis are the results from the first-order setup which include wave excitation at all headings in 10 degree increments and frequencies ranging from 0.008 Hz up to 0.8 Hz. The output is given in terms of normalized exciting forces for each degree of freedom (Surge, Sway, Heave, Roll, Pitch, Yaw) according to Equation 3-12:

$$\overline{X_i} = \frac{X_i}{\rho g A L^m} \qquad 3\text{-}12$$

Where ρ is the water density, g is the acceleration of gravity, A is the incident-wave amplitude and L is the length scale taken as 1 for their analyses. Replacing the incident wave amplitude A with 3.5m, and combining the surge and sway loads, the maximum horizontal load on the floater ranges from 16980 kN to 17700 kN (based on the wave heading) for the appropriate frequency range of this location.

3.2.3 From Floater to Seabed Level

The methodologies presented in the previous sections can estimate the loads that the wind and waves impose on the floater. Since the floater is connected to the foundation via catenary mooring lines, the chain weight and stiffness affect the load that is ultimately applied to the foundation. For determining this load, the MoorPy toolset developed by NREL is employed. MoorPy is a quasi-static mooring model written in Python, capable of analyzing floating systems with complex mooring line configurations. Each mooring line segment is solved using standard catenary equations. MoorPy automatically solves for equilibrium of the mooring system geometry and external loads the user defined. It also allows for visual representation of the results as it includes built-in plotting functions. The UMaine floater geometry was modeled with this tool by specifying the following parameters.

- The water depth.
- The (x,y,z) coordinates of the end points of all mooring lines.

• The unstretched length of each mooring line.

• The chain diameter, axial stiffness and dry mass density.

The floater was modelled as a free body connected to one end of each mooring line at the corresponding fairlead. The other end of the mooring lines was fixed at the foundation location. To verify the model accuracy, the results are compared with the values of the Static Surge-Sway Offsets given in the description of the UMaine floater. Two situations are compared, the initial at rest state and the state at 30m surge offset. The later situation was selected as it was easier to read the tension values from the diagram in the UMaine description. **Table 1** compares the model results with the UMaine description values. The values compared are quite accurate and the deviation can be attributed to the difficulty of reading the tension values from the 3D curve the UMaine floater description presents them. It is concluded that the model is very accurate and may be used to calculate the loads at the anchor level.

Table 1: Tension results comparison.

Force	Model	UMaine	Difference
Fairlead Tension (at rest) [kN]	2420	2437	-0.7%
Fairlead Tension (30m Offset) [kN]	5450	5500	-0.9%
Anchor Tension (30m Offset) [kN]	4400	4500	-2.2%

From the previous section, the wave load on the floater was derived to be in the range 16980 kN - 17700 kN. The wind load was found to have two local maximums, 2570 kN at rated wind speed and 1900 kN at 50 year wind speed (**Figure 3.5**). The first peak occurs with the turbine operating and corresponds to design load case (DLC) 1.6 (Iec 2019). This load case simulates power production without faults performed for wind speeds in the entire operational range with normal wind turbulence but under severe sea state (SSS) conditions (Hartvig 2019). As a conservative estimation, the 50-year return significant wave height independent of wind speed is used to approximate $H_{s,SSS}$ (Bureau of Shipping 2020). The partial load factor for this load case is 1.35 (Hartvig 2019) which makes the design load on the floater equal to 27360 kN. The second peak occurs with the turbine parked and at fault condition and corresponds to design load case (DLC) 6.2 (Iec 2019). This load case simulates a parked turbine with idling rotor and abnormally large yaw error at a wind speed with 50-year recurrence period under extreme sea state (ESS) (Hartvig 2019). For this specific load scenario, it's necessary to factor in gusts according to Iec 2019 by multiplying the 10-minute wind speed by 1.4. Since the load is dependent on the square of wind speed, the original load of 1900 kN then gets multiplied by

the square of 1.4, resulting in a wind load of 3730 kN. The partial load factor for this load case is 1.10 (Hartvig 2019) which makes the design load on the floater equal to 21430 kN. It is evident that when implementing the partial load factors, the load case during operation becomes the critical one for the design.

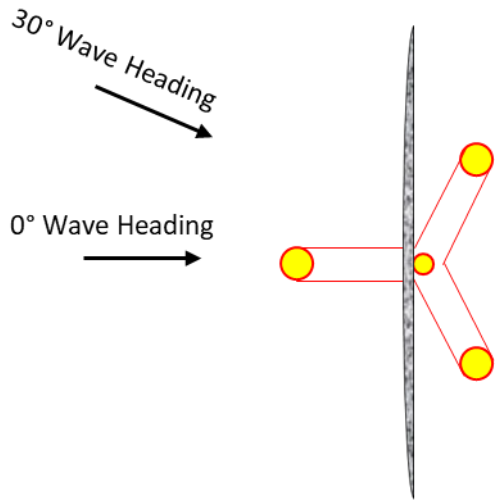

Figure 3.8: Wave heading angles relative to the UMaine Floater.

Table 2 presents detailed results for the required Ultimate Holding Capacity (UHC) of the anchors. The wave load corresponds to the output calculated by NREL for 7m wave height for all possible wave headings (0° – 180° due to floater symmetry). **Figure 3.8** illustrates examples that clarify the concept of wave headings at 0° and 30° with respect to the floater. The design load adds the two local maximums of wind load and keeps the most critical as described above. The anchor load is the maximum load computed on any of the 9 anchors by MoorPy by applying the design load in the appropriate wave heading. An example of the system solved by MoorPy is depicted in **Figure 3.9**. The required UHC is the anchor load multiplied by 1.8, a safety factor introduced by VRYHOF 2018 to account for the fact that the calculation was quasi-static and not dynamic. Thus, the maximum required UHC is 28753 kN. As this Thesis is to examine Drag Embedded Anchors, the market available anchor designs were considered. The aim is to choose an anchor whose capacity is higher than the required UHC of 28753 kN. Ultimately, the 65t drag anchor from the Vryhof Stevpris Mk5 series was selected as it can achieve a capacity of 34MN (VRYHOF 2018).

Table 2: UHC calculation for varying wave heading.

Floater			Anchor	
Wave Heading (°)	**Wave Load (kN)**	**Design Load (kN)**	**Anchor Load (kN)**	**Required UHC (kN)**
0	17023	26451	12392	22306
10	16998	26417	14483	26069
20	16980	26393	15258	27464
30	17080	26528	14536	26165
40	17322	26854	12584	22651
50	17586	27211	14987	26977
60	17701	27366	15962	28732
70	17586	27211	15053	27095
80	17322	26854	12594	22669
90	17080	26528	14544	26179
100	16980	26393	15276	27497
110	16998	26416	14462	26032
120	17023	26451	12394	22309
130	16998	26416	14465	26037
140	16980	26393	15257	27463
150	17080	26528	14535	26163
160	17322	26854	12584	22651
170	17586	27211	15000	27000
180	17701	27366	15974	28753

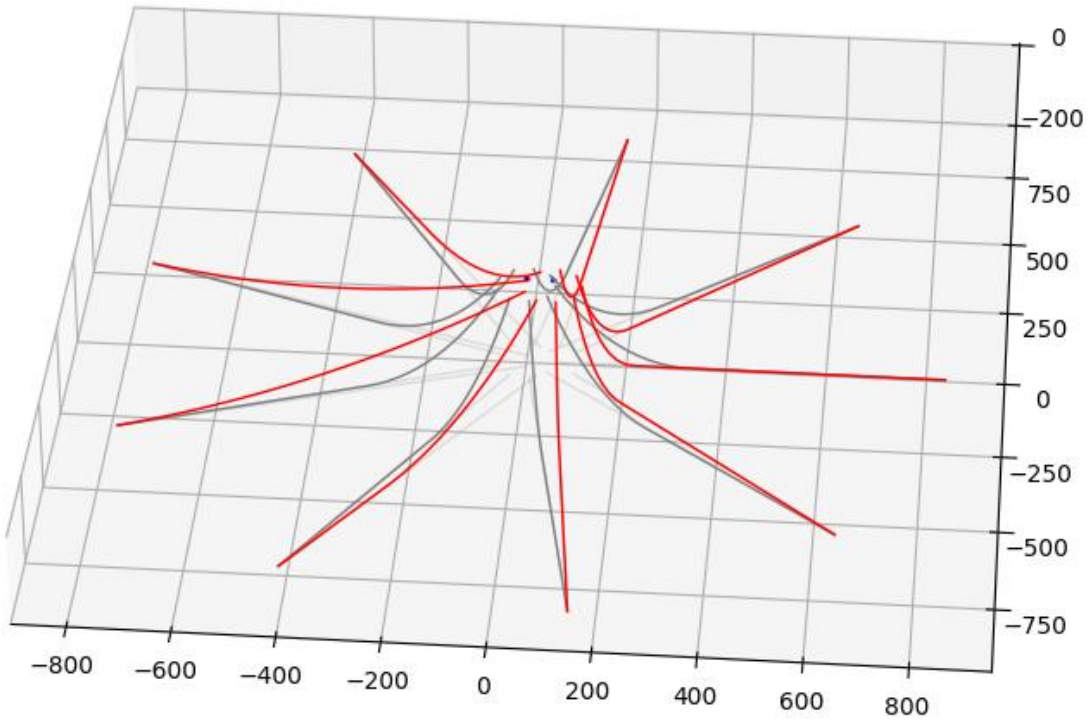

Figure 3.9: Simulation of the floater and 9 mooring lines in MoorPy. The grey lines show the initial at rest situation and the red lines the situation after applying a horizontal load.

Chapter 4

Methodology of Numerical Analyses

4.1 The numerical model

4.1.1 Model Geometry and Mesh

All the numerical analyses mentioned in this Thesis are three dimensional and small-displacement and were performed with the PLAXIS Finite Element software. Modeling the geometry of a Stevpris Mk5 (**Figure 4.1a**) presents a considerable challenge. To tackle this, the focus will be solely on the anchor fluke within the numerical simulations, employing a two-dimensional plate structural element. For the sake of simplicity, the simulation will assume complete rigidity of the plate. The width B of this equivalent plate was set equal to the actual width of the anchor and the out of plane length L was calculated in order to give the same fluke projected area A_{proj}. The assumptions that a rectangular plate with the same fluke area can represent a DEA is widely accepted in the published literature. A fictitious thickness was assigned to the plate considering that the plate should have the same dry weight as the original 65t anchor. A sketch of the equivalent plate is depicted in **Figure 4.1b**.

The shank length is 11.563m and is assumed to be at an angle of 32 degrees relative to the fluke for use in sandy soils. Thus, the padeye eccentricities normal e_n and parallel e_p to the anchor fluke can be calculated. The padeye offset ratio for this anchor is $\eta = e_p / e_n = 1.1$ which is consistent with the calculations of Maitra et al. 2022 for a fluke-shank angle equal to 32 degrees. The material assigned to the plate is steel and its properties are presented in **Table 3**. The geometry of the equivalent plate is summarized in **Table 4**.

Table 3: Steel properties.

Young's modulus	210	GPa
Dry density	7.85	Mg/m^3
Poisson's ratio	0.3	-

Table 4: 3D plate geometry.

Fluke Width, B	6.4	m
Fluke Projected Area, A_{proj}	39.8	m2
Fuke Length, L	6.2	m
Fluke Thickness, t	0.2	m
Fluke-Shank angle, θ_{fs}	32	°
Shank Length, Lshank	11.563	m
Padeye offset parallel, e_p	6.624	m
Padeye offset normal, e_n	6.127	m
Padeye offset ration, η	1.1	-

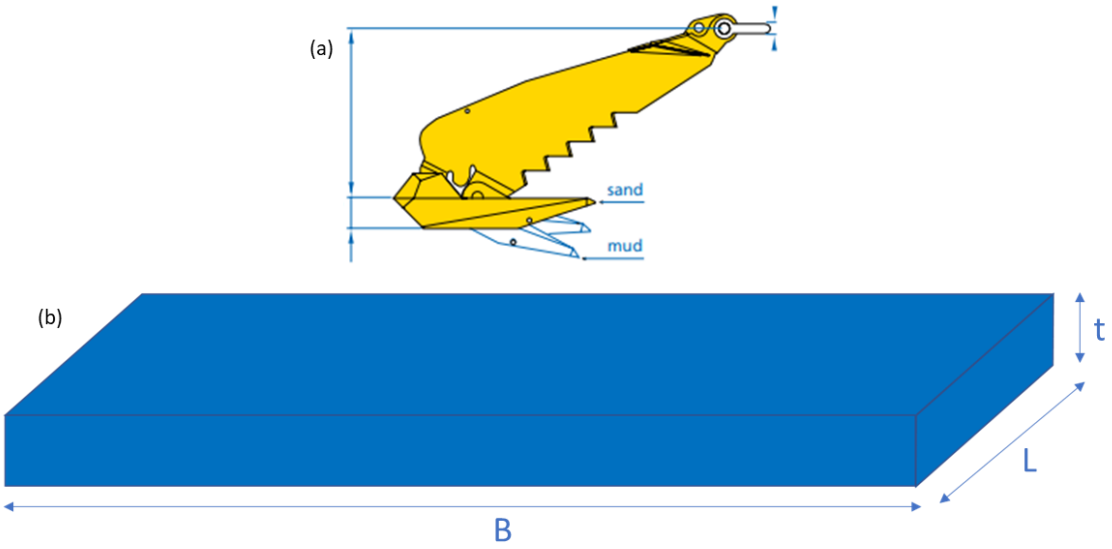

Figure 4.1: Sketches of (a) the Stevpris Mk5 (source: VRYHOF 2018) and (b) the equivalent plate.

The Finite Element domain is presented in **Figure 4.2**. Preliminary analyses indicate that the appropriate domain size spans twelve times the anchor width (12B) in each direction relative to the anchor centroid, to avoid unwanted boundary effects. The soil thickness was set equal to six times the anchor width (6B) as it was found that increasing it didn't have any effect on the anchor behaviour. To reduce the computation need of the model, the y=0 plane was used as a plane of symmetry and thus only half of the domain was simulated. Therefore, the Finite Element domain has a length of 24B = 153.6m, a width of 12B = 76.8m and height of 6B = 38.4m. The water table is placed 1m above the soil surface as placing it higher would make no difference to the effective stresses the soil experiences.

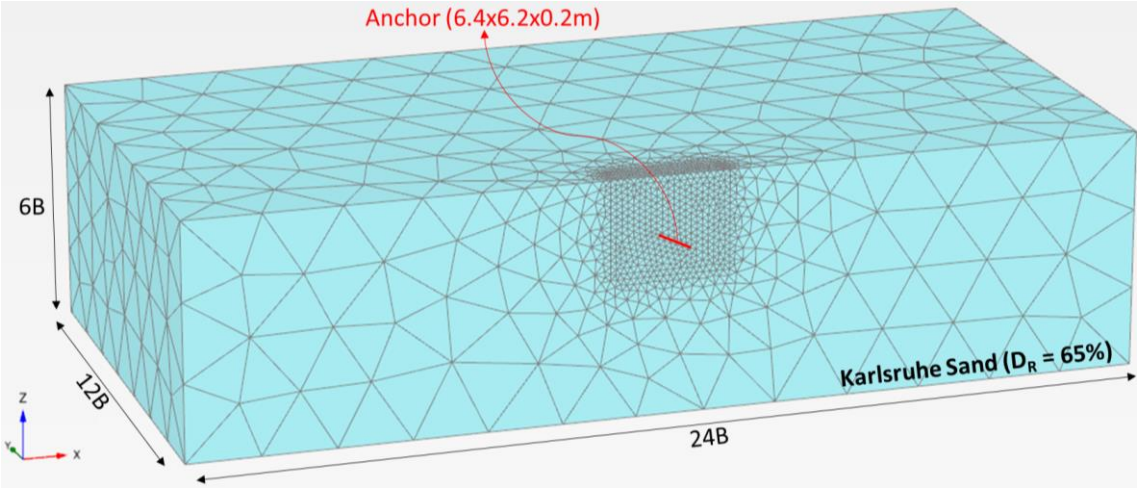

Figure 4.2: Three dimensional representation of the numerical model

Aiming to capture more accurately the anchor soil interaction, the mesh is denser in the area surrounding the anchor. More specifically, the element size is approximately B/6 = 1.07m close to the anchor and approximately 2B = 12.8m in the far field where the soil structure interaction effects will be less significant. The domain consists of approximately 12000 elements and 18000 nodes. Roller constrains were placed at the sides of the domain and hinge constrains at the base. The anchor is restricted from moving in the y axis direction and rotating around the x and z axis.

In preliminary analyses, the use of an interface between the plate and the soil was also examined. However, it was found that the anchor response was significantly affected by the choice of the interface stiffness parameters. Absence of any data to calibrate the interface parameters against, it was inferred that the results of the models without using an interface are more reliable and ultimately the use of an interface between the plate and the soil was rejected. The variation of the anchor response in terms of force displacement curve by altering the location of the fixed boundaries, the element size close to the anchor and the interface properties are included in the Appendix.

4.1.2 The SANISAND-MS constitutive model

As highlighted in Chapter 3, this Thesis will delve into investigating the behavior of a Drag Embedded Anchor (DEA) in connection with a floater via a mooring line of catenary shape. Throughout its operational lifespan, the anchor will be subjected to one-way cyclic loads. Within such loading conditions, the critical factor governing anchor response is the accumulation of shear strains. Developed to enhance the accurate simulation of (rate-independent) cyclic sand behavior, particularly concerning drained high-cyclic ratcheting and

the associated strain accumulation, the SANISAND-MS (Liu et al. 2019) constitutive model stands out as the most fitting choice for this Thesis.

The SANISAND-MS model is an advanced constitutive model used to predict the stress-strain response of granular soils under large numbers of repeated loading cycles. It is an extension of the SANISAND2004 model developed by Dafalias and Manzari (Dafalias and Manzari 2004). The primary enhancement in SANISAND-MS is the incorporation of a "memory surface" to replace the fabric tensor, as proposed by Corti et al. 2016. The model is based on the critical state framework, which is widely used to describe the stress-strain behavior of soils undergoing plastic deformations. The framework uses four critical loci to define the material's response:

1. Conical yield locus (f):

This encloses the elastic domain and represents the boundary beyond which plastic deformations occur. When the current stress state exceeds this locus, it evolves with the plastic strain increment due to the kinematic hardening formulation of the model.

2. Conical bounding surface (f^B):

The bounding surface sets the current stress bounds consistent with an evolving state parameter. This parameter is introduced to capture the evolving behavior of the material during loading and unloading, as proposed by Been and Jefferies 1985, and further developed by Manzari and Dafalias 1997.

3. Conical dilatancy surface (f^D):

This locus separates stress zones associated with contractive (volume reducing) and dilative (volume expanding) deformations.

Conical memory surface (f^M):

The memory surface is introduced to bound an evolving stress region associated with non-virgin loading. Non-virgin loading refers to loading paths that have been previously experienced by the material. The memory surface accounts for stress-induced anisotropy at the micro-scale, capturing micro-mechanical effects associated with changes in fabric (reorientation of particle contacts) during cyclic loading. This allows the model to represent variations in stiffness and dilatancy due to changes in the microstructure of the material.

The researchers that developed the SANISAND-MS constitutive model calibrated its parameters with Karlsruhe sand which is a medium-coarse quartz sand, and thus, the parameters of the soil surrounding the anchor that were selected to match this type of sand.

The initial relative density of the sand was selected to be D_R = 65% which corresponds to initial void ratio e_0 = 0.681 and saturated unit weight of the soil γ_{sat} = 19.44 kN/m^3. The specific gravity of the soil particles was assumed G_s = 2.65. The reference SANISAND-MS parameters for the Karlsruhe sand are presented in **Table 5** (Liu et al. 2022a).

Table 5: Karlsruhe sand's SANISAND-MS model parameters.

Elasticity		Critical state					Yield surface	Plastic modulus			Dilatancy		Memory surface		
G_0	ν	M_c	c	λ_c	e_0	ξ	m	h_0	c_h	n^b	A_0	n^d	μ_0	ζ	β
110	0.05	1.27	0.71	0.05	0.85	0.27	0.01	5.95	1.01	2	1.06	1.17	260	0.0005	1

4.1.3 Loading Stages

The geometry presented in **Figure 4.3** serves as a general representation of the problem under examination. All mentions of applied load pertain to the load acting on the anchor at the padeye level, denoted as T_a unless expressly stated otherwise. In all loading stages the load inclination at the padeye θ_α is assumed to be constant. This load is applied at the anchor's centroid, with the resultant of the horizontal and vertical components, F_x and F_y, being equivalent to T_a. Additionally, a moment M is introduced, accounting for the specified eccentricities e_p and e_n, as indicated in equation 4-1 adapted from (Tian et al. 2015).

$$M = T_a\left[e_n \cdot \cos\left(\pi - \beta - \vartheta_\alpha\right) + e_p \cdot \sin\left(\pi - \beta - \vartheta_\alpha\right)\right] \qquad 4\text{-}1$$

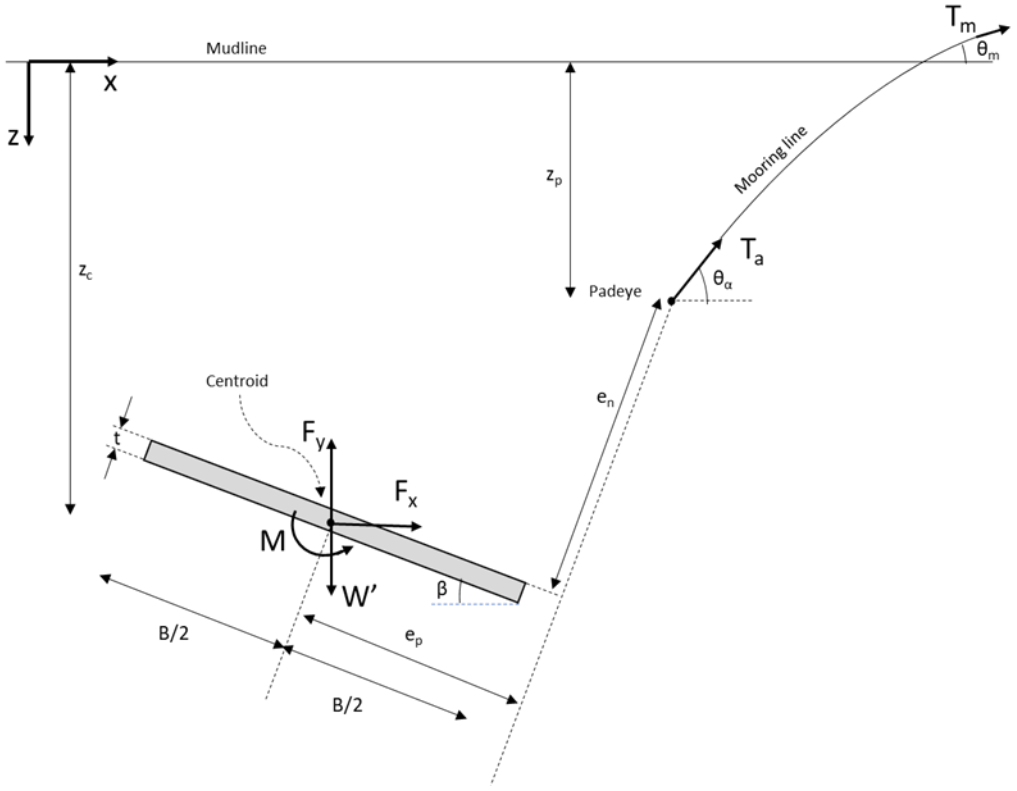

Figure 4.3: Geometric details and loads acting on the anchor and chain (not in scale).

In all the numerical analyses, the anchor is subjected to one of the following loading stages.

Stage I: Static Monotonic Load

In this stage, the anchor is subjected to a gradually increasing load in a single direction until either the prescribed value is reached, or failure occurs (**Figure 4.4** left). For each loading step, the deformations and stresses at points of interest are recorded. This stage helps estimate the holding capacity of the anchor at different initial positions in Chapter 5.

Stage II: Static Cyclic Load

In this stage, the anchor experiences one-way cyclic loading, which involves alternating between minimum and maximum load values for a predetermined number of cycles. Each cycle is divided into two phases: loading and unloading. The loading phase involves applying an increasing load up to the maximum value, as in Stage I. The unloading phase involves decreasing the load back to the minimum value (**Figure 4.4** right). This stage is utilized in Chapter 6.

As the Thesis examines the behaviour of a DEA in sand, fully drained loading conditions are assumed in both loading stages. This is motivated by the high hydraulic conductivity of sandy soils, which limits excess pore pressure generation during loading.

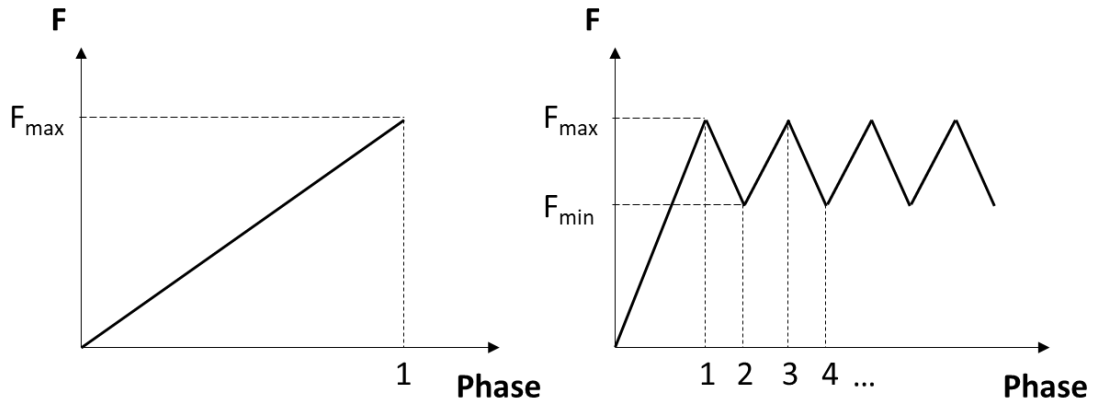

Figure 4.4: Schematic representation of the applied loading stages.

4.2 Initial Anchor Position

4.2.1 Performance of embedded anchor chains

As previously stated, the mooring line is attached to the anchor at the padeye. During installation, the other end of the mooring line is being pulled by an Anchor Handling Vessel (AHV) which causes the anchor fluke to penetrate the soil. Part of the chain also embeds, causing frictional and normal forces to act on the embedded section of the chain. Due to these forces, the chain forms a reverse catenary shape from the anchor attachment point to the seabed. This phenomenon impacts the load transferred to the anchor in two ways. Firstly, the frictional forces acting on the chain reduce the load that acts on the anchor. Secondly, the load on the anchor padeye is not horizontal but at an angle θ_α to the horizontal which means that there is a vertical component to the load (**Figure 4.5**).

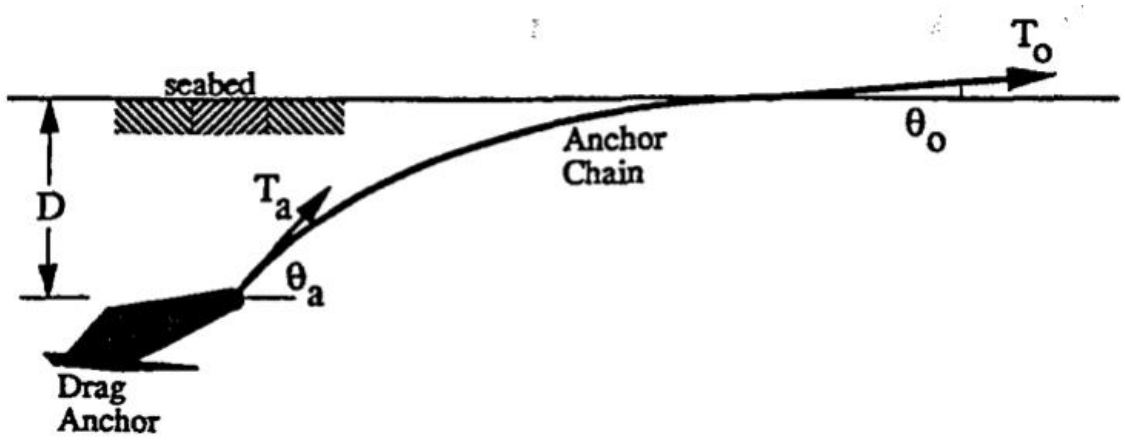

Figure 4.5: Reverse catenary shape of the embedded chain. (source: Neubecker Randolph,. 1995)

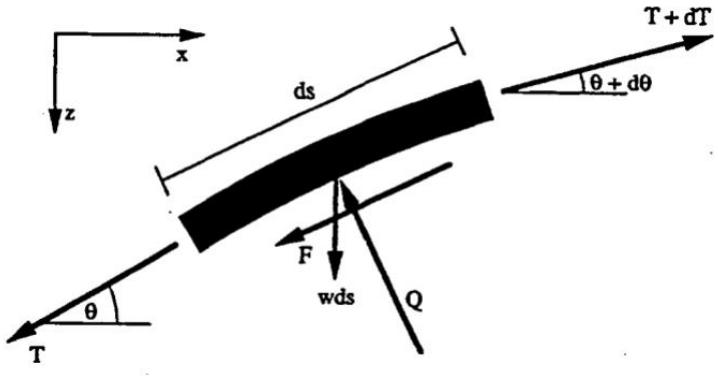

Figure 4.6: Force equilibrium on a chain element. (source: Neubecker Randolph,. 1995)

Vivatrat et al. 1982 derived the force equilibrium differential equations for a chain element (Equations 3-2 and 3-3). In these equations, T is the tension in the chain, θ is the angle of the chain relative to the horizontal, s is the distance along the chain measured from the padeye, F

and Q are the tangential and normal soil reaction forces per unit length of the chain and w is the buoyant chain self-weight. An iteration procedure is utilized to solve the system where for a given chain tension T_a, a chain angle θ_a is initially assumed. The equations are then integrated over the embedment depth D and give an estimation for the angle at the mudline level θ_o. Variations of the chain angle θ_a are performed until the intended angle at the mudline level θ_o is reached.

$$\frac{dT}{ds} = F + w \cdot \sin\theta \qquad 4\text{-}2$$

$$T\frac{d\theta}{ds} = -Q + w \cdot \cos\theta \qquad 4\text{-}3$$

For many years the solution of the chain system involved solving the governing set of differential equations proposed by Vivatrat et al. 1982 which was computationally very expensive. Neubecker and Randolph 1995 were able to convert it into a system of analytical solutions based on the following assumptions:

- The ultimate normal resistance is given by the expression:

$$Q_u = E_n \cdot d_b \cdot q \qquad 4\text{-}4$$

  where E_n is a multiplier to give the effective width in the normal direction and d_b is the diameter of the steel used to fabricate the chain.

- The soil normal pressure is given by the following expression:

$$q = N_q \cdot \gamma' \cdot z \qquad 4\text{-}5$$

  where N_q is a bearing capacity factor and γ' is the effective unit weight of the soil.

- The ultimate normal Q_u and frictional F_u resistance is mobilized simultaneously.
- The self-weight of the chain can be ignored.

They concluded the following set of equations:

$$T = T_a \cdot e^{\mu(\theta_a - \theta)} \qquad 4\text{-}6$$

$$\frac{-T_a}{1+\mu^2}\left[e^{\mu(\theta_a-\theta)}\left(\cos\theta + \mu \cdot \sin\theta\right)\right]_{\theta}^{\theta_a} = \int_z^D Q dz \qquad 4\text{-}7$$

Where μ is the ratio of the frictional over the normal soil resistance and D is the embedment depth.

4.2.2 Analytical models for simulating the installation trajectory of a DEA

Significant research has been performed in predicting the trajectory of the drag anchor during installation in cohesive soils including centrifuge test, finite element simulations and analytical methodologies. Of interest to this Thesis is the work of (Neubecker and Randolph 1995) in which they proposed a methodology to predict the installation trajectory and the magnitude and angle of the ultimate load in clays. Their work assumes that while the anchor is dragged, it will move parallel to the fluke and simultaneously rotate until the fluke becomes horizontal. After this point, the anchor stops rotating and moves only in the horizontal direction as it has mobilized its full capacity. This assumption is widely accepted in literature to this day.

To get the anchor embedment history, the anchor is incrementally advanced, assuming motion parallel to the fluke, and the rotation is determined based on moment equilibrium. At any embedment depth, the local soil strength and projected areas of the shank and fluke are used to estimate the anchor resistance. The chain solution presented in Equations 4-6 and 4-7 is employed in each step to calculate the load angle θ_a at the anchor padeye. The resistance of a weightless anchor T_w can be analyzed into two components, normal (T_n) and parallel (T_p) to the fluke as depicted in **Figure 4.7**. The anchor capacity can be calculated according to Equation 4-8.

$$T_w = \frac{f \cdot N_c \cdot A_p \cdot S_u}{\cos \vartheta_w} \qquad 4\text{-}8$$

With A_p being the anchor projected area in the direction of motion, N_c is a bearing capacity factor and f is the form factor of the anchor. The angle of the resultant T_w to the fluke θ_w is assumed to be a geometric characteristic of the anchor. However, during embedment, the anchor will be at an angle β to the horizontal and the anchor capacity T_a will be influenced by the anchor weight W. This leads to a modified resultant angle θ_w' which is related to β with the following expression:

$$\vartheta_a = \vartheta_w' - \beta \qquad 4\text{-}9$$

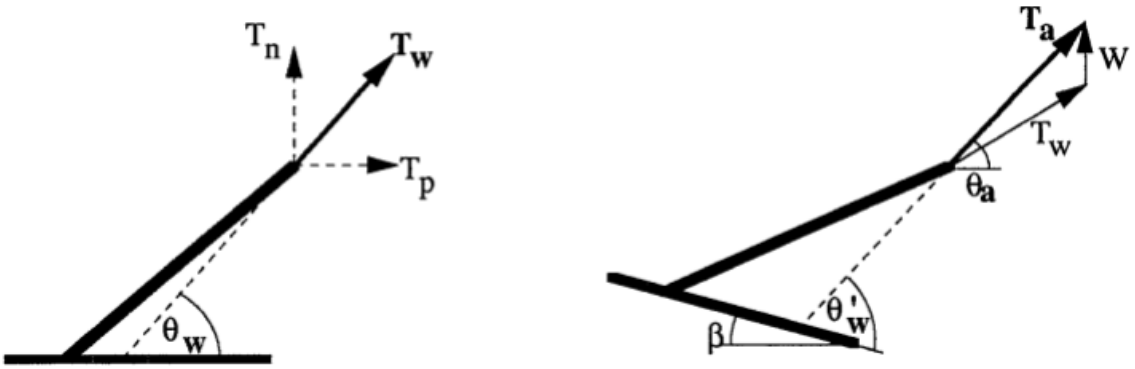

Figure 4.7: Resistance components of a weightless anchor (left) and a rotated "weighty" anchor (right). (source: Neubecker Randolph,. 1995)

Their methodology can be summed up in the following steps:

1. Assume an initial anchor position (depth and orientation) and advance the anchor by a horizontal increment dx.

2. Assuming the anchor will move parallel to the fluke, calculate the new embedment depth.

3. The anchor resistance T_a is calculated as the resultant of the resistance of a weightless anchor T_w and the anchor weight W (See **Figure 4.7**). Its orientation θ_w' can also be derived.

4. The load angle at the padeye can be calculated using the chain solution (Equation 4-7).

5. The new anchor angle to the horizontal can be calculated utilizing Equation 4-9.

6. Advance the anchor by another dx and go to step 2.

The anchor will follow a path as presented in **Figure 4.8**.

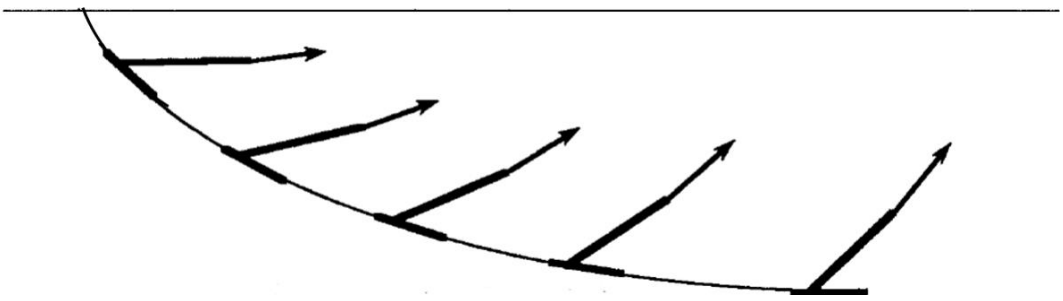

Figure 4.8: Anchor resistence and embedment trajectory. (source: Neubecker and Randolph 1995)

The advantage of this methodology is that is gives an estimate of the complete anchor embedment trajectory, anchor orientation and load inclination at the padeye. However, it requires the calibration of the soil resistance angle to the fluke θ_w and the anchor form factor f.

Moreover, useful to this Thesis is the work of Tian et al. 2015. Defining the problem geometry similar to **Figure 4.3**, they proposed a solution for the ultimate embedment depth and the ultimate holding capacity of a drag anchor in cohesive soil by making the following assumptions:

- As the anchor embeds, the chain pulling angle will gradually increase and thus there will be a point in the installation where the vertical component of the load will not allow the anchor to dive any further.
- At the ultimate embedment depth, the vector of the chain load passes through the rotation center of the anchor and hence, no moment acts on the anchor.
- All the loads act on the anchor centroid which is also assumed to be the rotational center.
- The anchor displacements increment, equal to the incremental plastic displacement due to the rigid plastic assumption, can be calculated, due to the assumption of normality, by differentiating the yield surface.

Utilizing the chain solution of (Neubecker Randolph,. 1995) and the yield locus of Bransby and O'Neill 1999 they were able to put together a set of five simultaneous equations with five unknowns. This non-linear equation can be solved numerically by means of a Newton-Raphson iterative scheme. The yield locus adopted is of the following form:

$$f = \left(\frac{N_n}{N_{n,\max}} \right)^q + \left[\left(\frac{N_m}{N_{m,\max}} \right)^m + \left(\frac{N_s}{N_{s,\max}} \right)^n \right]^{1/p} = 1 \qquad 4\text{-}10$$

Where N_n, N_s, N_m are the normalized normal, sliding and moment loads that act on the anchor centroid. The parameters p, q, n and m are dimensionless.

While this methodology focuses solely on the ultimate state and doesn't provide any insight regarding the installation history that led to equilibrium, it is very powerful as the user only has to define the yield locus parameters. These parameters can be taken directly from the literature according to the anchor geometry. Notice that the parameters $N_{m,max}$ and m don't need to be given values as N_m is assumed to be nil at the ultimate state.

4.2.3 Prediction of the Installation trajectory of the 65t Stevpris Mk5

The methodologies presented in the previous sections, have been coded with Python and are used in this Chapter to predict the embedment history of the selected anchor. The parameters needed were selected based on recommendations available in the international literature.

More specifically, from the critical state line slope for compression in the q-p' space M_c = 1.27, the critical state friction angle ϕ can be derived to be equal to 31.6°. According to Day 2006, who offers a N_q-ϕ relationship curve, this friction angle corresponds to a bearing capacity factor N_q = 23. The For calculating the soil resistance in Equation 4-8, the term $N_c \times S_u$ was replaced by $N_q \times \gamma' \times z$ (Equation 4-5) for use in sandy soils as per Neubecker Randolph, 1995.

Kulhawy, 1983 claim that the interface friction angle δ can be taken as 0.5-0.7 times the soil friction angle and thus δ = 0.6ϕ = 19°. For solving the chain solution, the friction ratio μ is taken equal to the tangent of the interface friction angle (Peng and Liu 2019), therefore μ = 0.34. The chain effective width E_n is taken equal to 2.5 even though this value was derived from centrifuge test in clay due to lack of proposed values for sand (Degenkamp and Dutta 1990). The yield locus parameters (Equation 4-10) were adapted from Elkhatib 2006 and are presented in **Table 6**.

Table 6: Yield contour parameters.

$N_{n,max}$	11.93	-
$N_{s,max}$	4.65	-
p	1.27	-
q	3.93	-
n	3.44	-

The methodology from (Tian et al. 2015) gives for the ultimate state:

- Normalized embedment depth, z_c / B = 3.60
- Load angle at the padeye, θ_a = 41.24°

To use the methodology of (Neubecker and Randolph 1995), the form factor f and angle of the soil resistance force θ_w were set equal to 0.86 and 35.4° respectively in order to match the prediction of the ultimate state to the results from Tian. **Figure 4.9** presents the evolution of the anchor position and anchor orientation β during the installation of the 65t Mk5 Stevpris anchor. It is clear from the plots that the anchor embeds into the soil and simultaneously rotates, which is expected based on the imposed boundary conditions. It should be noted that the drag distance required for the anchor to reach the ultimate state is about 30 times its width. At that ultimate state the anchor has a zero degree inclination and moves strictly horizontally. **Figure 4.10** shows the evolution of the load angle at the padeye. The angle increases as the anchor penetrates deeper, thus increasing the vertical component of the load and ultimately prohibiting the anchor from moving to greater depth.

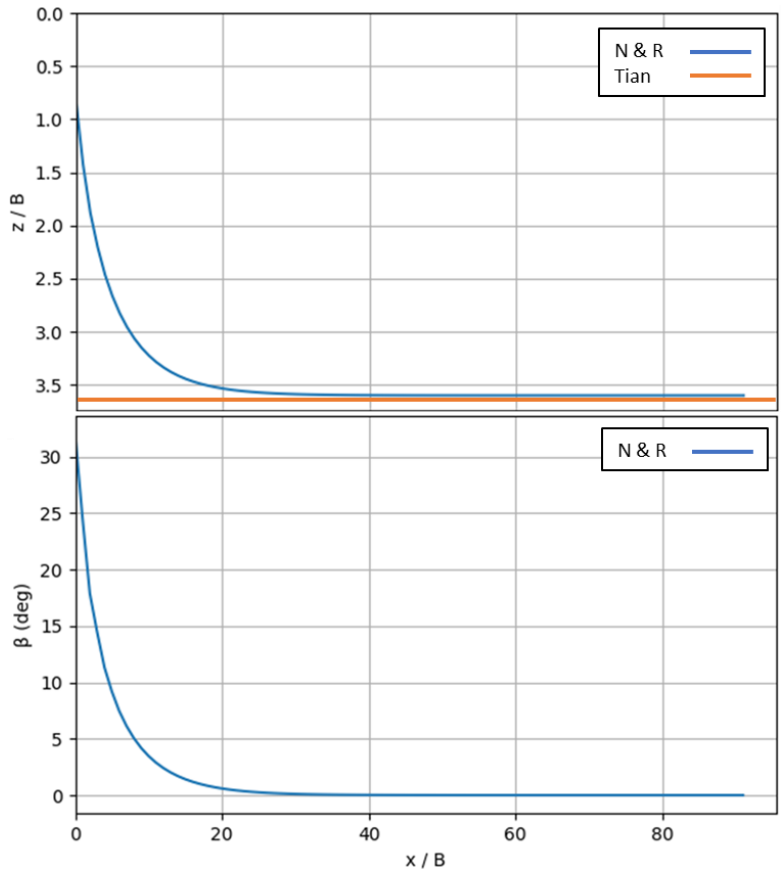

Figure 4.9: Anchor trajectory (top) and orientation (bottom) during installation. N & R stands for prediction of Neubecker and Randolph 1995, Tian stands for prediction of Tian et al. 2015.

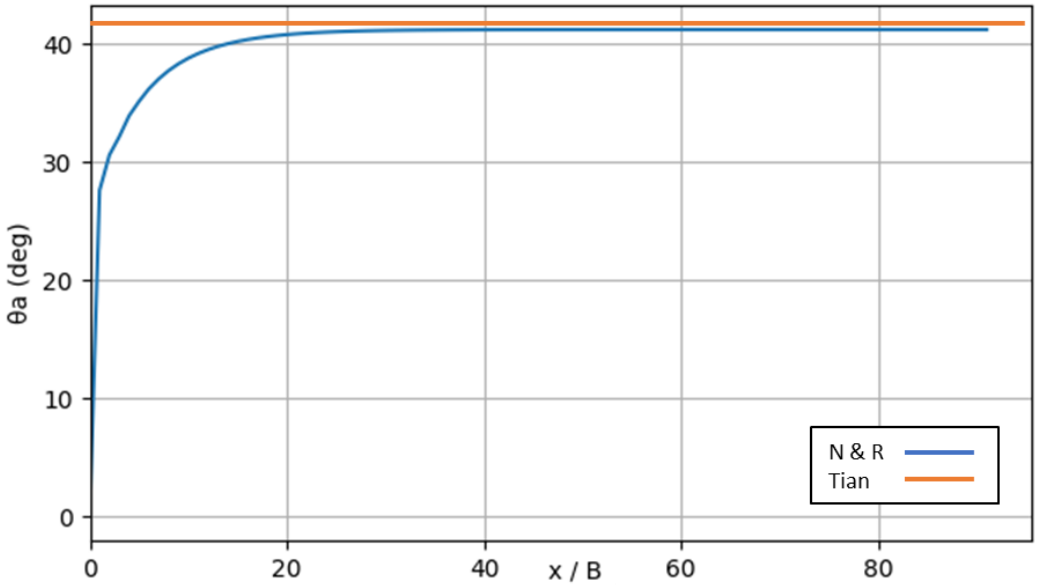

Figure 4.10: Load angle at the padeye (top) and load magnitute (bottom) during installation. N & R stands for prediction of Neubecker and Randolph 1995, Tian stands for prediction of Tian et al. 2015.

Having established the above, it is clear that the initial conditions of the anchor in terms of initial depth and orientation can't be arbitrarily selected but should be consistent with the

trajectory presented in **Figure 4.9**. Additionally, the load angle at the padeye should be selected according to **Figure 4.10**.

4.3 Chapter Summary

The numerical model used for all analyses was presented in this Chapter. The appropriate domain size has dimensions 24Bx12Bx6B and the mesh is denser closer to the anchor. The anchor's complex geometry is simplified, and an equivalent two dimensional rigid plate with 6.4m width and 6.2m length is employed. For the soil surrounding the anchor, the advanced numerical model SANISAND-MS is used, deemed fit to capture the cyclic sand behavior. The sand was assigned properties corresponding to Karlsruhe sand (Liu et al. 2022a). The soil plate interface was assumed fully bonded due to lack of measured data for calibrating interface properties.

The initial conditions of the anchor are selected according to the methodologies of Tian et al. 2015 and Neubecker and Randolph 1995. Tian gives a solution for the ultimate state for the anchor and Neubecker & Randolph give a solution for the installation trajectory but requires calibration of the form factor f and the soil resistance force θ_w. The two parameters were chosen so that both methodologies predict the same ultimate depth. The anchor is subjected to either static monotonic load (Load Stage I) or static cyclic load (Load Stage II).

Chapter 5

Results – Static Monotonic Load

5.1 Typical Results

In this chapter, the anchor undergoes load stage I, which involves an incremental increase of the applied load until reaching failure. Within this section, the results of the analysis are presented, specifically when the anchor is initially positioned at 47% of its ultimate embedment depth ($z_c/z_{c,max}$ = 47%). As described in Chapter 4, the anchor has an inclination of 22.87° and its centroid is located 10.81m below the mudline. The load angle at the padeye is 27.7°. The results will be discussed in terms of anchor movement, soil behaviour around the anchor and force displacement curve. **Figure 5.1** illustrates the anchor's orientation during the initial and final steps of the analysis. The final position corresponds to an applied load of 25500 kN. It is noticeable that there is a displacement towards the positive x-direction, which is logical as there is a positive horizontal load component.

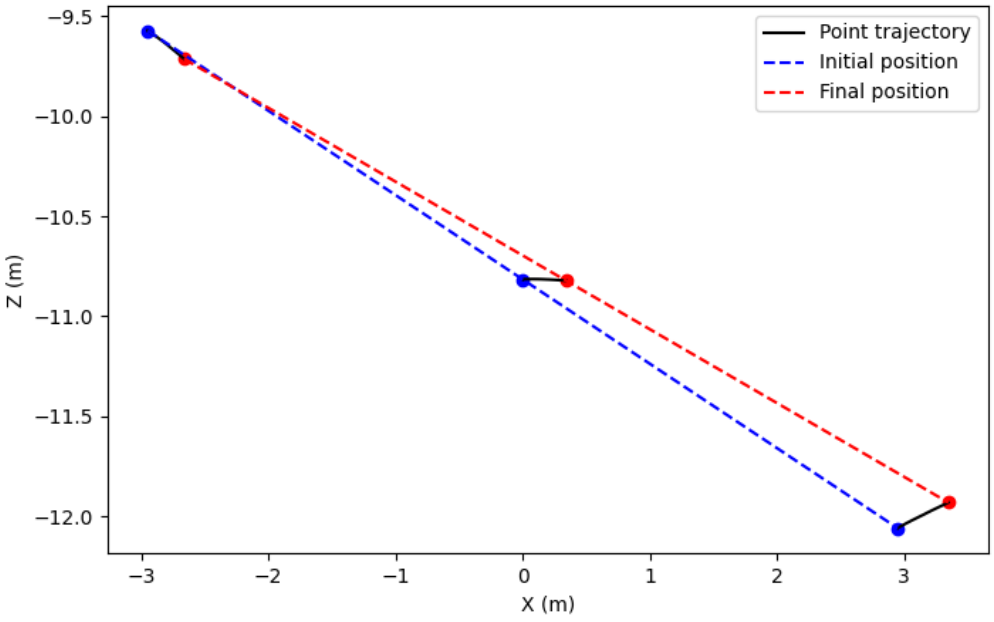

Figure 5.1: Anchor position at the first and last load step.

Figure 5.2 displays the progressive change in the anchor's angle concerning the horizontal axis, along with the centroid's coordinates evolution. The anchor's angle, exhibits a consistent linear decline, shifting by approximately one degree every 13 cm. As for the centroid, it initially moves upwards for the first 10 cm, then shifts downward movement and to the right at an angle of around 1 degree relative to the horizontal. From a qualitative point of view, this aligns with the predictions of the analytical methodologies as the anchor has in general a downward moving trend and simultaneously rotates. From a quantitative point of view, the rotation is highly overestimated as it implies that the anchor would be completely horizontal for small horizontal displacements. This is attributed to the fact that while the anchor rotates, the load angle at the padeye θ_α must evolve to account for the updated anchor geometry. However, this feature was not possible to implement into the numerical analyses and θ_α remained constant.

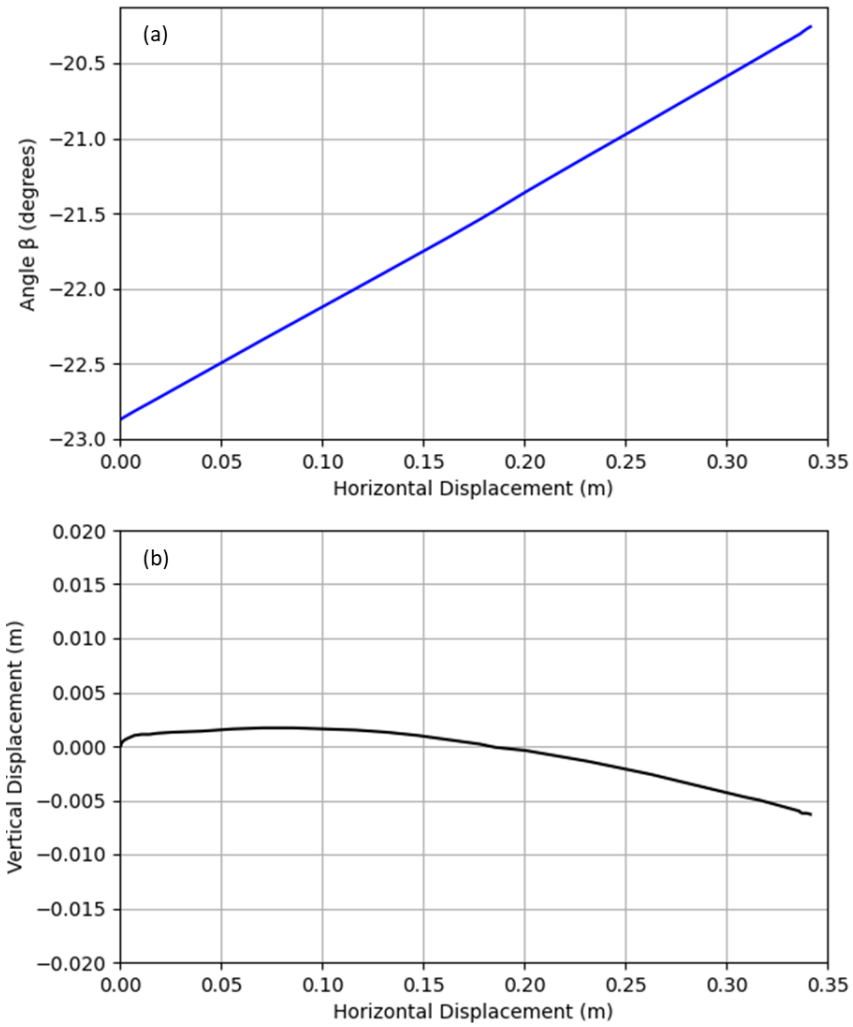

Figure 5.2: (a) Anchor orientation and (b) centroid position.

This shift from upward to downward motion can be explained by examining the evolution of the instantaneous center of rotation (ICR) of the anchor, as presented in **Figure 5.3**. Initially, the anchor rotates around a point situated on the rear side of the centroid, leading to an upward movement of the centroid. However, as the ICR progressively shifts towards the positive x-direction, it comes ahead of the centroid, inducing a downward movement. As will be elaborated later in this Chapter, the initial upwards anchor movement compresses the soil in the above the anchor and close to the fluke front. Consequently, it becomes easier for the anchor to penetrate deeper than further compress the soil above it which shifts the ICR forward and results in a downwards anchor movement. This is a direct result of the anchor being "wished in place" initial conditions.

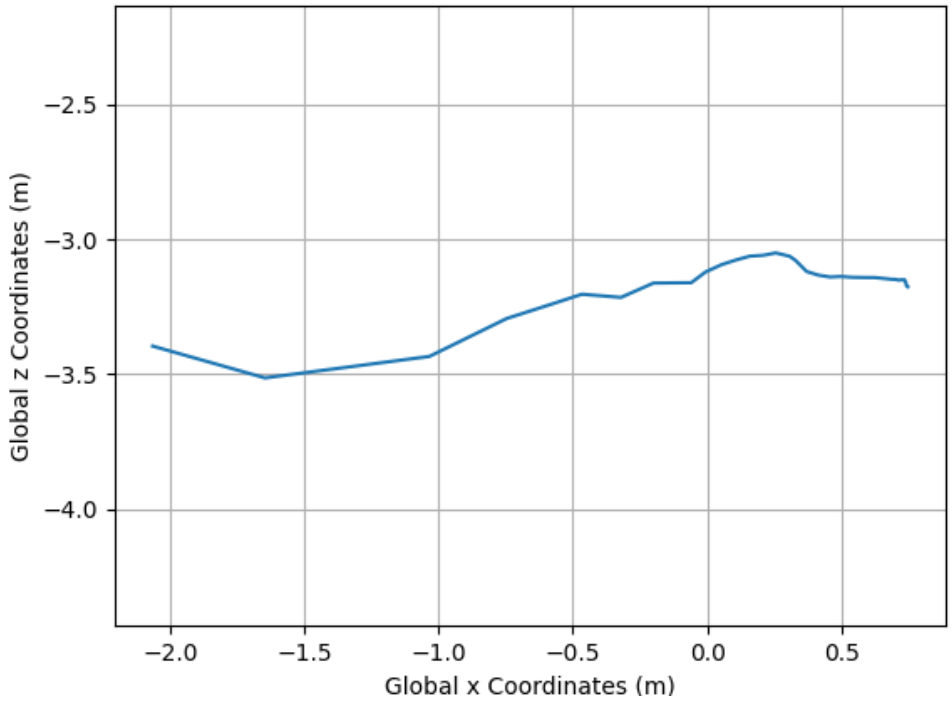

Figure 5.3: ICR coordinates evolution.

Figure 5.4 depicts the total displacement vectors of the soil surrounding the anchor. It can be observed that there is a movement component perpendicular to the fluke that extends to the mudline. This observation is consistent with the findings of Zhang et al. 2023 for a DEA at shallow depth. Above the anchor, in the area close to the front of the fluke, the soil moves predominantly in alignment with the loading direction. Still above the anchor but in the area close to the back of the fluke, the soil tends to fil the void created. This results in an almost circular soil movement around a point a few meters below the mudline.

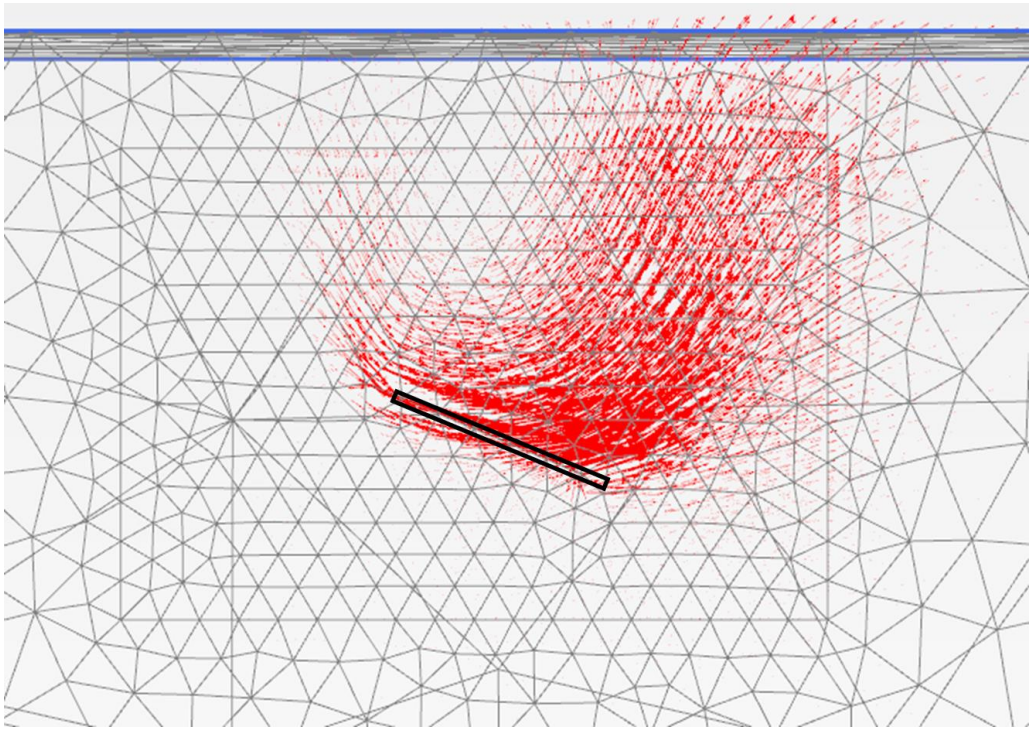

Figure 5.4: Total displacement vectors.

The contours illustrating the total deviatoric strain γ_s and principal effective stress σ_3', presented in **Figure 5.5**, further support this observation. The deviatoric strains contour reveals the formation of a failure surface that extends to the mudline. Moreover, the principal effective stress σ_3' contour exhibits a concentration of compressive stresses above the anchor in the direction of loading. Below the anchor the soil is unloaded.

Considering the shape of the failure surface in **Figure 5.5**, the direction of soil movement shown in **Figure 5.4**, and the anchor movement shown in **Figure 5.1**, the following conclusions can be drawn:

- As the anchor load increases, the anchor will experience horizontal movement with a slight upward movement and gradual rotation towards a more horizontal orientation.
- The anchor movement and rotation results in different soil behaviour around the anchor. Above the anchor, in the area close to the front of the fluke, the soil moves predominantly in alignment with the loading direction. Still above the anchor but in the area close to the back of the fluke, the soil tends to fil the void created. The failure surface that is formed extends all the way to the mudline suggesting a shallow failure mechanism.
- Above the anchor, in the area close to the front of the fluke, there is significant concentration of compressive stresses. Above the anchor, in the area close to the back

of the fluke the soil is unloaded. The soil below the anchor is also unloaded and increases its volume.

- A point is reached at which the anchor finds it easier to penetrate deeper in the soil than to further compress the soil above which results in a downwards anchor movement.

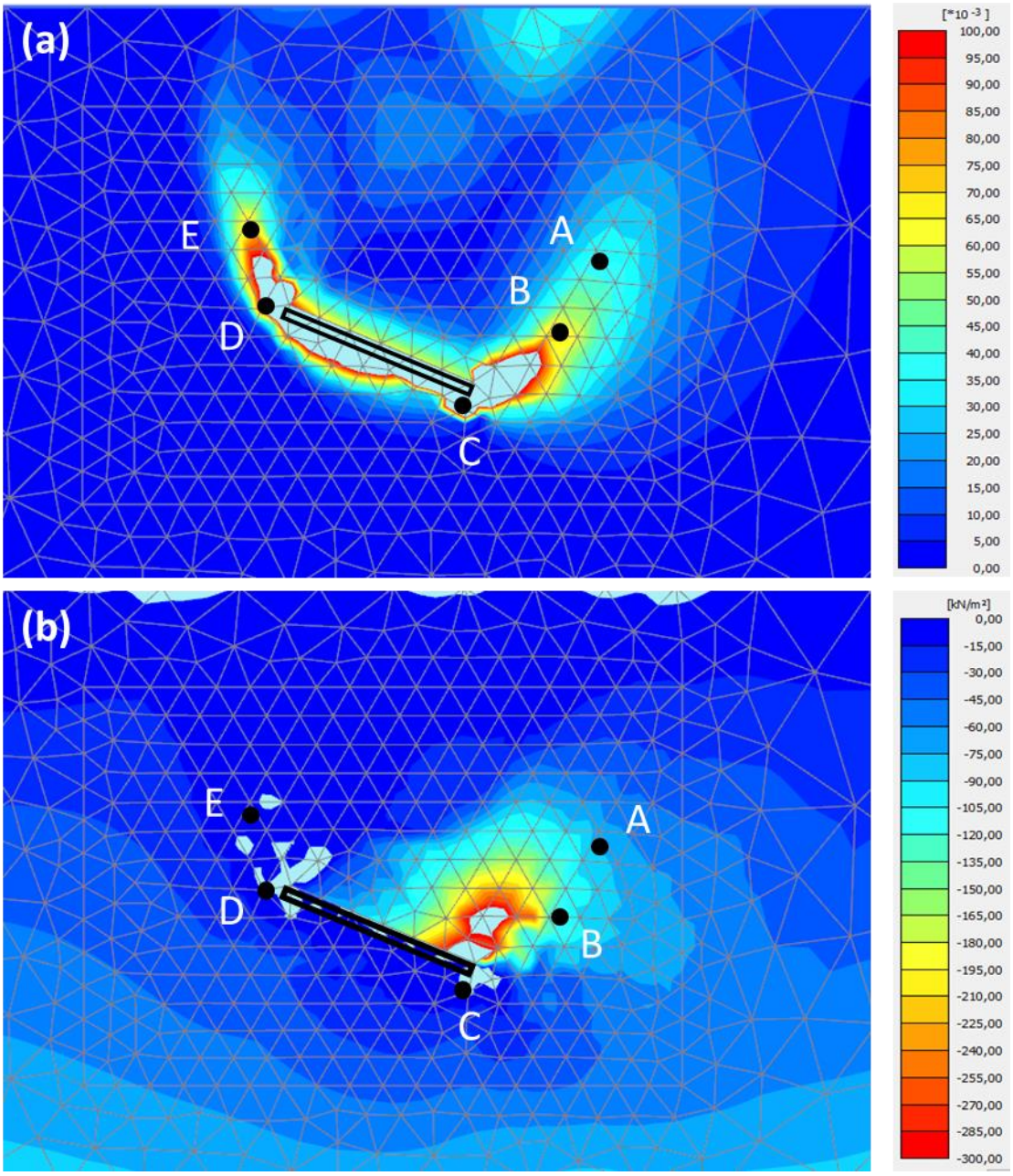

Figure 5.5: Contours of (a) total deviatoric strains γ_s and (b) principal effective stress σ_3' (negative values stand for compression).

To further investigate the soil behaviour, specific points have been chosen along the failure zone situated both above and below the anchor, as well as in both the frontal and rear regions

of the anchor. These designated points are illustrated in **Figure 5.5** and will subsequently be referred to as indicated in **Figure 5.6**.

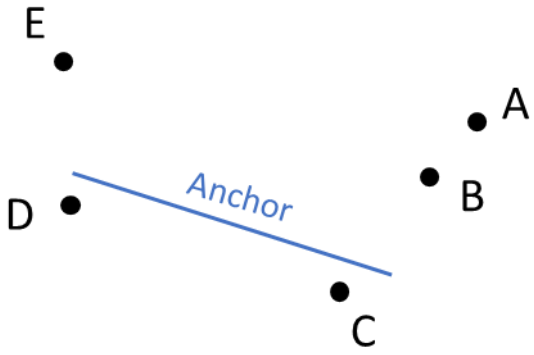

Figure 5.6: Schematic representation of the selected points of interest.

For the selected points, which are located close to the symmetry plane (y ≈ 0m), the following stress paths are depicted in **Figure 5.7**.

- Deviatoric stress, q – Deviatoric strains, ε_q
- Deviatoric stress, q – Mean effective stress, p'
- Void ratio, e - Mean effective stress, p'

Both points A and B experience linear increase in deviatoric stress followed by hardening as the applied load is increased. Point B, which is closer to the anchor, exhibits softening behaviour at the last loading steps. In the q – p' space, these points show stress increase that is close but doesn't follow the critical state line for compression, indicating that they are close to failure. Furthermore, they initially exhibit a slight decrease followed by a slight increase in void ratio. In the proximity of Point E, the soil shows a decrease both in deviatoric and mean effective stress. This unloading, induces an increase in volume locally.

Below the anchor, the response is similar both in front and behind the anchor as unloading occurs resulting to a slight increase in void ratio. Point D experiences a sort of dry liquefaction after which its volume increases under zero stress. This is attributed to the fact that the anchor is moving and thus relieving the soil below it from the pressure of the overburden soil. The stress paths are qualitatively similar when moving away from the boundary (y ≈ 3m), as indicated in **Figure 5.8** which displays the stress path of point A at y ≈ 0m and y ≈ 3m .

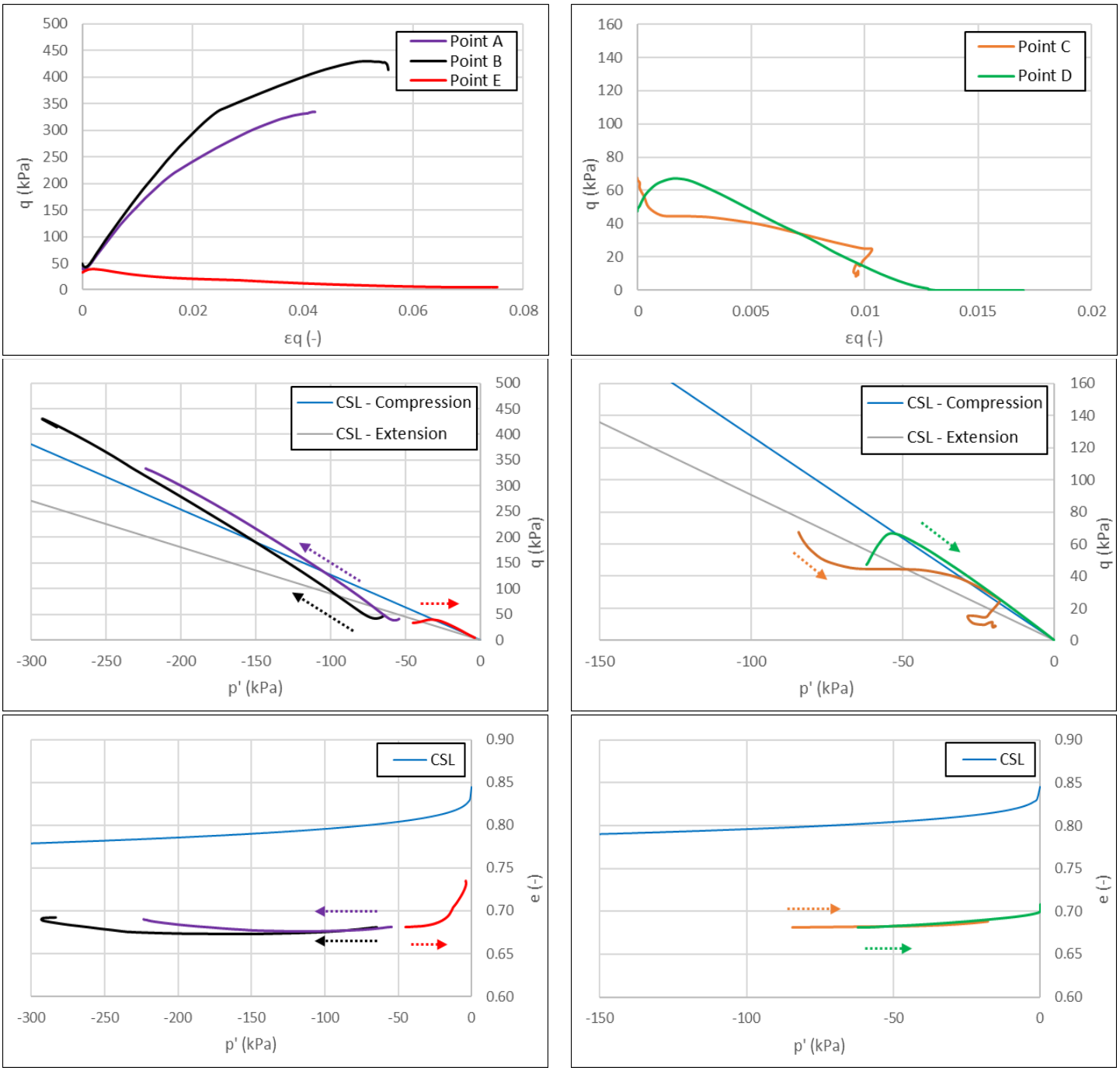

Figure 5.7: Stress paths of points above (left) and below (righ) of the anchor (negative values stand for compression).

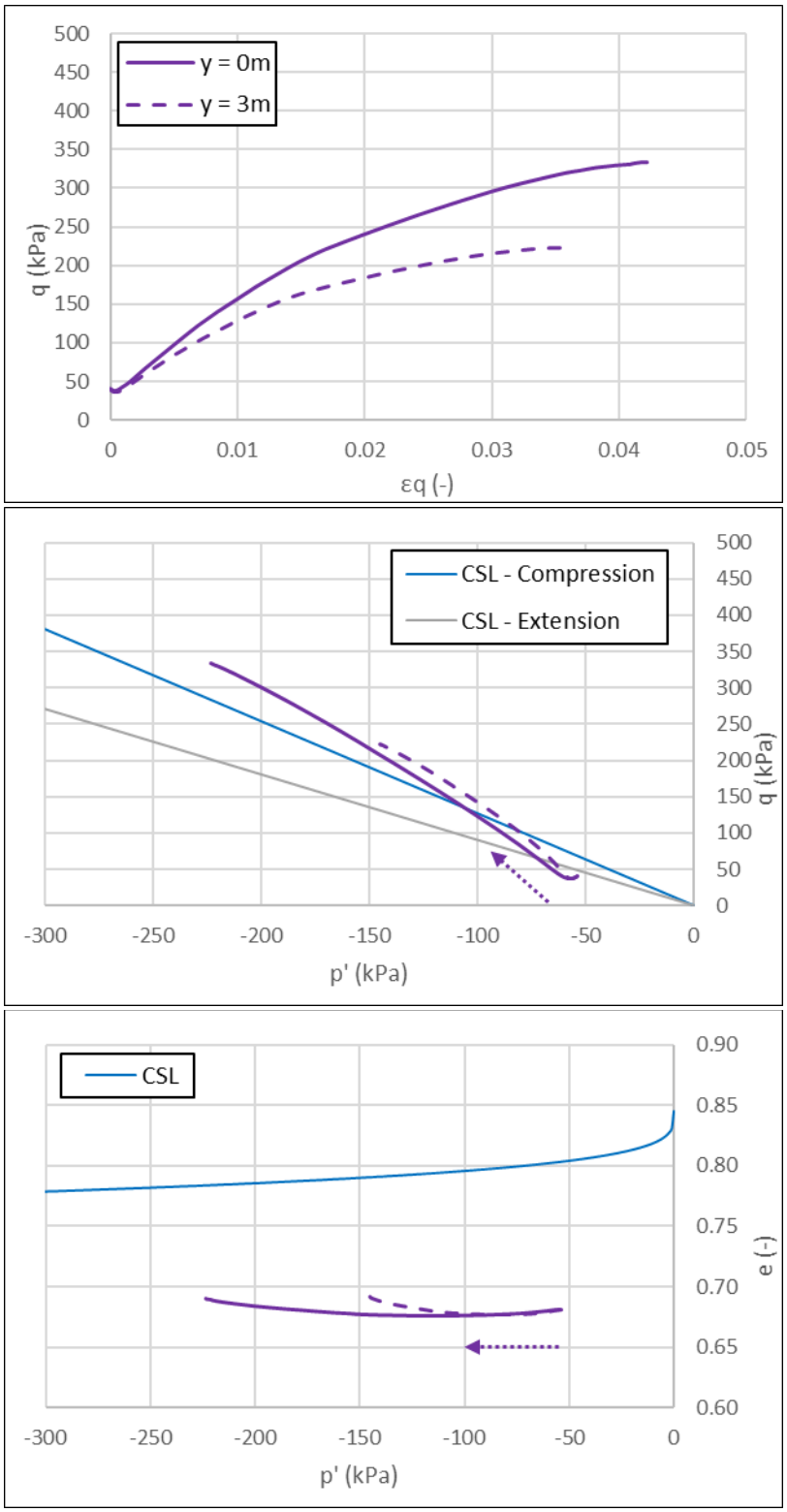

Figure 5.8: Stress path comparison of point A close and away from the symmetry plane (negative values stand for compression).

Figure 5.9 portrays the anchor centroid's horizontal displacement in relation to the applied force. The anchor shows non-linear behaviour at small displacements as the initial linear part is

barely noticeable. After yielding, the capacity continues to increase with the increase of accumulated displacement as the plastic domain expands.

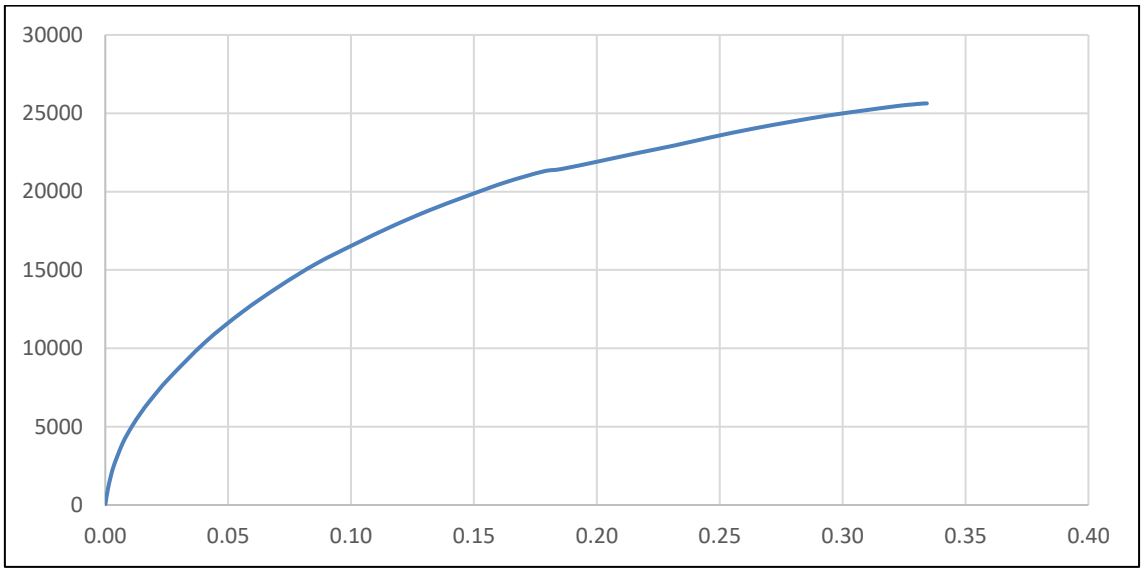

Figure 5.9: Force displacement curve.

5.2 An Expression for the Force-Displacement Curve

The scope of this Thesis is to identify appropriate analytical expressions that accurately describe the soil-anchor interaction of a DEA. Achieving this entails fitting various curves to align with the findings from Finite Element (FE) analyses. For a DEA subjected to monotonic load, the subsequent analytical models were investigated:

1. Linear Elastic – Perfectly Plastic (LEPP)

$$F = \begin{cases} K_{el} \cdot u & u < u_{yield} \\ K_{el} \cdot u_{yield} & u \geq u_{yield} \end{cases} \quad \text{5-1}$$

2. Bilinear

$$F = \begin{cases} K_{el} \cdot u & u < u_{yield} \\ K_{el} \cdot u_{yield} + K_{pl} \cdot \left(u - u_{yield}\right) & u \geq u_{yield} \end{cases} \quad \text{5-2}$$

3. Linear Elastic – Logarithmic (LEL)

$$F = \begin{cases} K_{el} \cdot u & u < u_{yield} \\ K_{el} \cdot u_{yield} \cdot \left[\ln \frac{u}{u_{yield}} + 1 \right] & u \geq u_{yield} \end{cases} \quad 5\text{-}3$$

4. Hyperbolic

$$F = \frac{u}{\frac{1}{K_{el}} + \frac{u}{P_u}} \quad 5\text{-}4$$

The LEPP and bilinear models are relatively simple models but could be of value due to their ease of implementation in several construction software applications. The LEL model, adapted from (di Prisco et al. 2018), has been proposed to describe the relationship between the pressure applied on the boundary of the tunnel cavity and the cavity convergence. The Hyperbolic model has found application in establishing backbone curves for piles (Lee et al. 2019). The parameters of each model that give the best fit have been identified using the Levenberg-Marquardt algorithm which is a variation of the least squares method designed specifically for nonlinear least squares problems. The parameter calibration was executed in Python utilizing the curve_fit function. The optimal parameter values for the anchor initially positioned at 47% of its ultimate depth, are presented in **Table 7**.

Table 7: Best fit parameters, $z_c/z_{c,max}$ = 47%

Parameter	LEPP	Bi-Linear	LEL	Hyperbolic	Units
K_{el}	193000	279000	317000	388000	kN/m
u_{yield}	0.114	0.049	0.021	-	m
K_{pl}	0	48600	-	-	kN/m
P_{ult}	-	-	-	30600	kN

The predicted force displacement curve for each of the examined models using their respective optimized parameters is presented in **Figure 5.10**. It becomes apparent that the LEPP model fails to capture the anchor's response effectively, with predictions significantly overestimating or underestimating the response across the entire range of applied force. On the other hand, the bilinear model appears to capture the response more accurately, although it falls short in predicting displacements within the load range of 10-15 MN and loads surpassing 25 MN. Additionally, it overestimates displacements between 17-22 MN.

The LEL and Hyperbolic models exhibit the best match as they accurately predict the anchor response for the whole range of applied load with the benefit of requiring calibration for only two parameters. It is therefore recommended to use either the Linear Elastic – Logarithmic model or the Hyperbolic model to predict the DEA response when subjected to monotonic load. In this Thesis the Linear Elastic – Logarithmic model is employed. Since this model assumes an infinitely expanding plastic domain, the capacity is defined as the force value at which the secant stiffness degradation reaches 90%.

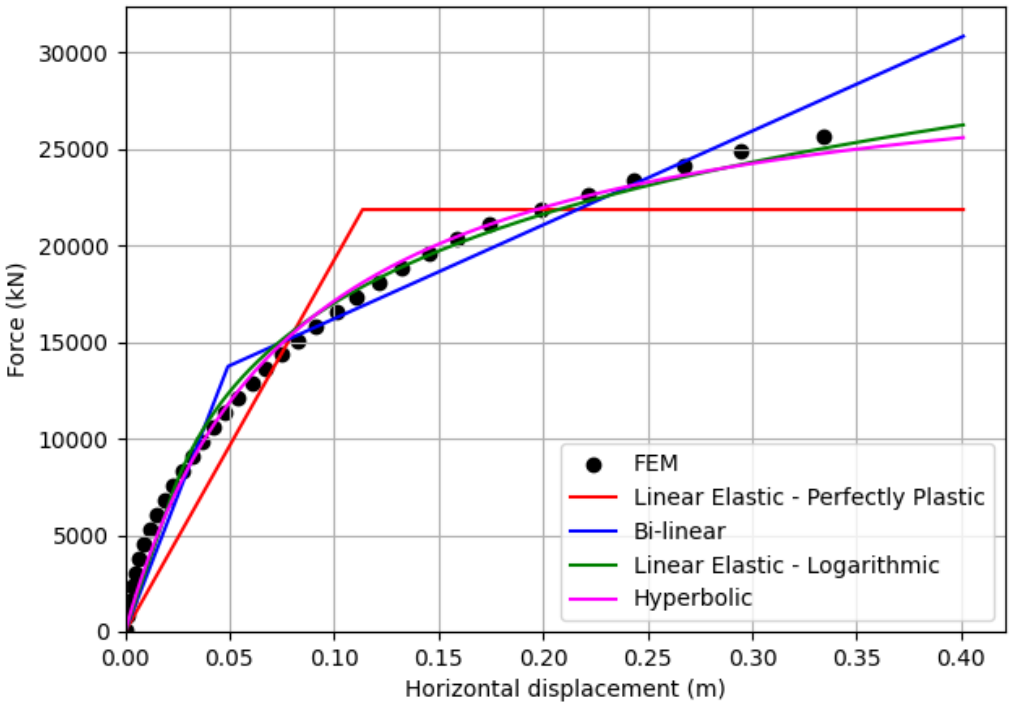

Figure 5.10: Comparison of best fit parameters between the analytical models.

5.3 Parametric Study

The FE analysis was repeated for different initial anchor positions. According to the results from Chapter 4, each depth is associated with a specific anchor inclination and a specific load angle at the padeye. The selected locations along the anchor installation trajectory and their corresponding anchor inclination and load angle are presented in **Table 8**.

Table 8: Details of the examined initial positions.

z_c / $z_{c,max}$ (%)	z_c / B	z_c (m)	θ_a (deg)	β (deg)
35	1.26	8.04	24.716	30.497
47	1.7	10.81	27.696	22.871
60	2.16	13.83	31.093	15.902
70	2.52	16.12	33.693	11.311
80	2.88	18.43	36.272	7.177
90	3.24	20.73	38.788	3.437
100	3.6	23.03	41.243	0

Figure 5.11 presents the force displacement curves obtained by performing load stage I at the locations indicated at **Table 8**. It is clear that by positioning the anchor deeper into the soil, the response becomes stiffer and the anchor is able to withstand higher loads for equal displacement levels. Moreover, the analytical expressions presented in the previous Section were fitted to the force displacement curves. Indicatively, the calibrated values of the Hyperbolic model are presented in **Figure 5.12**. Unsurprisingly, both the elastic stiffness K_{el} and the ultimate load p_u increase with depth. The best fit values for all the analytical model are included in the Appendix.

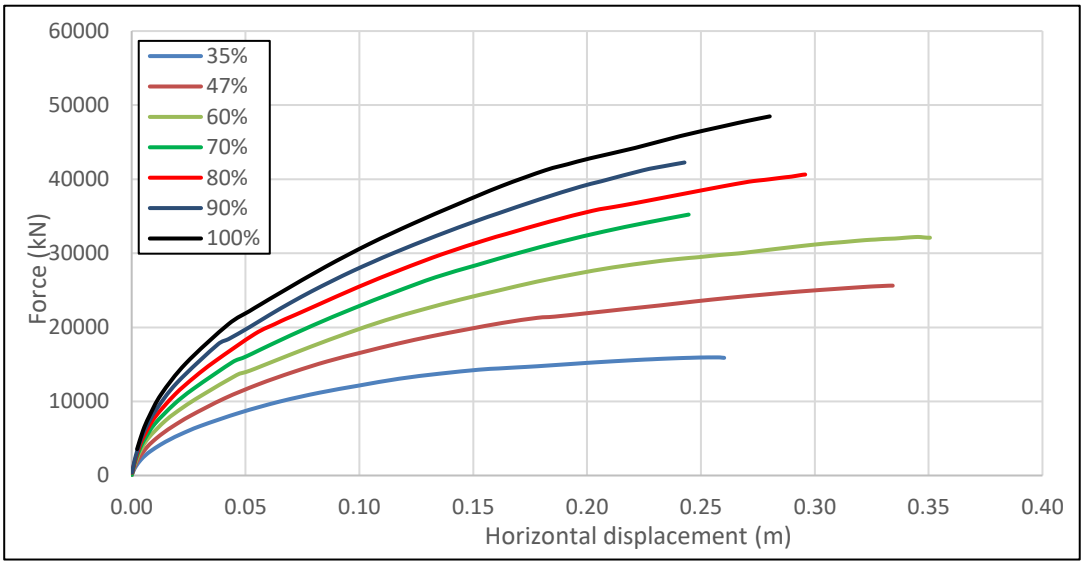

Figure 5.11: FEM obtained force displacement curves for different initial conditions.

Figure 5.13 presents the predicted holding capacity of the anchor from the FE analyses for all the examined locations, estimated by fitting the LEL model to the force displacement curves. The UHC of the anchor is 62.8 MN which is close to the prediction of Tian et al. 2015 at 54.3 MN. VRYHOF 2018 claims that 65t Stevpris Mk5 can bear loads equal to 34 MN at its ultimate depth which is almost half of what FE results indicate. However, Vryhof's design chart does not make any distinction between drained or undrained behaviour, static or dynamic loading or

even sand density. The definition of the anchor size is accompanied by a single value of ultimate holding capacity which could not possibly be true for all soil conditions. It is therefore concluded that no realistic comparison can be made.

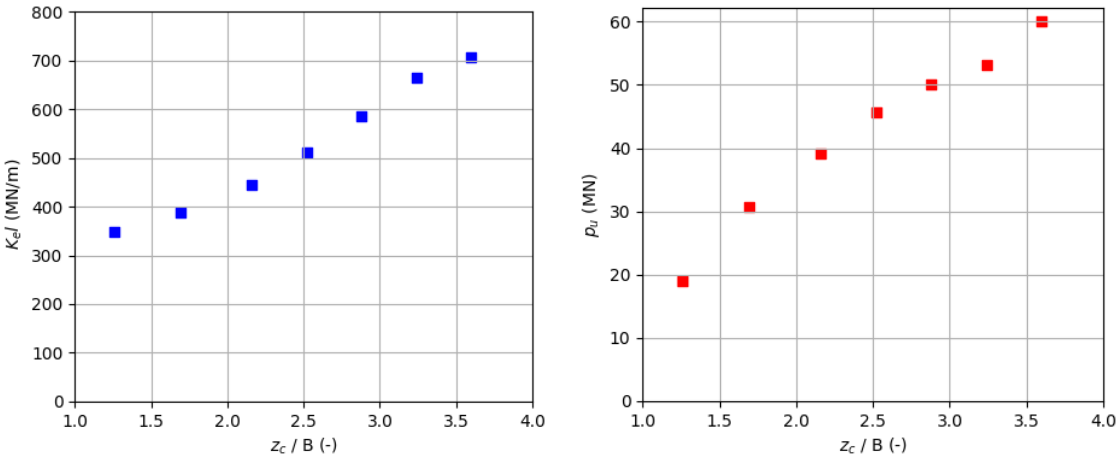

Figure 5.12: Influence of initial anchor depth on the hyperbolic model parameters.

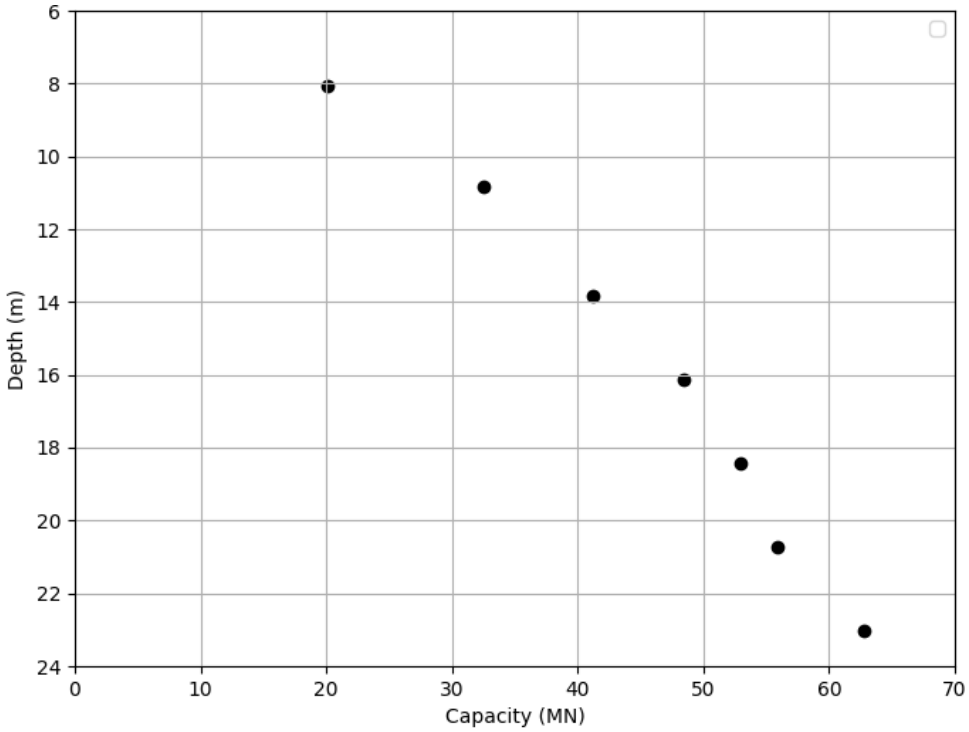

Figure 5.13: Ultimate holding capacity during installation.

5.4 Chapter Summary

In this Chapter, the anchor was subjected to static monotonic load. Results obtained for the analysis where the anchor was initially placed at a depth 47% of its ultimate depth were

presented and interpreted. The anchor's behaviour under monotonic loading can be summarized as follows:

- As the anchor load increases, the anchor will experience horizontal movement with a slight upward movement and gradual rotation towards a more horizontal orientation.
- The anchor movement and rotation results in different soil behaviour around the anchor. Above the anchor, in the area close to the front of the fluke, the soil moves predominantly in alignment with the loading direction. Still above the anchor but in the area close to the back of the fluke, the soil tends to fil the void created. The failure surface that is formed extends all the way to the mudline suggesting a shallow failure mechanism.
- Above the anchor, in the area close to the front of the fluke, there is significant concentration of compressive stresses. Above the anchor, in the area close to the back of the fluke the soil is unloaded. The soil below the anchor is also unloaded and increases its volume.
- A point is reached at which the anchor finds it easier to penetrate deeper in the soil than to further compress the soil above which results in a downwards anchor movement.
- The force displacement curve exhibits non-linear behaviour which can be predicted by using either the Linear Elastic – Logarithmic or the hyperbolic models.
- As the anchor embeds deeper into the soil, it generates more capacity with the peak value estimated at 62.8 MN.

Chapter 6

Results – Static Cyclic Load

6.1 Results from the FE simulations

6.1.1 Typical results

In this chapter, the anchor undergoes load stage II, which is imposing one-way cyclic load. Initially the results of the analysis are presented, specifically when the anchor is positioned at 47% of its ultimate embedment depth ($z_c/z_{c,max}$ = 47%). The anchor has an inclination of 22.9 degrees and its centroid is located 10.8 meters below the mudline. The load angle at the padeye is 27.7 degrees. The results are presented in terms of force displacement curve, evolution of incremental and accumulated displacements, soil behaviour around the anchor and anchor movement.

Figure 6.1 depicts the force displacement curve for when the average load is 40% and the cyclic load amplitude is 10% of the anchor's monotonic capacity, as calculated in Chapter 5. This corresponds to an average load of 13115 kN and a cyclic load amplitude of 3280 kN. For the first loading cycle the response follows the monotonic curve up to the maximum applied load. The first unloading curve shows an almost linear decrease and doesn't follow in reverse the monotonic curve which suggests that plastic deformations have already occurred. In each subsequent cycle, there is an amount of plastic displacement added which reaches just over 72cm after 300 cycles.

The stiffness of each loading and unloading cycle is defined as in **Figure 6.2**. The stiffness of the first loading cycle is the slope between points A and B, the stiffness of the second loading cycle is the slope between points C and D and so on. The stiffness of the first unloading cycle is the slope between points B and C and so on. The normalized stiffness with respect to the loading stiffness of the first cycle is also depicted in **Figure 6.2**. The stiffness during loading increases rapidly for the first 10 cycles, tripling its initial value and continues to increase at a smaller rate thereafter. After 300 cycles the increasing rate has declined significantly with the stiffness

being just over 5 times the initial one. The stiffness during unloading remains relatively unchanged throughout the simulation.

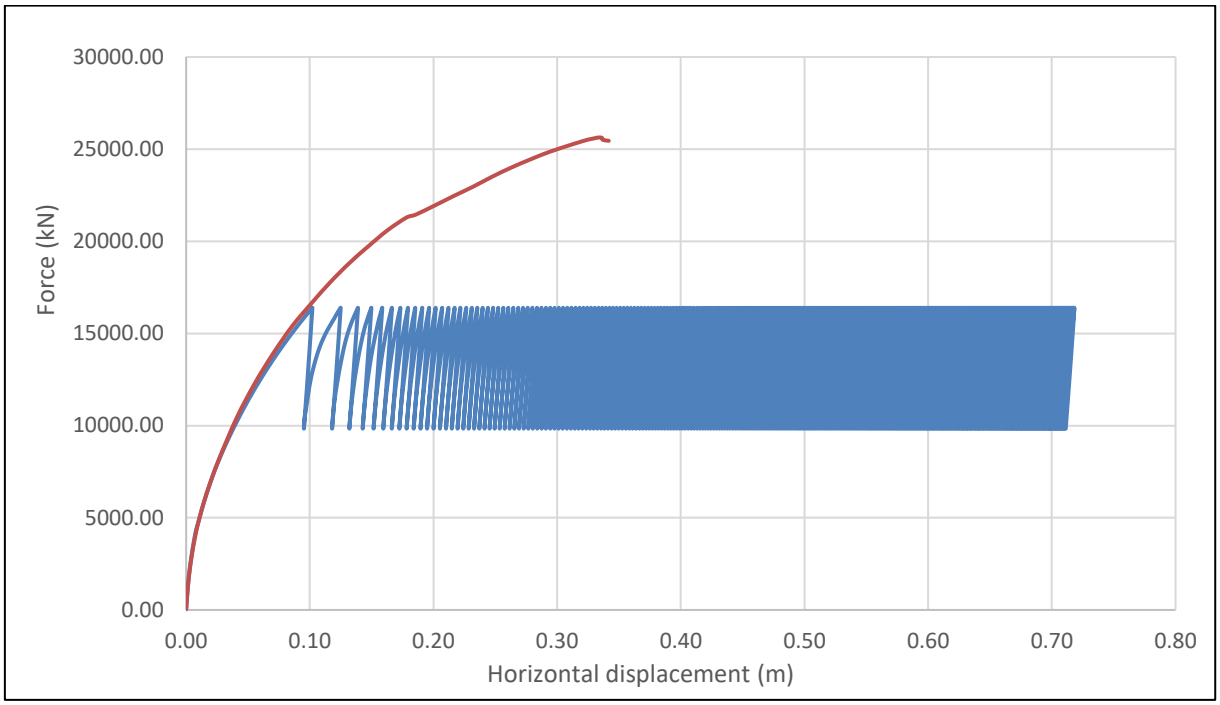

Figure 6.1: Force displacement curve for anchor initial depth $z_c/z_{c,max}$ = 47%, average load 40% and cyclic load 10%.

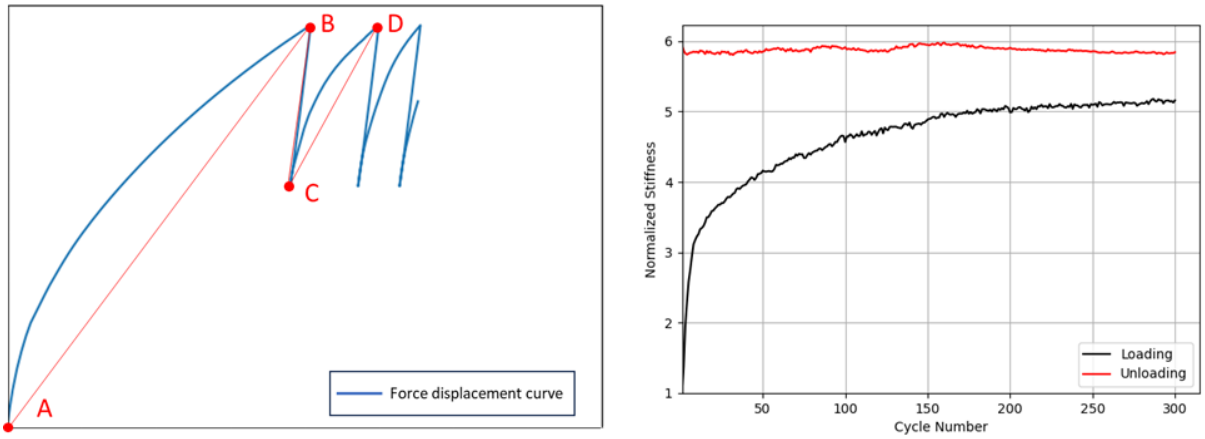

Figure 6.2: Loading and unloading stiffness definition (left) and evolution per cycle (right).

This progressively stiffer behaviour results in the decrease of the amount of incremental displacements per cycle as shown in **Figure 6.3a**. Starting from about 9.5 cm in the first cycle, it takes 5 cycles for the incremental displacement to drop to below 1 cm per cycle. This value slowly decreases and seems to stabilize at approximately 0.1 cm per cycle. This implies that for every additional loading/unloading cycle at this load level, the anchor will move 0.1cm horizontally. Observing **Figure 6.3b** it is evident that the rate at which the displacements

accumulate declines with each additional cycle and appears to be almost linear after 150 loading/unloading cycles.

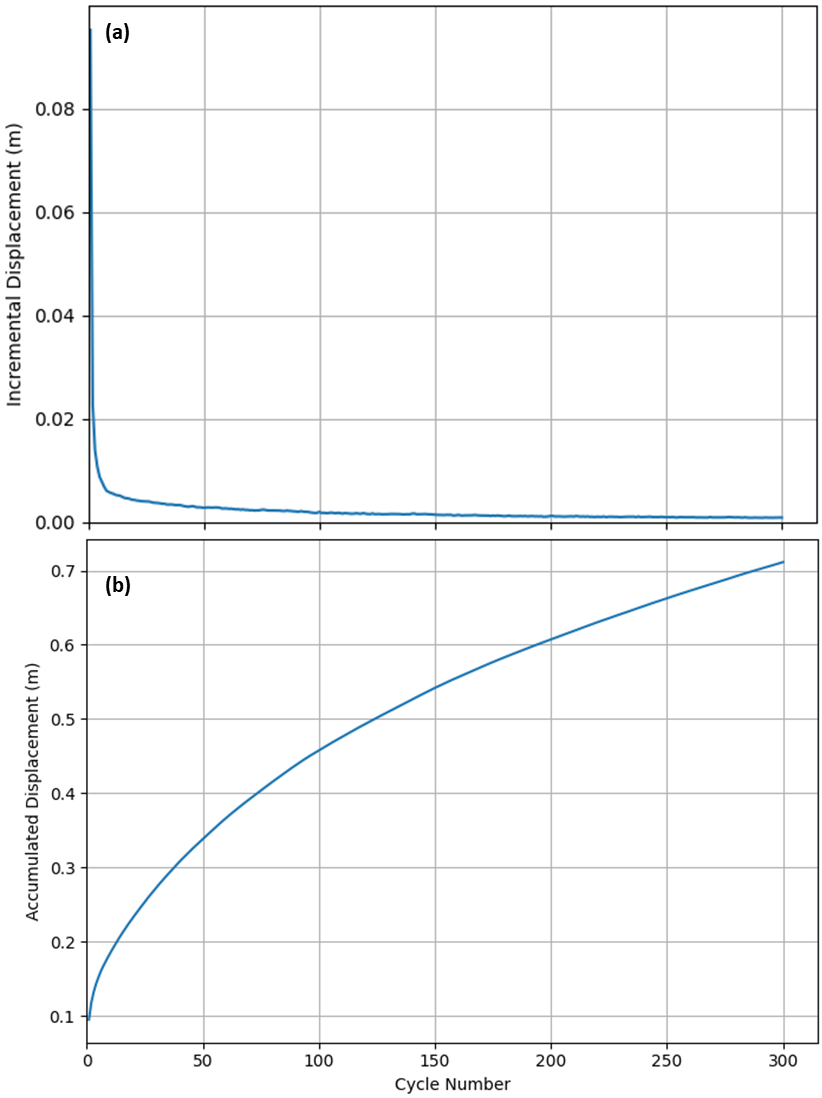

Figure 6.3: Evolution of (a) Incremental and (b) accumulated displacemetns.

Figure 6.4 depicts the total deviatoric strain γ_s and principal effective stress σ_3' contours after 300 cycles of loading. The development of a failure surface extending to the mudline, coupled with reduced compressive stresses behind the anchor and increased compressive stresses ahead of it, as observed in the monotonic loading scenario, holds true for cyclic loading as well. The soil in the vicinity of the anchor appears to be in a state of failure, even though the applied load is far from the anchor's capacity at this depth. The anchor sustains a consistent rotational movement at a rate of 1 degree over a 12cm span. As in the monotonic case, this is attributed to the fact that while the anchor rotates, the load angle at the padeye θ_α must evolve to account for the updated anchor geometry. However, this feature was not possible to implement into the numerical analyses and θ_α remained constant.

This rotation occurs concurrently with horizontal and downward shifts, as depicted in **Figure 6.5** and **Figure 6.6**.

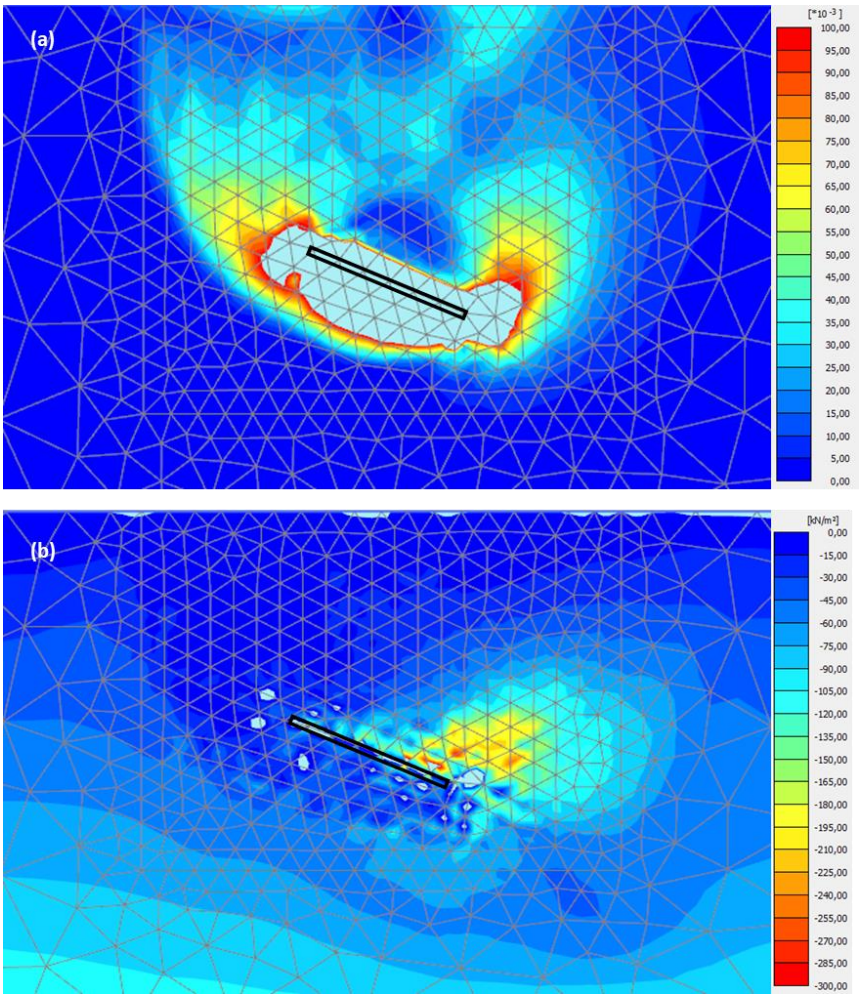

Figure 6.4: Contours of (a) total deviatoric strains γs and (b) principal effective stress σ_3'.

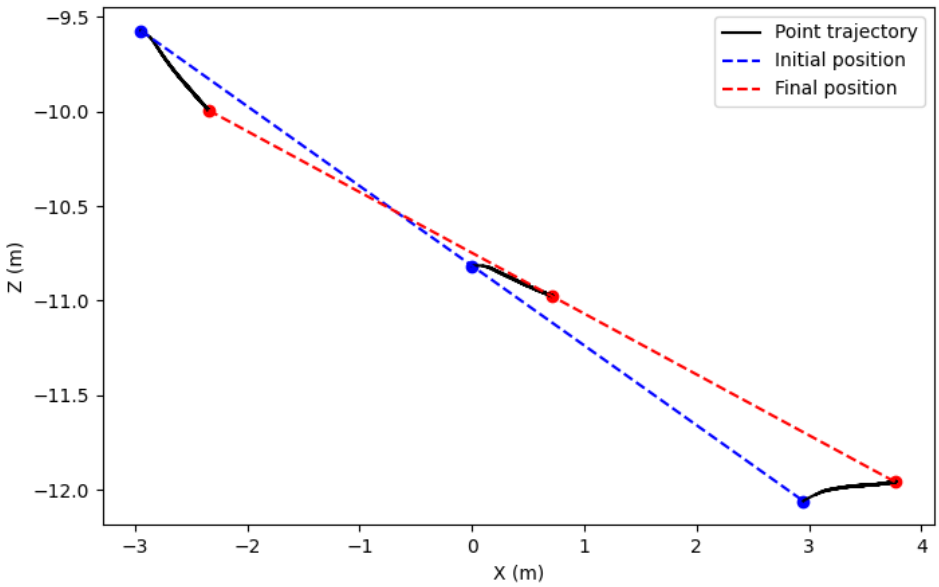

Figure 6.5: Initial and final anchor orientation.

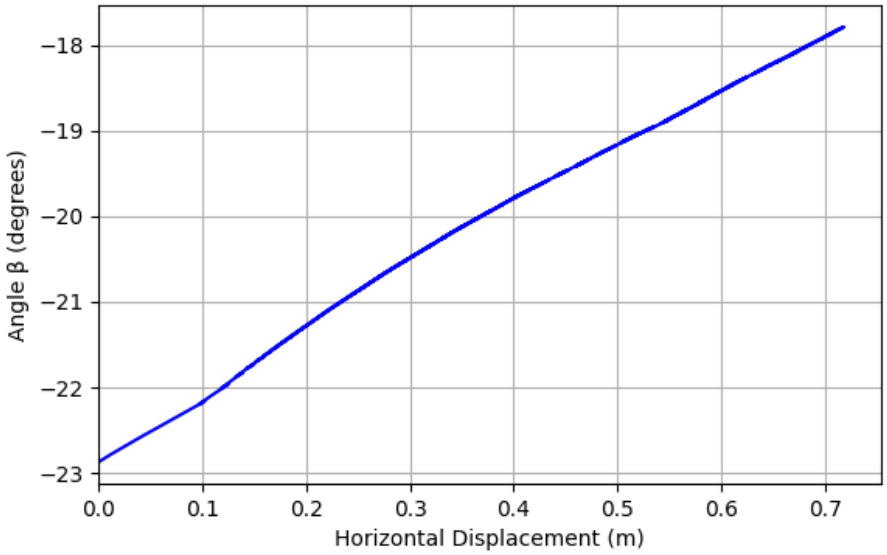

Figure 6.6: Evolution of anchor orientation.

6.1.2 Effect of load range

All results presented in Section 6.1.1 relate to an average load of 40% and a cyclic load of 10% of the anchor's monotonic capacity. In order to investigate the effect of the anchor load value on the anchor's response, the analysis was repeated for different combinations of average and cyclic load, further elaborated in **Table 9**. No average loads above the 50% threshold were examined as this load case corresponds to a value close to the maximum load expected at the anchor (16MN) calculated in Chapter 3.

Table 9: Noramlized load values

Average load 10%	3279 kN
Average load 20%	6558 kN
Average load 30%	9836 kN
Average load 40%	13115 kN
Average load 50%	16394 kN

Figure 6.7 presents the evolution of incremental and accumulated displacements for varying the value of the normalized average load but keeping the normalized cyclic load constant at 10% of the capacity. It can be inferred that when the average load decreases, the incremental displacements stabilize in fewer cycles and at a lower value. When the average load is at 10% of the capacity the incremental displacement reaches 0.15 mm while when the average load is at 50% the respective value is 1.8 mm. Since offshore structures have the potential to be subjected to thousands of cycles throughout their operational lifetime, significant displacements may accumulate and need to be considered during the design phase.

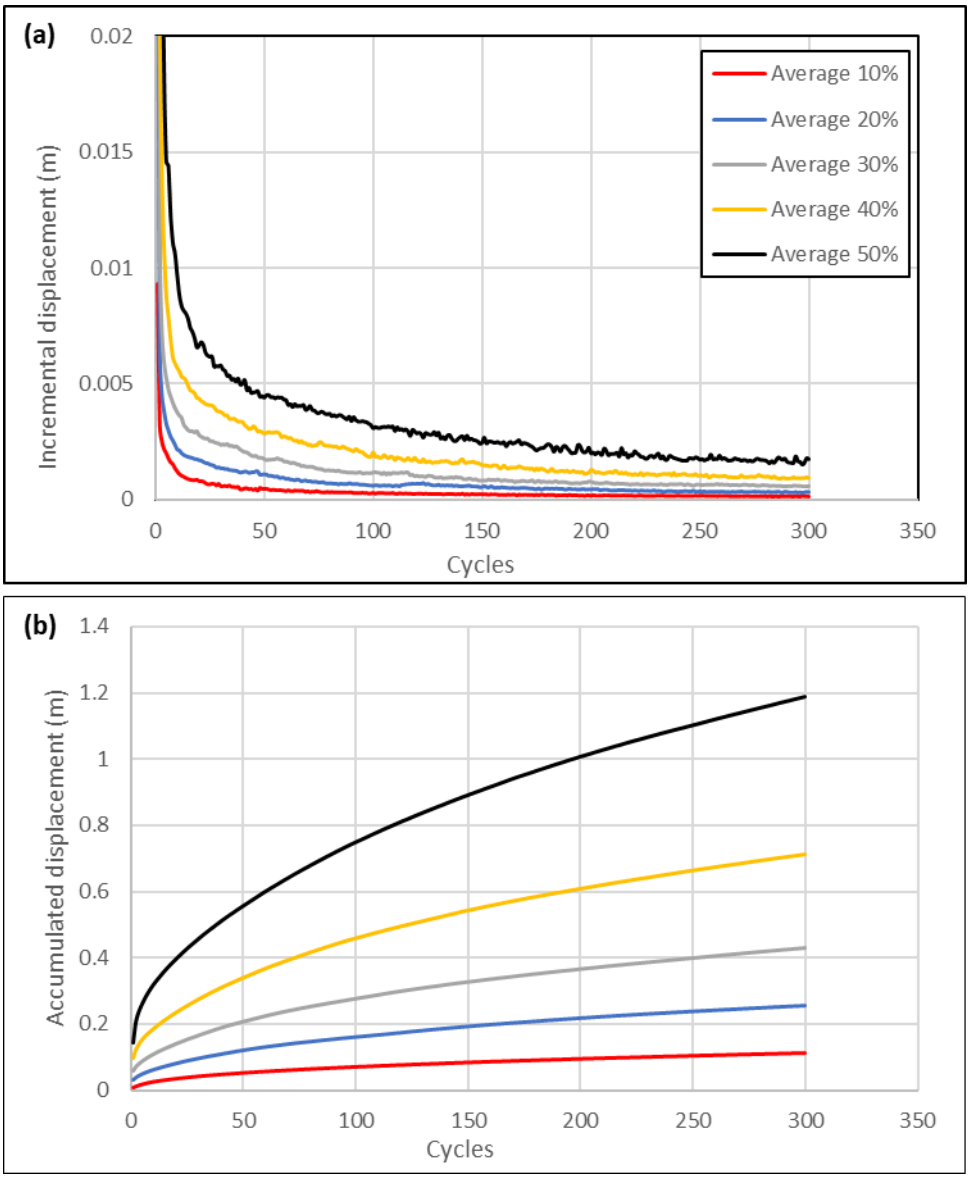

Figure 6.7: Evolution of (a) incremental and (b) accumulated displacements for initial anchor depth $z_c/z_{c,max}$ = 47%, varying average load and cyclic load 10%.

Figure 6.8 presents the evolution of incremental and accumulated displacements for keeping the value of the normalized average load constant at 30% but increasing the normalized cyclic load from 10% to 30% of the capacity. By increasing the cyclic load the is a substantial quantitative difference as the incremental displacements require a greater number of cycles to stabilize and when they eventually do, they settle at a higher value. This is logical as the greater the difference between the maximum and minimum load at each cycle the higher plastic displacements occur. This results in the accumulated displacements being almost triple when the cyclic load is increased three times.

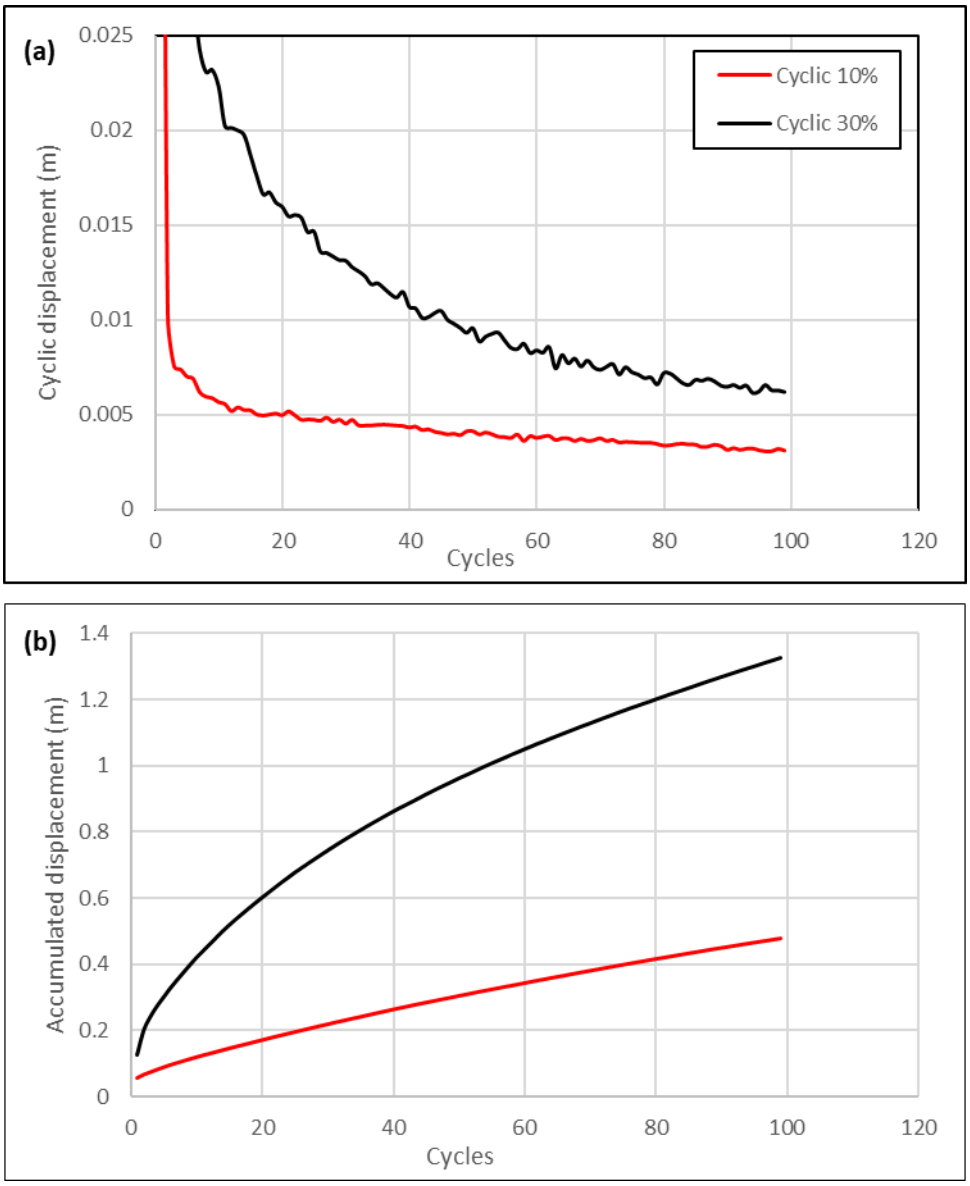

Figure 6.8: Evolution of (a) incremental and (b) accumulated displacements for initial anchor depth zc/zc,max = 47%, average load 30% and varying cyclic load.

Figure 6.9 displays the progression of incremental and accumulated displacements with different combinations of average and cyclic loads, culminating in a maximum load amounting to 60% of the anchor's capacity. Notably, after 100 cycles, the incremental displacements are more pronounced in the case with increased cyclic load amplitude. This observation suggests that while the maximum load value holds importance, it is not the predominant factor governing accumulated displacements; rather, it is the amplitude of the cyclic load that plays a more significant role.

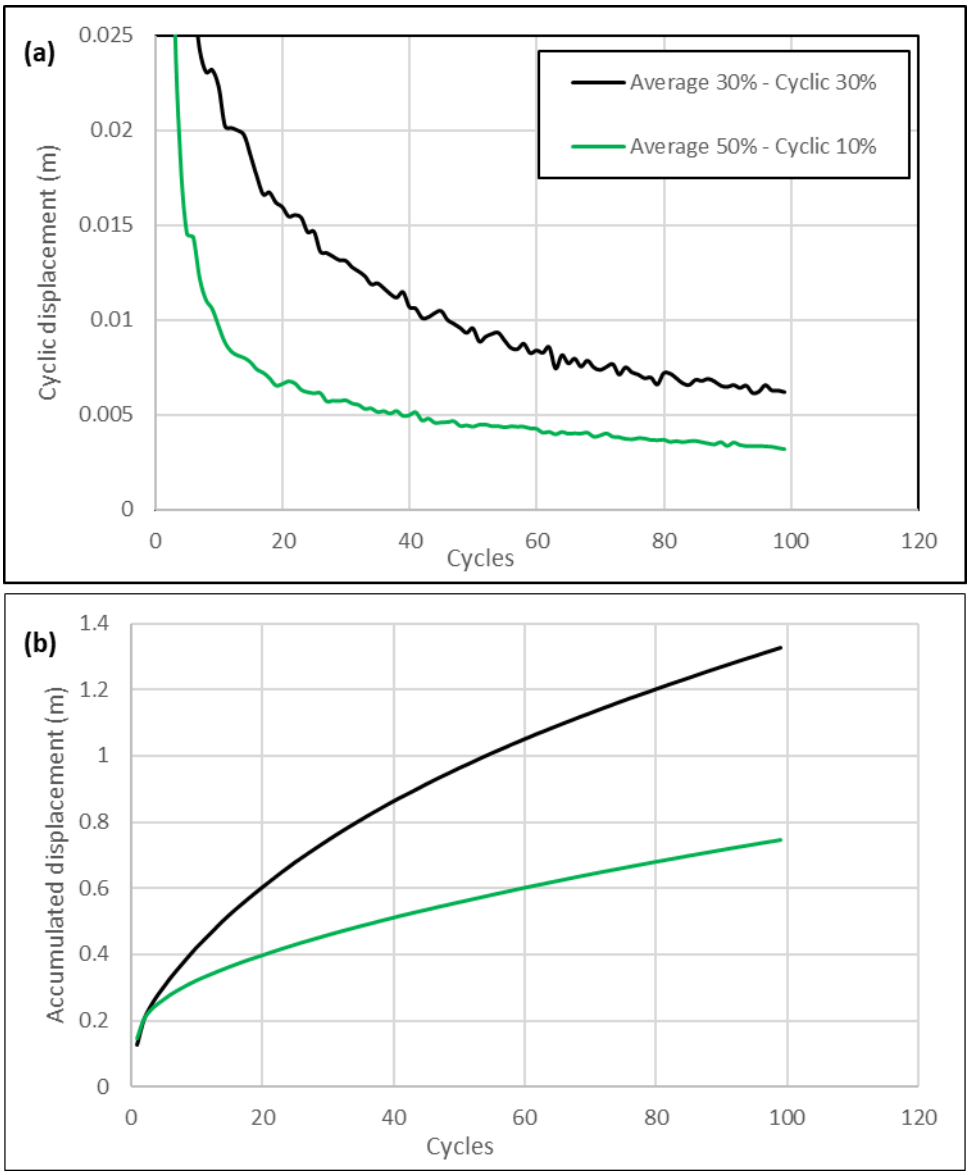

Figure 6.9: Evolution of (a) incremental and (b) accumulated displacements for initial anchor depth zc/zc,max = 47%, max load 60%.

6.1.3 Multi-Amplitude Loading

While this Chapter of the Thesis focuses on cyclic loads of constant amplitude, real environmental loads are characterized by varying amplitude, average level and frequency. In offshore engineering practices, these irregular loadings are often simplified by techniques that convert the original complex loading history into a series of distinct loading cycles, each with its own amplitude and number of repetitions sorted in ascending amplitude. For cases where pore pressure build up is disregarded, this is proven to be a reasonable approach (Liu et al. 2022b). In this Section, an investigation is conducted to examine whether the sequence in which the equivalent regular cycle packages are applied has any impact on the accumulation of displacements.

A summary of the considered loading cases with regular cyclic packages is provided in **Table 10**. Load history effects are investigated by simulating different application patterns of the selected load packages. These patterns include increasing, mixed, and decreasing amplitudes. To manage the computational demands inherent in 3D finite element simulations, the analysis exclusively focuses on individual packages consisting of 30 cycles each. While this value is small compared to the thousands of loading cycles experienced by DEAs offshore, it is still possible to infer valuable insights on soil anchor interaction under multi amplitude cyclic loading.

Table 10: Regular multi-amplitude cyclic loading cases.

Order	Average Load (kN)	Cyclic Load Amplitude (kN)
Increasing	4920	1640 → 3280 → 4920
Mixed	4920	3280 → 1640 → 4920
Decreasing	4920	4920 → 3280 → 1640

The force displacement curves of the anchor centroid for all cases are presented in **Figure 6.10** and the evolution of the anchor's centroid displacement against the number of cycles is shown in **Figure 6.11**. It is evident that the accumulated displacements evolve at a significant rate when the current load amplitude is the highest experienced until that moment. Case (a) shows that increasing the cyclic load amplitude of subsequent loading packages induces accumulation of displacements at a progressively higher rate. On the contrary, negligible displacements are observed for the second and third loading package of case (c) as the amplitude of the first package is higher. The intermediate case (b) shows consistent results as negligible displacements occur of the second package where the cyclic amplitude is decreased but considerable displacements are accumulated during the third package where the amplitude is the highest experienced.

Another point worth mentioning is that the accumulated displacement after 90 cycles is approximately 13cm for all three cases which suggests that the ordering of loading parcels has minor effects on the accumulated displacement of the anchor's centroid. Similar results have been reported in the literature for piles and anchors under cyclic loading (Singh and Ramaswamy 2008, Liu et al. 2022b). What can be concluded is that each loading cycle with a certain amplitude damages the microstructure of the soil independently and the cumulative damage can be estimated by summing the damage of each individual cycle.

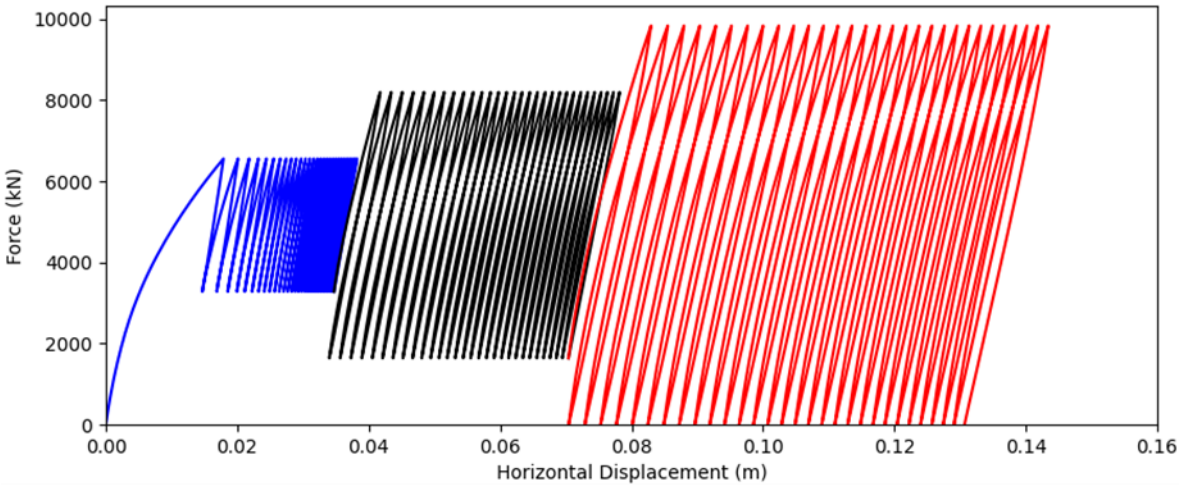

(a) F_{cyc} = 1640 kN → 3280 kN → 4920 kN

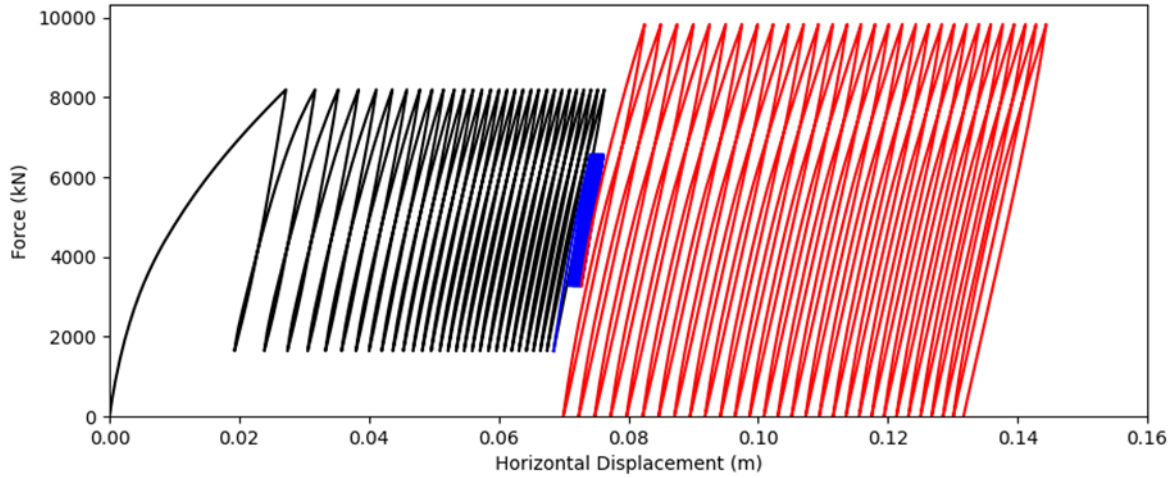

(b) F_{cyc} = 3280 kN → 1640 kN → 4920 kN

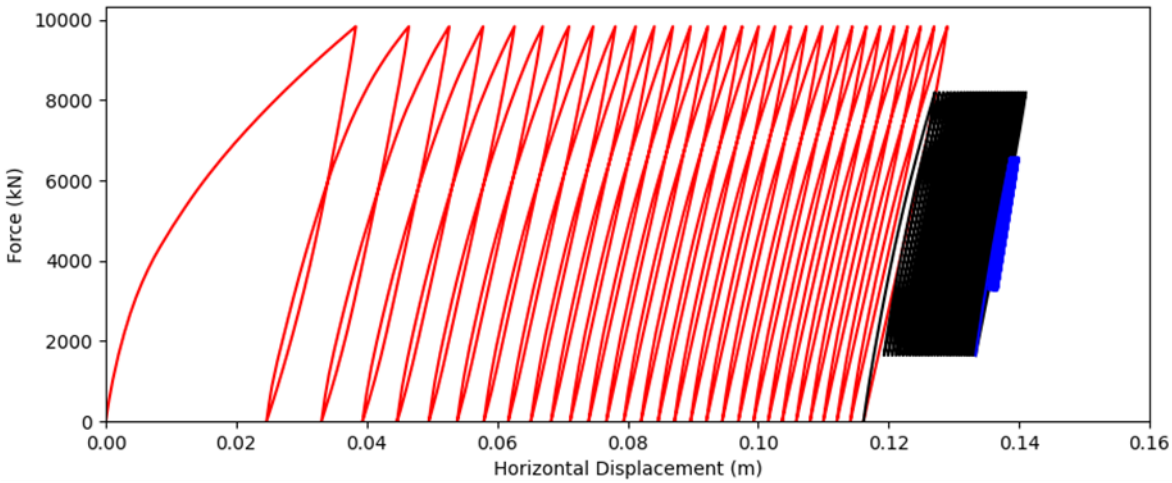

(c) F_{cyc} = 4920 kN → 3280 kN → 1640 kN

Figure 6.10: Influence of the cyclic loading sequence on the evolution of anchor displacement - Force–Displacement response at the centroid.

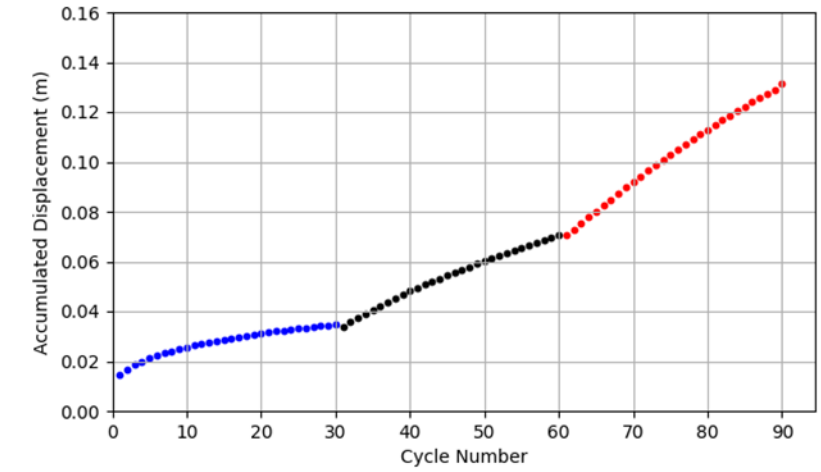

(a) F_{cyc} = 1640 kN → 3280 kN → 4920 kN

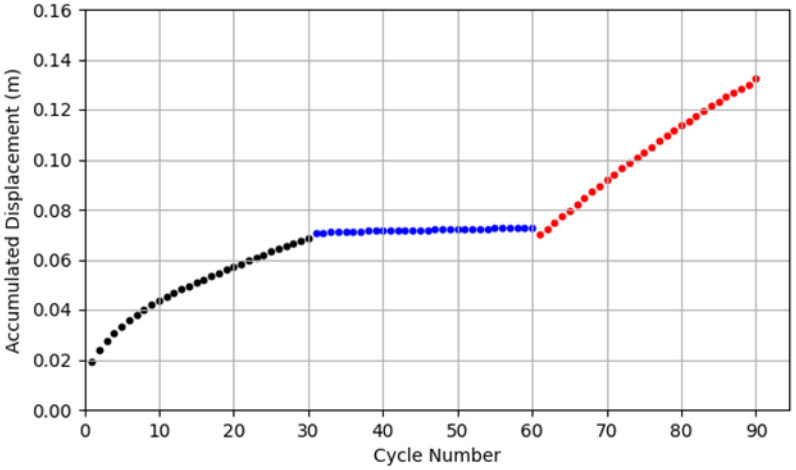

(b) F_{cyc} = 3280 kN → 1640 kN → 4920 kN

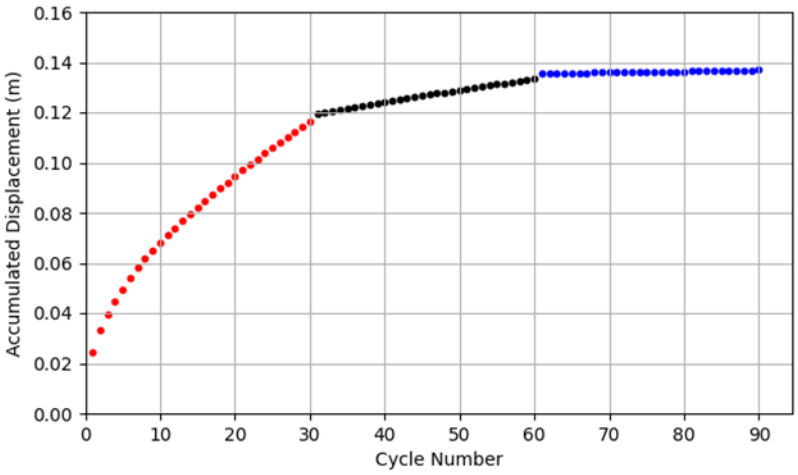

(c) F_{cyc} = 4920 kN → 3280 kN → 1640 kN

Figure 6.11: Influence of the cyclic loading sequence on the evolution of anchor displacement. Centroid displacement against the number of loading cycles

6.2 Calibration of 1D model

It is apparent that three-dimensional finite element simulations offer the most accurate estimate of soil structure interaction in non-linear soil behaviour. However, creating a reliable FE model, selecting an appropriate stress-strain law and calibrating its parameters is inherently a complex and time consuming task. Recently, the focus of researchers has been in developing simplified one-dimensional soil-structure interaction models, mainly for piles. Particularly interesting for this Thesis is the work of Kementzetzidis et al. 2022 who introduced a model to analyze piles in sandy soils subjected to lateral cyclic loading.

The model builds on the work of Suryasentana and Lehane 2014 who proposed a monotonic p-y relationship for piles embedded in sandy soils. Moreover, they proposed a CPT-based parameter calibration procedure (Suryasentana and Lehane 2016) for the parameters p_u, α and m which they introduced. In their formulation, p_u stands for the ultimate soil reaction (per unit length), while α and m are positive dimensionless parameters. One of the spring elements Kementzetzidis et al. 2022 incorporated into the p-y formulation is memory enhancement, which captures soil ratcheting that emerges when the pile is subjected to extended cyclic loading. For this Thesis, only the memory spring is utilized from the Kementzetzidis et al. 2022 model. This neccesitates the calibration of only four parameters, namely:

p_u : the ultimate soil resistance per unit length (kN/m)

α : post yielding stiffness parameter (-)

m : shape parameter (-)

μ_0 : racheting parameter (-)

In addition to the above parameters, the stiffness E (kN/m) of an elastic spring that is connected in series with the memory sping needs to be calibrated. The equations employed in the aforementioned model are included in the Appendix. Since response under examination refers to solely one point, the anchor centroid, and not a collection of points moving in one direction (as is the case for piles), the term 0D is adopted hereafter to describe the elastic spring in series with the memory spring. The calibration of parameters pu, α, m and E was performed for the monotonic case when the anchor is positioned at 47% of its ultimate embedment depth ($z_c/z_{c,max}$ = 47%) and the comparison with the FE prediction is depicted in **Figure 6.12** which exhibits a good match.

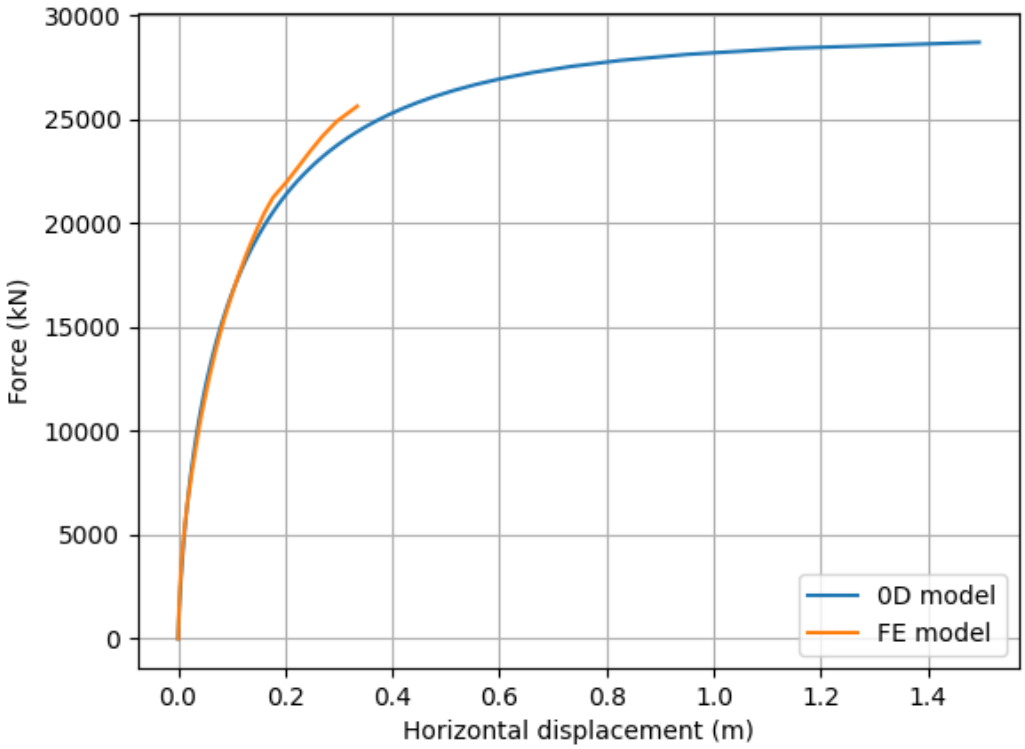

Figure 6.12: Monotonic curve comparisonbetween FEM and 0D model.

The ratcheting control parameter was calibrated against the results for the case where the average load is 40% and the cyclic load is 10% of the anchor's monotonic capacity. The best fit values are presented in **Table 11** and the results in terms of incremental and accumulated displacements are depicted in **Figure 6.13**. Considering the high accuracy with which the response is predicted, the 3D FE analysis can be avoided and the 0D model with proper parameters can be employed instead.

Table 11: Best parameters for anchor initial depth $z_c/z_{c,max}$ = 47%, average load 40% and cyclic load 10%.

E , (kN/m)	$1x10^6$
α , (-)	11
m , (-)	0.59
p_u , (kN)	29000
μ_0 , (-)	59

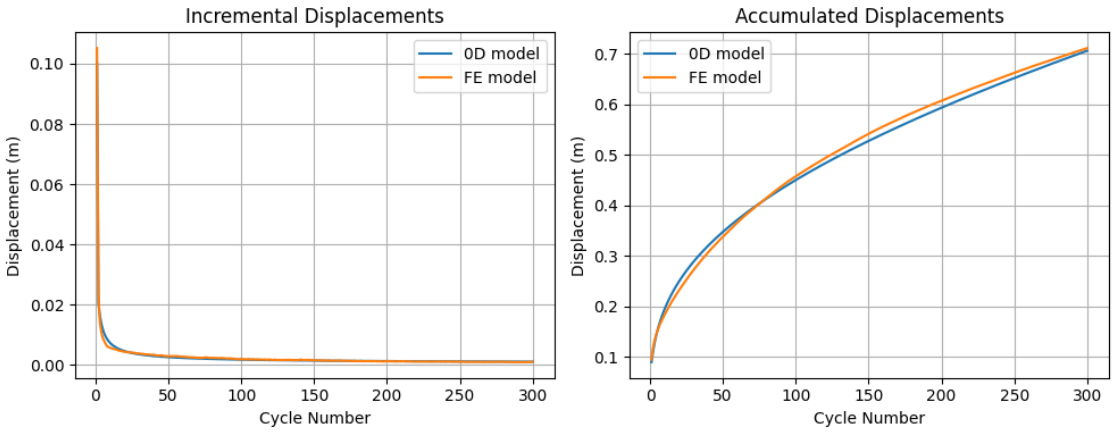

Figure 6.13: Best fit comparison for anchor initial depth zc/zc,max = 47%, average load 40% and cyclic load 10%.

However, the parameters of **Table 11** can't be used regardless of the applied load as the displacements are underpredicted for lower average load (e.g. 30%) and overpredicted for higher average load (e.g. 50%) as depicted in **Figure 6.14**. Indicatively, **Figure 6.15** illustrates the predictions with the appropriate values for μ_0 for three cases and the predictions match reasonably well. The calibrated values for the ratcheting control parameter are presented in **Table 12**. The current mode formulation could be improved e.g. so that μ_0 is related to the permanent displacement and provides accurate results across a wide range of loads.

Table 12: Calibrated values for the ratcheting control parameter μ_0.

Average Load (%)	Cyclic Load Amplitude (%)	Parameter μ_0
10	10	38
20	10	40
30	10	48
40	10	59
50	10	92
30	30	75

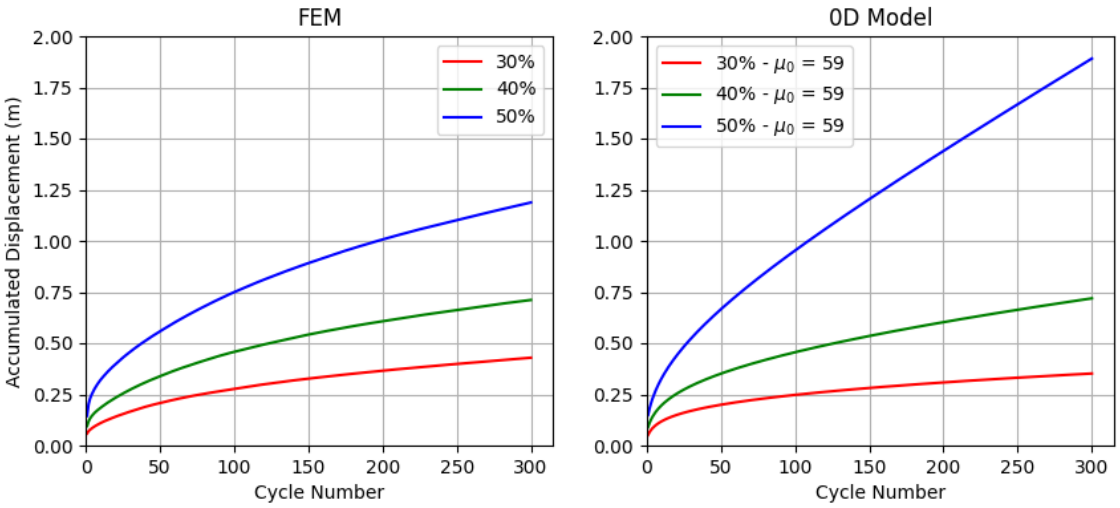

Figure 6.14: Predictions comparison for anchor initial depth zc/zc,max = 47%, cyclic load 10% and average load 30%, 40% and 50%. Parameters from Table 2.

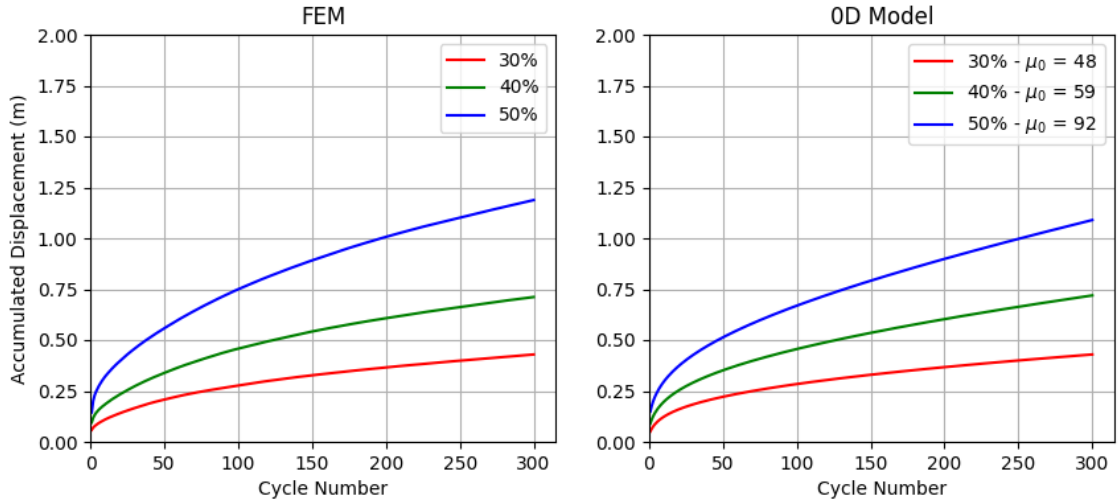

Figure 6.15: Predictions comparison for anchor initial depth $z_c/z_{c,max}$ = 47%, cyclic load 10% and average load 30%, 40% and 50%. Parameters from Table 2 except from μ_0.

6.3 Parametric study

In this section the effect of applying the cyclic load when the anchor is at different positions along its trajectory is examined. The average load applied is 13115 kN and the cyclic load amplitude is 3280 kN which corresponds to the 40% ± 10% case of the anchor positioned at 47% of its ultimate embedment depth ($z_c/z_{c,max}$ = 47%). The four additional positions examined have normalized embedment depths 60%, 70%, 80% and 90%. **Figure 6.16** depicts the results from the FE analyses in terms of accumulated displacements after 150 loading/unloading cycles. When the anchor is embedded deeper, the applied load is farther from the UHC and thus, less plastic deformations occur. This results in the accumulated displacements after 150 cycles being smaller the deeper the anchor is placed. The 0D model predictions are in reasonable agreement with the FE results.

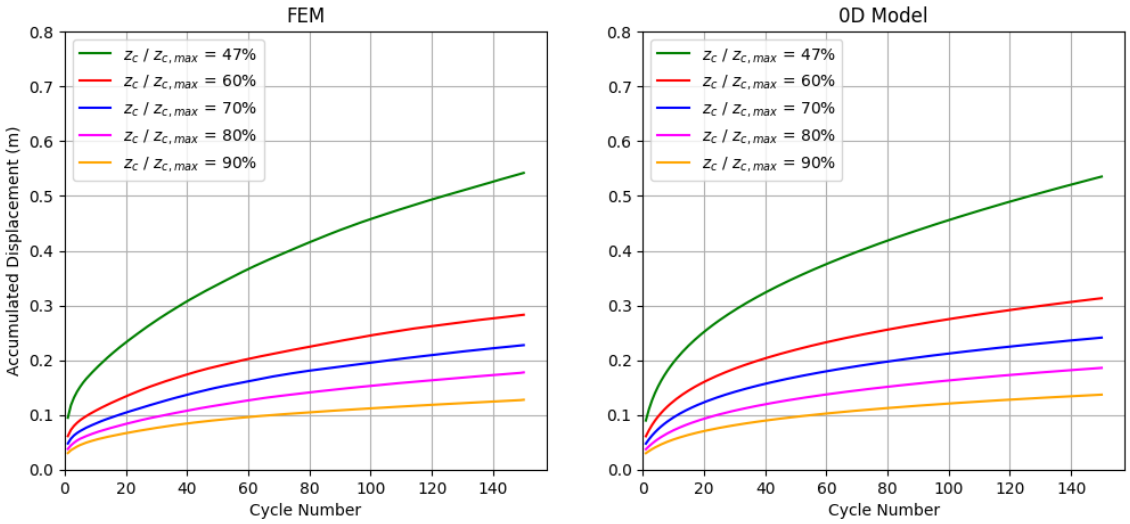

Figure 6.16: Accumulation of displacements obtained from FE analyses and 0D model predictions for diferrent initial anchor positions.

As illustrated in **Figure 6.17**, the initial anchor position affects the model parameters. The elastic stiffness E and the ultimate permissible load p_u show an increase with the increase of the anchor depth. This is not surprising as, according to Chapter 5, the response becomes stiffer and the anchor capacity increases with increasing depth, therefore the parameters need to be adjusted accordingly. The parameter α decreases with increasing anchor depth while the shape parameter m slightly decreases. It can be also observed that while the parameter m exhibits a linear relation with depth, the others follow a trend that seems to reach a plateau as the anchor is closer to the ultimate depth. The calibrated parameters for all examined locations are summarized in **Table 13**.

Table 13: Calibrated 0D model parameters for different anchor initial positions.

Parameter	$z_c/z_{c,max}$ = 47%	$z_c/z_{c,max}$ = 60%	$z_c/z_{c,max}$ = 70%	$z_c/z_{c,max}$ = 80%	$z_c/z_{c,max}$ = 90%
E (kN/m)	$1x10^6$	$1.4x10^6$	$1.8x10^6$	$1.85x10^6$	$1.9x10^6$
p_u (MN)	29.0	41.2	48.5	52.9	55.9
α (-)	11	6.6	5.8	5.4	5.15
m (-)	0.59	0.54	0.53	0.51	0.49
μ_0 (-)	59	60	62	64	75

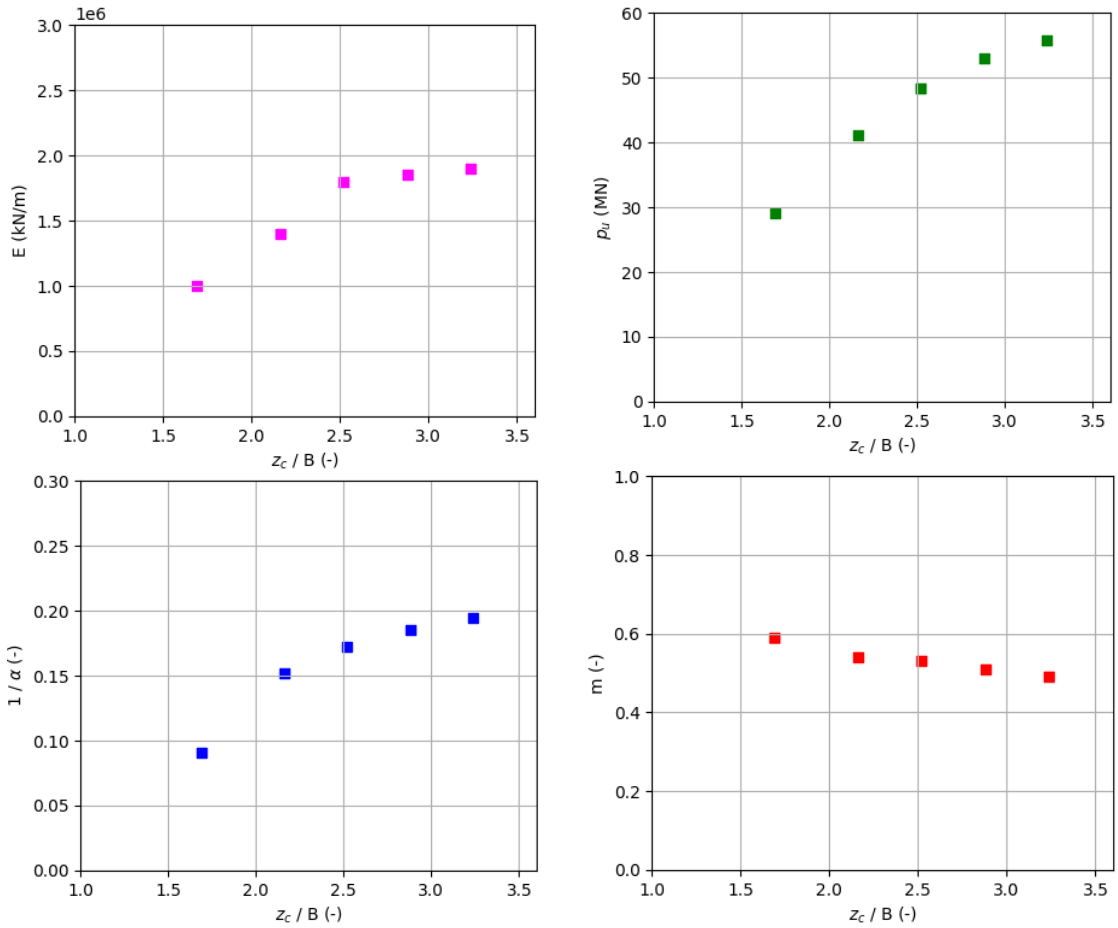

Figure 6.17: Influence of initial anchor depth on 0D model parameters.

6.4 Chapter Summary

In this chapter, the anchor is subjected to one-way cyclic load. The main conclusions of this study can be summarized as follows:

- In the first loading cycle the anchor follows the response from the monotonic case.
- With each additional cycle more plastic displacements are accumulated.
- The anchor shows a progressively stiffer response which decreases the amount of incremental displacements per cycle and stabilizes after enough cycles have been endured by the anchor.
- The movement of the anchor closely resembles the monotonic pattern, characterized by horizontal translation combined with a simultaneous rotation towards a more horizontal orientation.
- Increasing the value of average load while keeping the cyclic load constant results in the incremental displacements stabilizing after a higher number of cycles and at a higher value.

- Increasing the value of cyclic load while keeping the average load constant has qualitatively the same effect with increasing the average load. However, quantitatively, the effect is more pronounced when increasing the cyclic load.
- In the case of multi-amplitude loading, the accumulated displacements evolve at a significant rate when the current load amplitude is the highest experienced until that moment. The ordering of loading parcels has minor effects on the accumulated displacement of the anchor's centroid.
- The 1D model proposed by Kementzetzidis et al. 2022 for piles under lateral cyclic loading can be calibrated to reproduce the response of a DEA under monotonic load.
- The model predictions when applying cyclic loading are accurate from a qualitative point of view. However, depending on the applied load can lead to overestimation or underestimation of the accumulated displacements.
- To better reproduce the DEA response, the ratcheting parameter μ_0 when the load amplitude is increased.
- When placing the anchor deeper in the soil, the parameters E and p_u must be increased and parameter α must be decreased to capture the response. Parameter m should be slightly decreased.

Chapter 7

Conclusions - Recommendations

7.1 Conclusions

The scope of the Thesis was to select an anchor based on a case study and investigate the behaviour of this anchor under cyclic loading. The VolturnUS-S (Allen et al. 2020) semisubmersible was studied, connected to Drag Embedded Anchors via a catenary mooring system. The location for the floater was an area 15 km of the coast of Aberdeen, Scottland for which the environmental conditions were obtained. Subsequently, the loads from wind and waves on the floater were estimated and finally transferred to the anchor through the mooring lines. With applying the appropriate safety factors, it was concluded that the 65t Stevpris Mk5 Vryhof anchor (VRYHOF 2018) is appropriate for this study. Analytical methodologies published in the literature were utilized to predict the anchor depth, orientation and load angle at the padeye during installation. Finally, the anchor was placed in different positions along its trajectory and was subjected to static monotonic and static cyclic load. The main conclusions can be summarized as below:

I. Anchor's Response to Static Monotonic Load

- As the anchor load increases, the anchor will experience horizontal movement with a slight upward movement and gradual rotation towards a more horizontal orientation.
- The anchor movement and rotation results in different soil behaviour around the anchor. Above the anchor, in the area close to the front of the fluke, the soil moves predominantly in alignment with the loading direction. Still above the anchor but in the area close to the back of the fluke, the soil tends to fil the void created. The failure surface that is formed extends all the way to the mudline suggesting a shallow failure mechanism.
- Above the anchor, in the area close to the front of the fluke, there is significant concentration of compressive stresses. Above the anchor, in the area close to the back

of the fluke the soil is unloaded. The soil below the anchor is also unloaded and increases its volume.

- A point is reached at which the anchor finds it easier to penetrate deeper in the soil than to further compress the soil above which results in a downwards anchor movement.
- The force displacement curve exhibits non-linear behaviour which can be predicted by using either the Linear Elastic – Logarithmic or the hyperbolic models.
- As the anchor embeds deeper into the soil, it generates more capacity with the peak value estimated at 62.8 MN.

II. Anchor's Response to Static Cyclic Load

- In the first loading cycle the anchor follows the response from the monotonic case.
- With each additional cycle more plastic displacements are accumulated.
- The anchor shows a progressively stiffer response which decreases the amount of incremental displacements per cycle and stabilizes after enough cycles have been endured by the anchor.
- The movement of the anchor closely resembles the monotonic pattern, characterized by horizontal translation combined with a simultaneous rotation towards a more horizontal orientation.
- Increasing the value of average load while keeping the cyclic load constant results in the incremental displacements stabilizing after a higher number of cycles and at a higher value.
- Increasing the value of cyclic load while keeping the average load constant has qualitatively the same effect with increasing the average load. However, quantitatively, the effect is more pronounced when increasing the cyclic load.
- In the case of multi-amplitude loading, the accumulated displacements evolve at a significant rate when the current load amplitude is the highest experienced until that moment. The ordering of loading parcels has minor effects on the accumulated displacement of the anchor's centroid.
- The 1D model proposed by Kementzetzidis et al. 2022 for piles under lateral cyclic loading can be calibrated to reproduce the response of a DEA under monotonic load.
- The model predictions when applying cyclic loading are accurate from a qualitative point of view. However, depending on the applied load can lead to overestimation or underestimation of the accumulated displacements.

- To better reproduce the DEA response, the ratcheting parameter μ_0 should be increased when the load amplitude is higher.
- When placing the anchor deeper in the soil, the parameters E and p_u must be increased and parameter α must be decreased to capture the response. Parameter m should be slightly decreased.

7.2 Recommendations

While completing this Thesis, very interesting research topics arose which require further investigation:

1. Simulating anchors of smaller size than the 65t Vryhof Stevpris Mk5 that was thoroughly examined in this Thesis. This could potentially lead to identifying patterns for the parameters of the Kementzetzidis et al. 2022 model and thus eliminate the need for performing 3D Finite Element analyses during the design phase.
2. The anchor was assumed to be wished in place in this Thesis, however, it is recommended to explore how incorporating anchor installation effects might impact the results. This would necessitate conducting large deformation Finite Element analyses, which can be computationally demanding and are beyond the scope of this Thesis.
3. The findings from the cyclic load analyses suggest that the soil can be significantly disturbed under cyclic loads, even when these loads are well below the anchor's capacity. As a result, it is advisable to conduct monotonic load analyses following the cyclic load analyses to assess the anchor's post-cyclic capacity.
4. Extending the parametric study to different soil properties (e.g. sands with different relative density, cohesive soils or the presence of layers with different properties), examining the response of the anchor under undrained loading conditions, applying irregular cyclic load or applying the load in a direction that is not parallel to the anchor’s shank.
5. Examining different anchor types than Drag Embedded Anchors (DEA) for the foundation of the floater such as Suction Embedded Plate Anchors (SEPLA) or Dynamically Embedded Plate Anchors (DEPLA).

References

Allen, C., Viscelli, A., Dagher, H., Goupee, A., Gaertner, E., Abbas, N., Hall, M., and Barter, G. (2020). "Definition of the UMaine VolturnUS-S Reference Platform Developed for the IEA Wind 15-Megawatt Offshore Reference Wind Turbine." Golden, CO (United States).

Barter, G. E., Robertson, A., and Musial, W. (2020). "A systems engineering vision for floating offshore wind cost optimization." *Renewable Energy Focus*, Elsevier Ltd, 34, 1–16.

Been, K., and Jefferies, M. G. (1985). "A state parameter for sands." *Geotechnique*, 35(2), 99–112.

Bransby, M. F., and O'Neill, M. P. (1999). "Drag anchor fluke-soil interaction in clays." *Numerical models in geomechanics. Proceedings of the 7th international symposium, Graz, September 1999.*, CRC Press, 489–494.

Bureau of Shipping, A. (2020). "Guide for Building and Classing Floating Offshore Wind Turbines 2020."

Cerfontaine, B., Knappett, J., Brown, M. J., Davidson, C., and Sharif, Y. (2020). "Optimised design of screw anchors in tension in sand for renewable energy applications." *Ocean Engineering*, Pergamon, 217, 108010.

Cerfontaine, B., White, D., Kwa, K., Gourvenec, S., Knappett, J., and Brown, M. (2023). "Anchor geotechnics for floating offshore wind: Current technologies and future innovations." *Ocean Engineering*, Pergamon, 279, 114327.

Chao, H. B., and Eng, H. (2016). "PERFORMANCE OF PLATE ANCHORS UNDER SUSTAINED LOADING."

Copernicus. (2023). "Home | Copernicus." <https://climate.copernicus.eu/> (Aug. 28, 2023).

Corti, R., Diambra, A., Wood, D. M., Escribano, D. E., and Nash, D. F. T. (2016). "Memory Surface Hardening Model for Granular Soils under Repeated Loading Conditions." *Journal of Engineering Mechanics*, American Society of Civil Engineers (ASCE), 142(12).

Dafalias, Y. F., and Manzari, M. T. (2004). "Simple Plasticity Sand Model Accounting for Fabric Change Effects." *Journal of Engineering Mechanics*, American Society of Civil Engineers, 130(6), 622–634.

Day, R. (2006). "Foundation Engineering Handbook."

Degenkamp, B. G., and Dutta, A. (1990). "S o i l resistances to embedded a n c h o r in s o f t c l

a y.” 115(10), 1420–1438.

DNV-RP-C205. (n.d.). “DNV-RP-C205 Environmental conditions and environmental loads - DNV.” <https://www.dnv.com/oilgas/download/dnv-rp-c205-environmental-conditions-and-environmental-loads.html> (Aug. 28, 2023).

DNV AS. (2021). “Energy Transition Outlook 2021 Executive Summary. A global and regional forecast to 2050.” 40.

Du, A. (2019). “Floating Wind. Semi-Submersible, Spar, TLP - Empire engineering.” <https://www.empireengineering.co.uk/semi-submersible-spar-and-tlp-floating-wind-foundations/> (Aug. 27, 2023).

Elkhatib, S. (2006). “The Behaviour of Drag-in Plate Anchors in Soft Cohesive Soils.” <https://books.google.nl/books/about/The_Behaviour_of_Drag_in_Plate_Anchors_i.html?id=f_kGNAAACAAJ&redir_esc=y> (Aug. 28, 2023).

Europe, W. (2019). “Offshore wind in Europe.” *Refocus*, 3(2), 14–17.

Geo.jawaga.nl. (n.d.). “geo.javawa.nl.” <https://geo.javawa.nl/> (Aug. 28, 2023).

Han, C., and Liu, J. (2020). “A review on the entire installation process of dynamically installed anchors.” *Ocean Engineering*, Pergamon, 202, 107173.

Hartvig, M. (2019). *Design Load Basis for Offshore Wind turbines DTU Wind Energy Report No . E- Design Load Basis for Offshore Wind turbines DTU Wind Energy Report No . E-0133*.

Herzig, G. (2022). “Global Offshore Wind Report 2021.” *Global Wind Energy Council*, (February), 1–8.

Iec. (2019). “INTERNATIONAL STANDARD Wind energy generation systems-Part 3-1: Design requirements for fixed offshore wind turbines INTERNATIONAL ELECTROTECHNICAL COMMISSION.”

IRENA, I. R. E. A. (2022). “Wind energy.” <https://www.irena.org/Energy-Transition/Technology/Wind-energy> (Aug. 28, 2023).

James, R., and Ros, M. C. (2015). “Floating Offshore Wind: Market and Technology Review Important notice and disclaimer.” (June), 1–168.

Kang, D., Ko, K., and Huh, J. (2015). “Determination of extreme wind values using the Gumbel distribution.”

Kementzetzidis, E., Pisanò, F., and Metrikine, A. V. (2022). “A memory-enhanced p-y model for

piles in sand accounting for cyclic ratcheting and gapping effects A R T I C L E I N F O.” *Computers and Geotechnics*, 148, 104810.

de Koning, C. (1984). *Offshore installation. HANDBOOK OF OFFSHORE ENGINEERING*, Elsevier Ltd.

Kulhawy, F. H. (1983). “EL-2870 Transmission Line Structure Foundations - Shallow Foundations (Kulhawy).pdf.”

Lee, M., Bae, K. T., Lee, I. W., and Yoo, M. (2019). “Cyclic p-y curves of monopiles in dense dry sand using centrifuge model tests.” *Applied Sciences (Switzerland)*, 9(8).

Liu, H., Kementzetzidis, E., Abell, J. A., and Pisanò, F. (2022a). “From cyclic sand ratcheting to tilt accumulation of offshore monopiles: 3D FE modelling using SANISAND-MS.” *Geotechnique*, ICE Publishing, 72(9), 753–768.

Liu, H., Pisanò, F., Petter Jostad, H., and Sivasithamparam, N. (2022b). “Impact of cyclic strain accumulation on the tilting behaviour of monopiles in sand: An assessment of the Miner’s rule based on SANISAND-MS 3D FE modelling.”

Liu, H. Y., Abell, J. A., Diambra, A., and Pisanò, F. (2019). “Modelling the cyclic ratcheting of sands through memory-enhanced bounding surface plasticity.” *https://doi.org/10.1680/jgeot.17.P.307*, Thomas Telford Ltd , 69(9), 783–800.

Loukidis, D., Loukidis, D., and Vavourakis, V. (2014). “Limit lateral resistance of vertical piles in plane strain.”

Ma, K.-T., Luo, Y., Kwna, T., and Wu, Y. (2019). “Mooring System Engineering for Offshore Structures.” <https://books.google.co.id/books?hl=en&lr=&id=Bx2bDwAAQBAJ&oi=fnd&pg=PP1&dq=Mooring+System+Engineering+for+Offshore+Structure.+Cambridge&ots=mo6lnELj81&sig=23etVa9lw91gtUDeVQAIl54Q3Og&redir_esc=y#v=onepage&q=Mooring System Engineering for Offshore Structu> (Aug. 27, 2023).

Maitra, S., Tian, Y., and Cassidy, M. J. (2022). “Investigation of the installation process of drag-in plate anchors from LDFE modelling.” *https://doi.org/10.1680/jgeot.21.00402*, Thomas Telford Ltd .

Manzari, M. T., and Dafalias, Y. F. (1997). “A critical state two-surface plasticity model for sands.” *Geotechnique*, Thomas Telford Services Ltd, 47(2), 255–272.

Musial, W., Spitsen, P., Duffy, P., Beiter, P., Marquis, M., Hammond, R., and Shields, M. (2022).

"Offshore Wind Market Report: 2022 Edition; Executive Summary."

Neubecker Randolph,., M. F. (1995). "Profile and Frictional Capacity of Embedded Anchor Chains." 121(November), 797–803.

Neubecker, S. R., and Randolph, M. F. (1995). "Performance of Embedded Anchor Chains and Consequences for Anchor Design." *Proceedings of the Annual Offshore Technology Conference*, OnePetro, 1995-May, 191–200.

Peng, J., and Liu, H. (2019). "Analytical study on comprehensive behaviors of drag anchors in the seabed." *Applied Ocean Research*, Elsevier, 90(January), 101855.

di Prisco, C., Flessati, L., Frigerio, G., and Lunardi, P. (2018). "A numerical exercise for the definition under undrained conditions of the deep tunnel front characteristic curve." *Acta Geotechnica*, Springer Berlin Heidelberg, 13(3), 635–649.

Da Silva, A. P. (2021). "Macro-element modelling of plate anchors for floating offshore structures accounting for capacity changes during operational conditions."

Singh, S. P., and Ramaswamy, S. V. (2008). "Influence of Frequency on the Behaviour of Plate Anchors Subjected to Cyclic Loading." *Marine Georesources and Geotechnology*, 26(1), 36–50.

Suryasentana, S. K., and Lehane, B. M. (2014). "Numerical derivation of CPT-based p-y curves for piles in sand." *Geotechnique*, 64(3), 186–194.

Suryasentana, S. K., and Lehane, B. M. (2016). "Updated CPT-based p–y formulation for laterally loaded piles in cohesionless soil under static loading." *Geotechnique*, 66(6), 445–453.

Tian, Y., Randolph, M. F., and Cassidy, M. J. (2015). "Analytical solution for ultimate embedment depth and potential holding capacity of plate anchors." *Geotechnique*, 65(6), 517–530.

Uzunoglu, E., Oguz, E., and Guedes Soares, C. (2021). "An Overview of Platform Types Used in Floating Wind Energy." *2nd International Congress on Ship and Marine Technology*, (September).

Vivatrat, V., Valent, P. J., and Ponterio, A. A. (1982). "The Influence of Chain Friction on Anchor Pile Design." *Proceedings of the Annual Offshore Technology Conference*, OnePetro, 1982-May, 153–156.

VRYHOF. (2018). *VRYHOF 2018*.

WAMIT. (2011). “Wamit, Inc. - The State of the Art in Wave Interaction Analysis.” <https://www.wamit.com/> (Aug. 28, 2023).

Yang, R., Zheng, X., Chen, J., and Wu, Y. (2022). “Current Status and Future Trends for Mooring Systems of Floating Offshore Wind Turbines.” *Sustainable Marine Structures*, Nan Yang Academy of Sciences Pte Ltd, 4(2), 40–54.

Zhang, Y., Fan, S., Li, S., and Yin, J. (2023). “Analysis of the drag anchor behaviour at shallow depths.” *Computers and Geotechnics*, 160(May).

- **Results Variation with domain size**

The distance of the anchor centroid to the fixed boundary was investigated

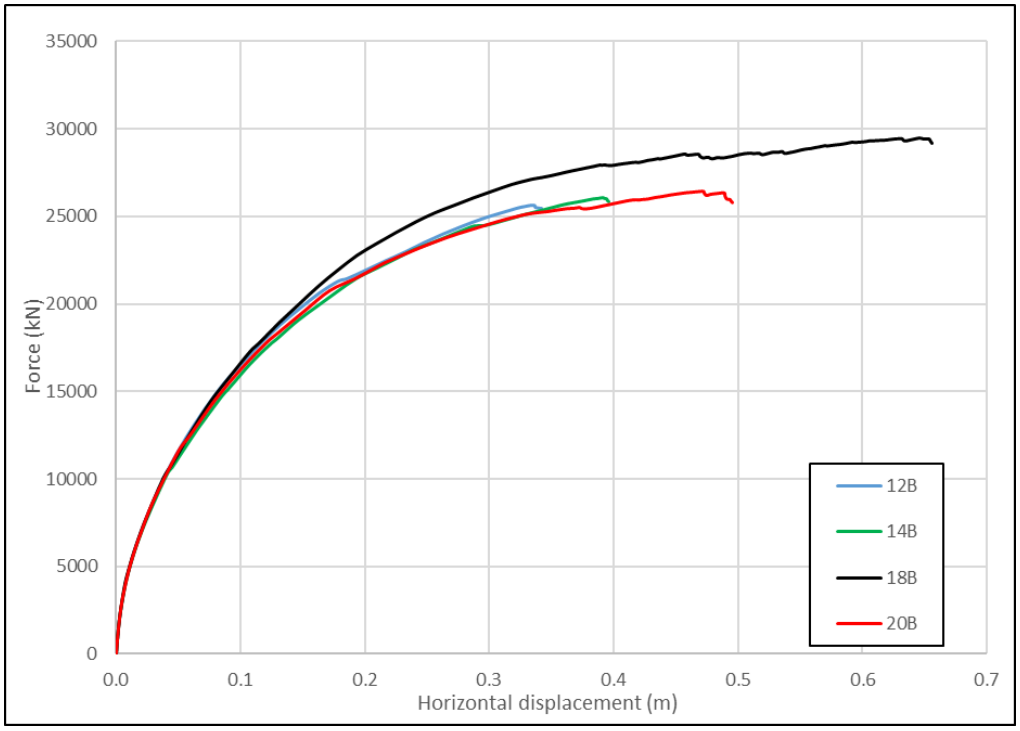

- **Results Variation with element size**

The element size close to the anchor was investigated

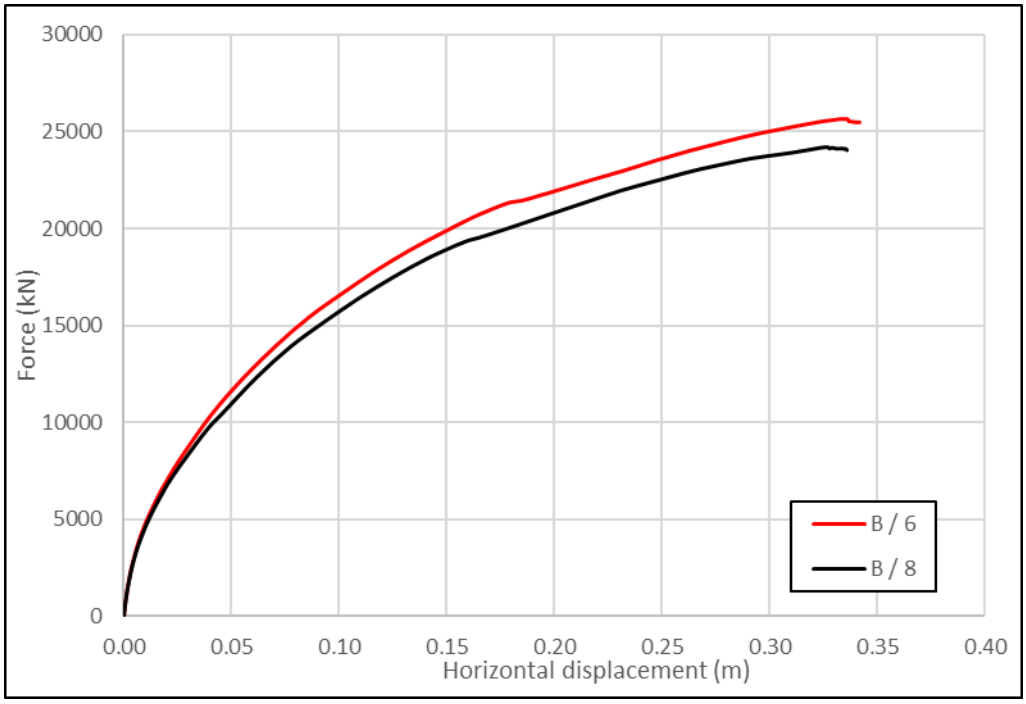

- **Results Variation with domain height**

The height of the sand layer was investigated

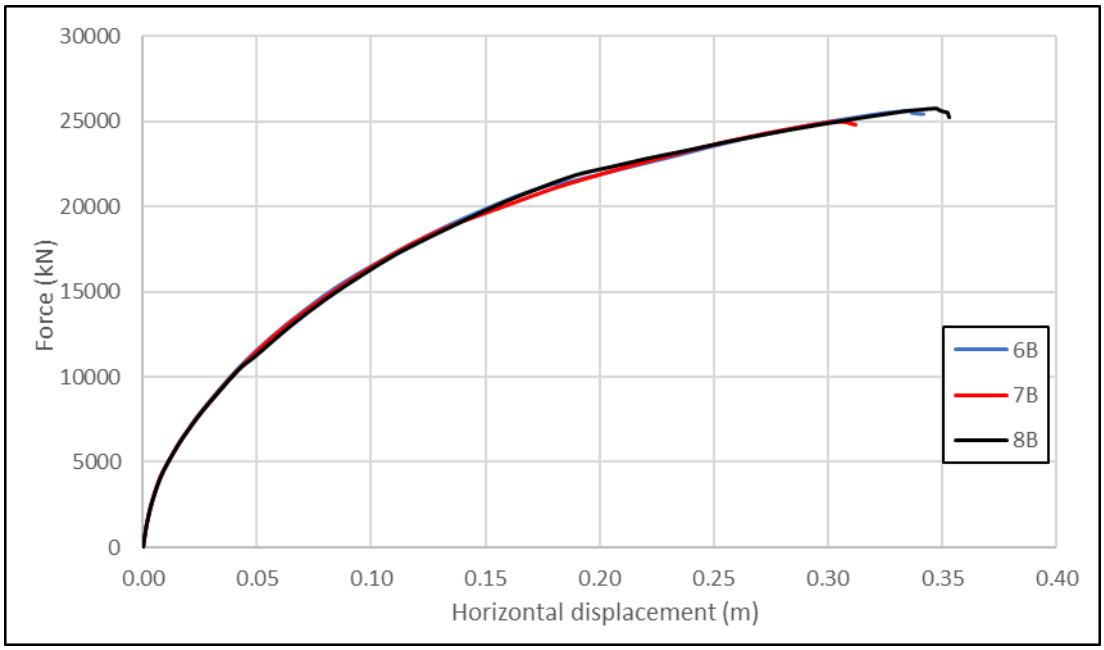

- **Results Variation with interface elements parameters – cohesion**

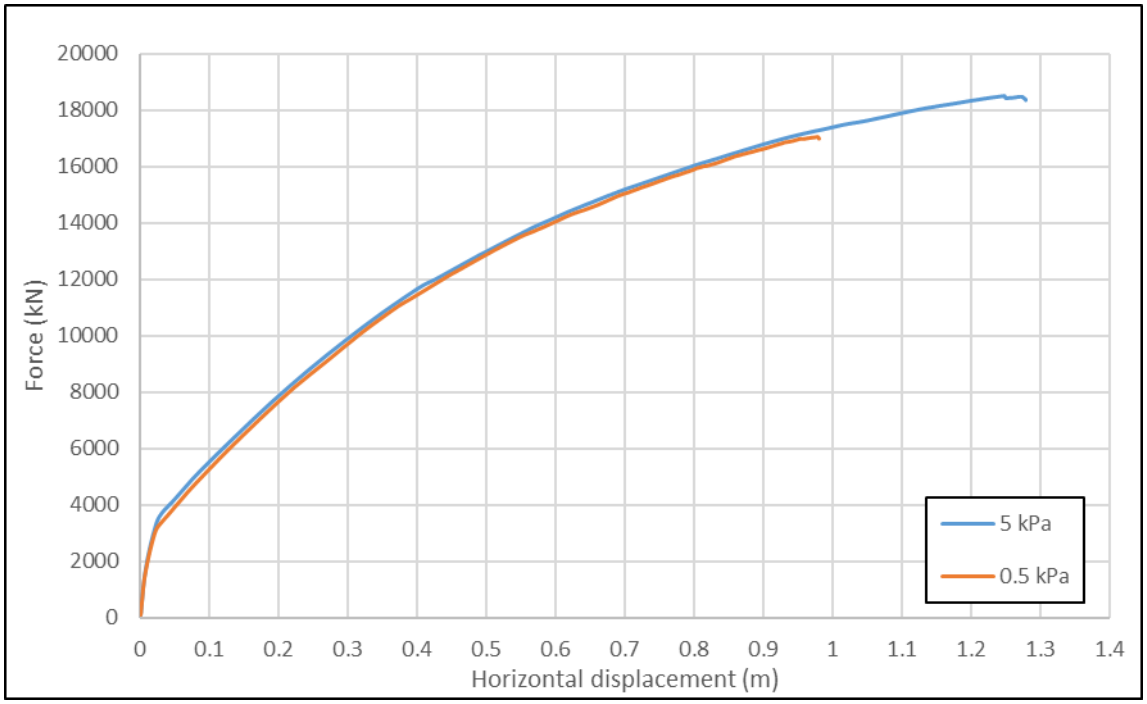

- **Results Variation with interface elements parameters – dilation angle**

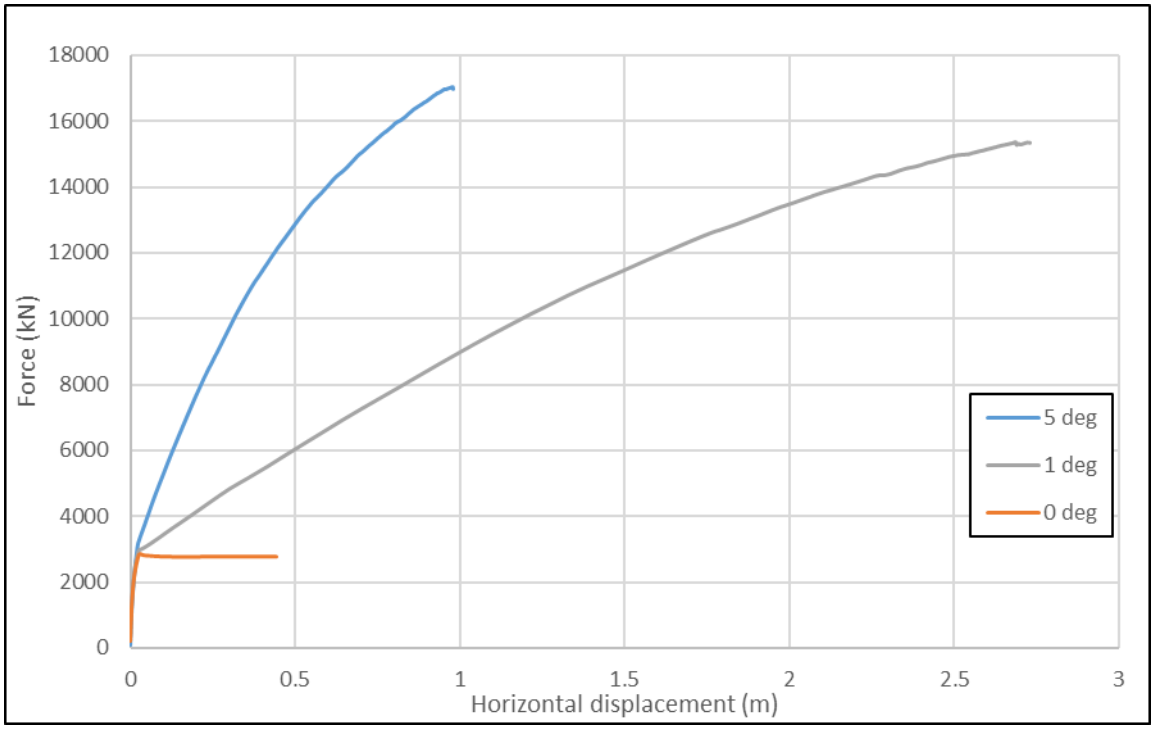

- **Results Variation with max load fraction per step (PLAXIS Numerical control parameter)**

The parameter that limits the maximum load applied per step as a fraction of the ultimate load was observed to affect the results of the cyclic load simulations performed for Chapter 6.

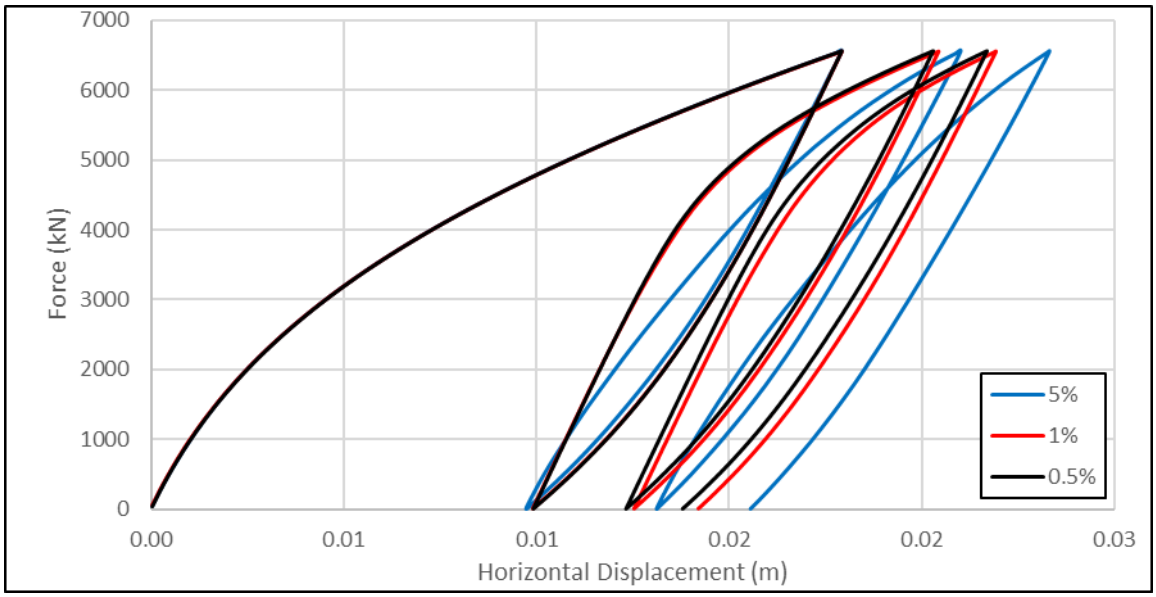

- **Calibrated Parameters for the Analytical Expressions of Chapter 5**

Linear Elastic Perfectly Plastic

$z_c/z_{c,max}$	K_{el} (kN/m)	u_{yield} (m)
35%	166758.4	0.0826
47%	192544.2	0.1136
60%	216186.4	0.1275
70%	245224.4	0.1281
80%	284918.2	0.1227
90%	312484.7	0.1192
100%	338861.8	0.1241

Bi – Linear

$z_c/z_{c,max}$	K_{el} (kN/m)	u_{yield} (m)	K_{pl} (kN/m)
35%	243368.4	0.0368	39500.64
47%	279482.6	0.0492	48615.25
60%	346536.8	0.0469	63538.17
70%	479888.9	0.0311	103953
80%	498044	0.0378	96504.9
90%	661479.2	0.0263	127181.8
100%	609765.7	0.0365	119066.9

Linear Elastic Logarithmic

$z_c/z_{c,max}$	K_{el} (kN/m)	u_{yield} (m)
35%	286815.4	0.0143
47%	316909.5	0.021
60%	368171.5	0.0229
70%	421388.7	0.0235
80%	483450.6	0.0224
90%	556448.2	0.0205
100%	594661.9	0.0216

Hyperbolic

$z_c/z_{c,max}$	K_{el} (kN/m)	Pu (kN)
35%	348325.3	19025.37
47%	388398.5	30635.01
60%	443649.3	39112.9
70%	512413.9	45743.57
80%	585338.1	50088.04
90%	666074.4	53189.06
100%	706580.5	60057.48

- **Formulation of the Kementzetzidis et al. 2022 1D model**

1) Rheological Scheme

$$dy = dy_e + dy_p$$

2) Elastic Law

$$dy_e = \frac{dp}{K}$$

3) Yield Criterion

$$F = \left|p - p_a\right| - p_y = 0$$

4) Plastic Flow Rule

$$dy_p = d\lambda \cdot \mathrm{sgn}\left(p - p_a\right)$$

5) Hardening Rule

$$dp = H \cdot dy_p$$

with

$$H = \frac{\alpha \cdot m}{D} \cdot \left|\bar{p}_u - p\right| \cdot \left|\frac{1}{\alpha} \ln\left(\frac{\bar{p}_u - p}{\bar{p}_u - p_0}\right)\right|^{\frac{m-1}{m}}$$

$$\bar{p}_u = p_u \cdot \mathrm{sgn}\left(dp\right)$$

6) Memory Surface

$$F_M = \left|p - p_{a,M}\right| - p_M = 0$$

With

$$H_M = H \cdot \exp\left\{\mu_0 \left(\frac{b_m}{b_{ref}}\right)^2\right\}$$

$$b_M = \left|p - \tilde{p}_M\right|$$

$$\tilde{p}_M = p_{a,M} + \bar{p}_M$$

$$\bar{p}_M = p_M \cdot \mathrm{sgn}\left(dp\right)$$